The Dynamics and Kinematics of Bio-inspired Swimming Systems

ARCHIVES
MASSACHUSETTS INSTITUTE OF TECHNOLOGY
JUN 25 2013
LIBRARIES

by

Lisa Janelle Burton

B.S.E., Duke University (2007)
S.M., Massachusetts Institute of Technology (2009)

Submitted to the Department of Mechanical Engineering
in partial fulfillment of the requirements for the degree of

Doctor of Philosophy in Mechanical Engineering

at the

MASSACHUSETTS INSTITUTE OF TECHNOLOGY

June 2013

© Massachusetts Institute of Technology 2013. All rights reserved.

Author .....
Department of Mechanical Engineering
May 20, 2013

Certified by .....
Anette E. Hosoi
Chair, Associate Professor, Mechanical Engineering
Thesis Supervisor

Certified by .....
John W. M. Bush
Advisor, Professor, Applied Mathematics
Thesis Supervisor

Accepted by .....
David E. Hardt
Chairman, Department Committee on Graduate Theses

The Dynamics and Kinematics of Bio-inspired Swimming Systems

by

Lisa Janelle Burton

Submitted to the Department of Mechanical Engineering
on May 10, 2013, in partial fulfillment of the
requirements for the degree of
Doctor of Philosophy in Mechanical Engineering

Abstract

The motion of biological systems in fluids is inherently complex, even for the simplest organisms. In this thesis, we develop methods of analyzing locomotion of both mechanical and biological systems with the aim of rationalizing biology and informing robotic design. We begin by building on existing visualization framework by studying an idealized swimmer: Purcell's three-link swimmer, at low Reynolds number. This framework allows us to illustrate the complete dynamics of the system, design gaits for motion planning and identify optimal gaits in terms of efficiency and speed.

We extend the three-link swimmer case to include effects such as the interaction between the links. By studying several systems, we broaden the applicability of our framework. These systems include a two-link swimmer at low Reynolds number with offset centers of buoyancy and mass and a swimmer with a continuously deformable shape, the serpenoid swimmer.

Drawing on the principles behind the serpenoid swimmer, we develop the kinematic decomposition, a method using a singular value decomposition (SVD) that describes the motion of complex systems in a low order manner. We show that with only two degrees of freedom, one can adequately describe an animal's motion. We apply this method to species in both high and low Reynolds number environments to elucidate different phenomena, including chemotaxing and species comparison in spermatozoa, gait changes in eels (steady versus accelerating), kinematic responses to viscosity and viscoelasticity in *C. elegans* (nematodes), and the Kármán gait in trout. Combined with our visualization framework, we successfully illustrate the generalized utility of the kinematic decomposition method to explore and understand fundamental kinematics of a wide range of both natural and man-made systems.

Thesis Supervisor: Anette E. Hosoi
Title: Chair, Associate Professor, Mechanical Engineering

Thesis Supervisor: John W. M. Bush
Title: Advisor, Professor, Applied Mathematics

For Mom & Luis

Acknowledgments

First and foremost, I am incredibly grateful to the two greatest PhD advisors a graduate student could wish for: Prof. Anette "Peko" Hosoi and Prof. John W. M. Bush. I looked forward to my weekly research meetings with Peko, who always seemed to problem solve, redirect, interpret or question in exactly the way I needed. She is one of the best teachers I know and if everyone was a little more like Peko, the world would certainly be a better place. I've loved working with John – his enthusiasm, whether about quantum mechanics, fluids or food, is infectious. Our meetings were frequently derailed by descriptions of recipes, dishes, or restaurants and this shared interest led to many fun side projects, including two devices that will hopefully appear in a restaurant one day. I would also like to thank my committee members, Prof. Howie Choset at Carnegie Mellon and Prof. Sangbae Kim at MIT, for their friendliness and thoughtful feedback during this process.

This research would be incomplete without the contributions of several fantastic collaborators. I would like to acknowledge Ross Hatton, now at Oregon State University, for his friendship, patience and kindness in teaching me many difficult concepts and his contributions, specifically to Chapters 2 and 3. At MIT, Roman Stocker and Jeff Guasto provided the spermatozoa data and valued feedback for Chapters 5 and 6. From the University of Washington, I am indebted to J. Nathan Kutz, Jeff Riffell, and Yasmeen Hussein for their guidance, expertise and fluorescence data on the sea urchin sperm. From Harvard, I'd like to thank George Lauder and Jeanette Lim for sharing their data and for the greatest lab tour I've ever had. From the University of Pennsylvania, I thank Paulo Arratia, Xiaoning Shen and David Gagnon for their *C. elegans* data and fruitful discussions. From Tufts University, I thank Eric Tytell for his time and sharing his eel data and from the University of Florida, Jimmy Liao and Otar Akanyeti for the trout data. Thank you to my UROPs over the past four years, namely Audrey Sedal, Victoria Hammett, Marty Sweeney, Anna Merrifield and Samir Patel. Further, Rob Carnes served as a fantastic mentor and sponsor through Battelle during my time as a PhD student. I also thank José Andrés and César Vega

for their contributions to the culinary devices presented in Appendix C.

The work in this thesis would not be possible without the support from the Battelle Memorial Institute, the National Science Foundation, the National Science Foundation Graduate Student Research Fellowship and the MIT Department of Mechanical Engineering.

I am grateful to have found support and friendship in the members of both research groups. These friendships started many years ago, when Dawn was the first graduate student I met during my MIT visit. Later, she introduced me to Peko and therefore is, in many ways, responsible for some of the most important decisions I've made in graduate school. Since then, she has always made herself available for venting, cheering, consoling and everything in between. I don't know what I would do without Nadia, who is the most thoughtful and caring person I know. I feel so lucky to have sat just feet away from her for four years and to endure many workouts alongside her. There was never a dull moment when Nadia and Ahmed were around. They always brought a smile on my face, even during tough times when I needed it most. Thanks to Tony (see you in Austin!), Amos, Sungyon, and all of the other members of Team Peko who always took the time to teach, comment and share with me. Thanks to Lydia, Anand, Jan, Dan, Lyuba and the other members of the Applied Math Fluids Lab, who also provided me with lots of great feedback (and entertainment).

I would be remiss if I didn't thank Leslie Regan, Una Sheehan, and Joan Kravitz in the Mechanical Engineering Graduate Office who are somehow able to keep hundreds of scattered people organized. Moreover, they care deeply about their students and just a short chat with any of them in the hallway always brightened my day. Also, a special thanks to Shirley Entzminger and Sean Buhrmester who were always so helpful.

My first introduction to research was through an undergraduate project at Duke with Prof. Don Bliss and Dean Linda Franzoni. They showed me how challenging, satisfying, enjoyable, and above all, *fun* research can be and were the driving force behind going to grad school. Thank you both for spending so much time with me – words can't express the influence you've had on me.

Burton Conner has been my home for the past four years and my graduate school experience would have been incomplete without my family there. Thank you to all of the residents of Burton 2, who never failed to entertain me with Dance Central or to amaze me with everything you all achieve and to the GRTs and house team, who helped make my time as a GRT so enjoyable.

Of course, I also want to thank my friends – Katie, Jenna, Andrej, Jamie, Christy, Mike, Mary, Abbey, Megan, Kate, Mari, Barbara, and Fen, among others – who provided welcomed (almost always food-related) distractions and mean more to me than they will ever know. You all make it very bittersweet to leave Boston, but I look forward to lifelong friendships (and frequent visits!).

My family has provided constant support through every stage of my life and it was especially appreciated during my time at MIT. A very sincere thank you to my mom (who believes I can do anything and is the first to celebrate with me when things are going well and to give me hope when they aren't), to Luis (for encouraging me to challenge myself, starting with going to the best college and not worry about the financial burden), to Lauren (who keeps me grounded – usually by calling me a nerd – but is also the first and loudest to tell everyone how proud she is of me) and to my dad (whose scientific curiosity and creativity – as demonstrated by his ability to make anything from duct tape and wire hangers and desire to understand how things work – I inherited). I am fortunate to have a loving and supportive extended family, from grandparents, aunts, uncles, and cousins, who all mean the world to me. Thank you.

Contents

List of Figures

List of Tables

Chapter 1

Introduction

Biology and nature are an increasingly popular source of inspiration for engineered materials and devices. For example, Velcro originated from mimicking burrs and superhydrophobic materials were inspired from the Lotus plant [8]. Many robots have biological counterparts, including ones that crawl like snakes [25, 65], burrow like razor clams [167, 168] or sandfish lizards [35, 97], walk on water like water striders [67], and climb walls like geckos [78, 128] and snails [23]. Swimming robots comprise a large part of the bio-inspired robot population, with machines that mimic snakes [65], jellyfish [27, 110], tuna [148], and a host of other fish [31, 37, 94, 95, 98, 146, 153].

Evolutionary pressures over millions of years have driven biological systems to their current state, which is likely to be locally, if not globally, optimal. Many animals far outperform man-made systems, as shown in Fig. 1-1. In this figure, we measure performance by *agility*, or turning speed, in units of angular frequency and *maneuverability*, defined as the turning radius, normalized by body length. The circled systems in the figure are man-made and are both less agile and less maneuverable than most of the animals surveyed. To improve man-made robots using bio-inspired principles, we must identify and understand the elements responsible for an animal's performance. These elements are likely a combination of structure, material, kinematics, and sensory systems.

Modeling and measuring living systems is inherently difficult. In most cases, we cannot control an animal's muscles or neurons to prescribe an input and measure the

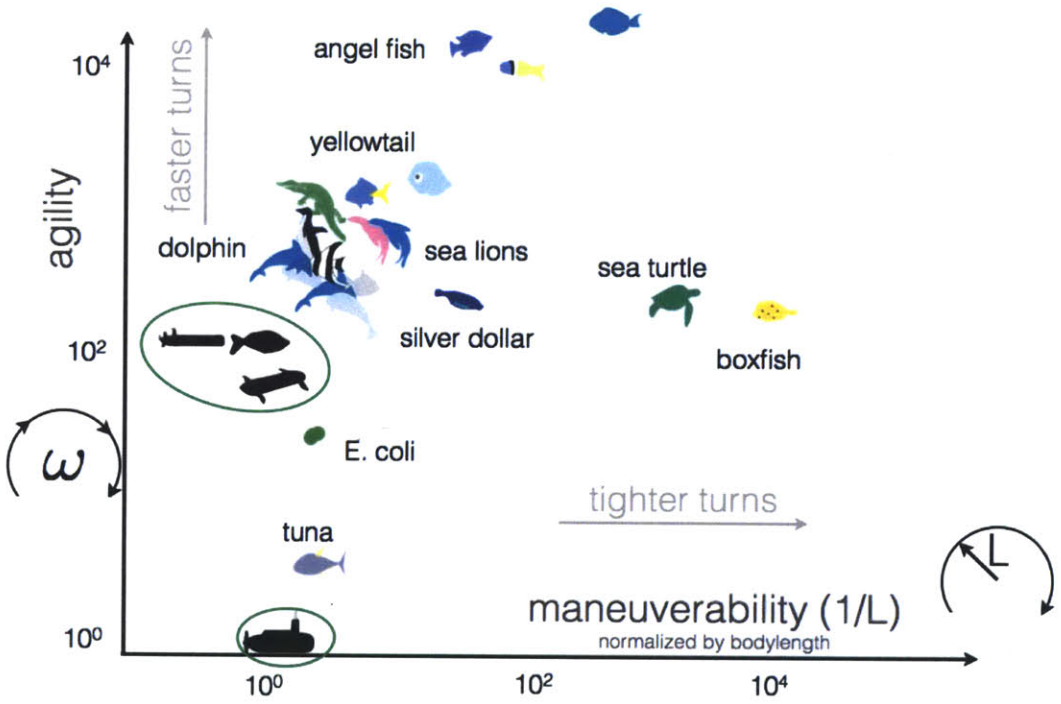

Figure 1-1: Biological organisms outperform man-made systems (circled) in terms of agility and maneuverability. Agility is the turning speed of a system and maneuverability is the inverse of the turning radius, normalized by body length. Courtesy of Audrey Sedal.

behavior or motion that results, as we would with a robotic system. When control or measurement of muscle activity is possible, it typically requires invasive procedures, like anesthetization and surgery [87]. A more easily attainable method of measurement is by observation, typically through recording video of an animal swimming in different environments or conditions. Images from these videos are then analyzed and data points along the animal, and sometimes within the flow, are tracked. From this data, many researchers use multiple kinematic metrics, such as velocity, tail beat frequency, amplitude of several points along the body and wavelength and wave speed of traveling waves down the body [83]. Another approach is to represent the kinematics by fitting the body shape in time to known functions, such as sines and cosines [116]. The number of parameters required for these methods typically vary between 8 and 30. From a modeling and control perspective, many parameters hinder our ability to quickly and efficiently visualize and understand the system.

The difficulty in modeling kinematics is not unique to biological systems. Recent advancements in soft and deformable robotics have spawned new device technologies such as muscle-like actuators [110, 127], which are increasingly more biological in nature. Standard methods to model and incorporate these technologies into robotic systems do not exist. Further, motion planning for more traditional robots with many discrete actuators, such as snake robots, is time consuming and difficult to optimize due to the high dimensionality of the parameter space and inability to visualize the system dynamics. Studying the kinematics of animals may give rise to lower dimensional control methods for efficient motions in robots: by coupling actuators in a manner that allows the robot to form biological patterns, roboticists can execute intricate, but effective motions with fewer parameters. Thus, improvements in understanding the biomechanics and locomotion of complex systems are imperative for informed robotic design and to understand the compromise between discrete mechanical components and biological motion.

Representing and comparing biological kinematics is essential, for instance, to examine the effects of an environment on an animal, kinematic changes during development, escape response versus cruising motions in fish, or swimming versus crawling

in snakes and nematodes. In this thesis, we address the need for a straightforward, non-invasive, quick representation of kinematics and dynamics of biological systems with two primary contributions. First, we present a novel framework to visualize the dynamics of a system swimming at low Reynolds number (and therefore in a drag-dominated environment) and exploit this framework to predict a system's motion and identify globally optimal strokes. Second, we develop the kinematic decomposition method, which draws out the dominant features of a system and effectively reduces the number of parameters needed to describe complex motion. Using this method as a comparative analysis tool, we study biological systems and demonstrate the decomposition's utility through examples that include determining the kinematic response of animals to environment, genetics, and the presence of an attractant.

This thesis is organized into two parts. In Part I, we focus on optimization and visualization of idealized swimming systems, beginning with Chapter 2, where we explore the dynamics and kinematics of the three-link, or "Purcell," swimmer at low Reynolds number. We review and expand upon recent geometric mechanics-based work in developing visualization tools, namely connection vector fields and curvature constraint functions. We utilize this framework and take advantage of the inherently kinematic nature of swimming at low Reynolds number to discover optimal strokes in terms of efficiency and displacement, and explore the limits of our fluids model. Drawing on these results, we extend the theory developed in Chapter 2 to study a two-link swimmer with offset centers of mass and buoyancy in Chapter 3. We compare the resulting dynamics visualizations and models to those found for the three-link swimmer and discuss the consequences of introducing an unactuated degree of freedom. In Chapter 4, we employ models common in snake robotics to develop a 'serpenoid' swimmer, a continuously deformable snake-like swimmer [65]. We prescribe its motion using sinusoidal basis functions in the curvature space, measured along the arclength of the swimmer. The visualizations and system dynamics are now parameterized using the amplitudes of the basis functions. We compare the optimal serpenoid motions to those found for the three-link swimmer.

The study of the serpenoid swimmer leads us to biological motions in Part II,

starting with sea urchin sperm. In Chapter 5, we develop a novel method of representing complex biological kinematics in a low-dimensional parameter space, allowing us to take advantage of the visualization framework exploited in the previous chapters. We incorporate the kinematic representation with a low Reynolds number fluid model to obtain the optimal strokes. For one species of sea urchin sperm (*Arbacia punctulata*), we analyze the kinematic differences during chemotaxis, or motion due to the presence of an attractant. Using a classification metric, we determine whether or not the sperm is chemotaxing, given the kinematics alone. In Chapter 6, we generalize our dynamics and kinematics tools to study the flagellar kinematics of six different sperm and examine the effect of diversity in terms of natural environment and genetics, the effect of viscosity and viscoelasticity in swimming *C. elegans*, steady versus accelerating gaits in eels, and passive and active gaits in rainbow trout. Best practices for performing kinematic decomposition are presented in Appendix A. We conclude in Chapter 7 with a discussion of future directions and expansions.

The work presented in Chapter 2 and 4 is submitted to the *Journal of Fluid Mechanics*. Chapter 3 appears in *Physics of Fluids* [19]. The research in Chapters 5 and 6 is in preparation to be submitted to the *Journal of Experimental Biology*. In Appendices B and C, we address two problems of interfacial phenomena: the role of flexibility in floating at an interface and two bioculinary devices that depend on surface tension. The work in Appendix B appears in *Physics of Fluids* [18] and Appendix C is submitted to *Bioinspiration & Biomimetics*.

Part I

Optimization and visualization of low Reynolds number swimming

Chapter 2

The three-link swimmer

A growing interest in natural and artificial microswimming has led to a variety of recent studies that address the unique challenges associated with swimming at small scales. A microswimmer's inertia is negligible compared to the effects of viscosity of the surrounding fluid (i.e., the Reynolds number is small); as such, these swimmers must employ strokes that do not depend on momentum to achieve a net translation. A well recognized consequence of this constraint is Purcell's *scallop theorem* [120], which states that in low Reynolds number flows, a system with a single internal degree of freedom cannot locomote. This theorem has led to several investigations of minimal swimming that examine the smallest increase in complexity needed to generate a system capable of locomotion.

Many of these investigations focused on breaking the symmetry of the swimmer by adding internal degrees of freedom, either through actively controlled joints [108, 144], or passive flexible members [170]. Other approaches have been to change the environment by using temporally and/or spatially varying magnetic fields to actuate or pull a passive swimmer [36], posing the swimming problem in a viscoelastic fluid [42], or adding inertia to the body only, so that the inertia of the fluid is still negligible [46].

The three-link swimmer has been well studied over several decades, though the relationship between strokes (especially those with large amplitudes) and net displacement of the system has presented unresolved challenges. In this chapter, we review a geometric framework for analyzing the three-link system at low Reynolds number

that uses tools from geometric mechanics, *connection vector fields* and *constraint curvature functions*, to visualize the complete system dynamics and the net displacement per stroke. By adopting a minimum perturbation coordinate representation of the system, the framework achieves greater accuracy in the face of nonlinearities than previous similar efforts. Using these novel geometric mechanics-based visualization tools, we highlight optimal translational and rotational gaits (in terms of displacement per stroke and efficiency) for the three-link swimmer and find optimal motions for a swimmer with continuous curvature. We then use these results to discuss the importance of including fluid interactions between the links by comparing resistive force theory to slender body theory. Further, we explore basis functions for parameterizing different systems to represent an extensive range of motions and shapes.

2.1 Background

Understanding the underlying mechanisms of locomotion in low Reynolds number swimming is key to advancing technologies across several disciplines, including using microrobots that move through the body for local drug delivery, observation or minimally invasive surgery. The challenge of designing such systems arises from the distinctive fluid-structure interaction that occurs at low Reynolds number, where the viscous drag from the fluid dominates inertial forces. In this environment, the act of gliding does not exist; that is, if the system ceases to change it shape, it instantly stops locomoting. Therefore, swimming strategies effective in moderately high Reynolds number environments, where inertia dominates and movements may rely on gliding, may not be effective at low Reynolds number.

The study of low Reynolds number locomotion spans several decades. A fundamental lecture by E.M. Purcell is often cited as the starting point for the topic [120]. In this lecture, Purcell proposed a minimalist model for low Reynolds number swimming: an infinitely slender three-link swimmer that moves its two joints in an alternating pattern. Using simple symmetry arguments, he demonstrated that any further reduction (such as to a two-link swimmer) would leave the system unable

to generate net motion over a stroke cycle. Purcell also identified that, in the low Reynolds number regime, the net motion produced by a stroke is geometric—i.e. it depends only on the series of shapes that the system moves through, and not on the rate with which it changes shape. This swimmer has since been adopted as a canonical model in low Reynolds number swimming, serving as an example of a wide range of analyses [6, 7, 54, 56, 59, 81, 144]. Becker *et al.* [7] employed a conventional fluid dynamics approach to analyze the direction and distance of net motion produced by Purcell strokes of different amplitudes (a question that had been left open since Purcell's original lecture), then optimized geometric parameters such as the link lengths to maximize the efficiency of the strokes. Tam & Hosoi [144] expanded and improved this optimization of morphology by additionally considering the kinematics as well as the geometry, allowing the joints to move simultaneously in coordinated patterns.

Another set of studies examined locomotion from a more geometric approach. Shapere & Wilczek [135] formalized Purcell's observations on the geometric nature of low Reynolds number swimming by drawing on tools from gauge theory in electromagnetism. Avron & Raz [6] applied an extension of this approach (similar to that used by Melli *et al.* [101] for high Reynolds systems) to determine net translation over various strokes and relate the displacement to an area integral in the space of joint angles. These geometric methods lose accuracy when the swimmer rotates significantly (which introduces non-commutative terms into the equations of motion), and so were historically most accurate when applied to small-amplitude strokes or to symmetric swimmers that do not undergo significant instantaneous rotation. Hatton *et al.* [56, 58, 61], however, demonstrated that appropriate coordinate transformations could mitigate the effect of the rotations, allowing geometric analysis of high-amplitude strokes.

Here we combine both of these approaches, merging the rigorous fluid dynamics models used by Becker *et al.* [7] and Tam & Hosoi [144] with the organizational structure and visualization framework in Shapere & Wilczek [135], Avron & Raz [6], and Hatton & Choset [56, 61]. We specifically review identifying cyclic shape changes, i.e., *strokes* or *gaits*, that efficiently displace the system over each cycle, and which

serve as the basic building blocks for motion over longer distances.

Starting in §2.2, we demonstrate the use of geometric mechanics tools in visualizing and understanding locomotion, and review key results from their previous application to swimming at low Reynolds numbers. In §2.3, we review the use of geometric tools to identify optimal strokes under a simplified model of low Reynolds number swimming (resistive force theory) and compare them to strokes found by the parametric optimization methods reported in existing literature. In §2.4, we build upon previous work to incorporate a more accurate fluid dynamics model (slender body theory) that includes hydrodynamic coupling between the links, and use the geometric tools to characterize the difference in output between it and the simpler model.

2.2 Kinematics of low Reynolds number swimming

A key feature of swimming at low Reynolds number is that it is *kinematic*: the sequence of positions the swimmer moves through in the world depends only on the sequence of shapes it assumes, and is independent of the rate of shape changes. This kinematic structure was recognized in Purcell's lecture and formalized by Shapere & Wilczek [135] in a differential-geometric framework adapted from the gauge mechanics of particle physics. Further work in the robotics community [55, 58, 61, 77, 107, 113, 114, 115] has developed Shapere & Wilczek's geometric mechanics formulation into a powerful set of tools for representing the motion of swimmers and other locomoting systems. These tools have formed the basis for a range of swimming studies on systems including anguilliform robots [98], fish [104], the three-link swimmer [6, 54, 56, 59], a two-link swimmer with offset centers of mass and buoyancy [19], and general deformable surfaces [59, 77], and are at the heart of the analysis in this thesis.

The three-link swimmer is commonly studied because of its simplicity and the amount of existing literature focused on this topic. Analytical tools are largely sufficient for solving the physics of this system, making it an accessible problem over many decades. We primarily use the three-link swimmer to develop our model and

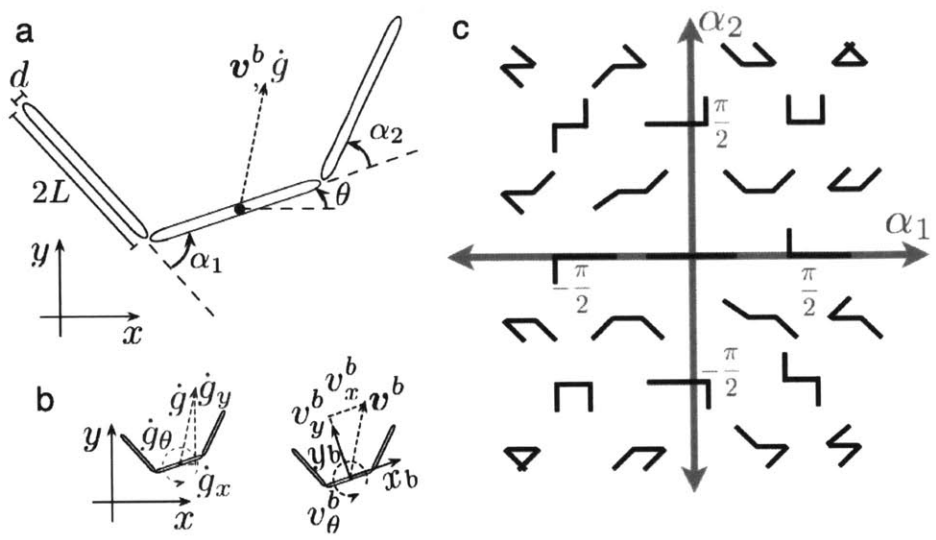

Figure 2-1: (a) The three-link swimmer is parameterized by the joint angles α_1 and α_2. (b) The motion of the system can described in terms of body velocity $\boldsymbol{v}^b$ or global velocity $\dot{\boldsymbol{g}}$. (c) The shape space of the three-link swimmer.

geometric framework, though it can be applied, in the present form, to any system whose shape is described by two parameters. The framework for systems requiring more than two parameters uses the same high level structure, though some of the visualization tools are less developed for these higher dimensions.

As an illustration of how this geometric formulation works, we first consider the motion of a basic three-link swimmer, shown in Fig. 2-1a, using a simplified model of fluid dynamics. This fluids model (resistive force theory) serves as an introduction to the more complete models we employ in §2.4, sharing key mathematical structure but with a more intuitively tractable derivation. Similarly, the swimmer is an elementary system for locomotion in a uniform fluid [120], and captures the important features of the swimmers we examine later in this chapter while adding as few complicating details as possible.

2.2.1 Dynamics at low Reynolds number

The physics of swimming systems are characterized by the Reynolds number, defined as $Re = \rho u L/\mu$ where ρ is the fluid density, μ is the dynamic viscosity and u and

L are the characteristic velocity and length scales. At low Reynolds number, where $Re \ll 1$, the hydrodynamics of the system are governed by the Stokes equations. These equations are simplified from the Navier-Stokes equations and represent the conservation of mass, $\boldsymbol{\nabla} \cdot \boldsymbol{u} = 0$, and the momentum balance between the pressure gradient and the contribution from viscous drag, $\boldsymbol{\nabla} p = \mu \nabla^2 \boldsymbol{u}$, where $\boldsymbol{u}$ and p are the velocity and pressure in the fluid. The boundary conditions for the swimming problem are found by matching the velocity of the swimmer at the boundary, and assuming the fluid velocity vanishes far from the swimmer, $\boldsymbol{u} \to 0$ at ∞. Physically, these equations reflect that momentum is instantly diffused at low Reynolds number and inertia of the system is negligible. In this case, the total hydrodynamic force on the system can be modeled as zero at every instant [24]. For swimming problems, we take advantage of this property and find the translation resulting from a given shape change as that which keeps the forces in balance over the whole motion.

Stokes equations are difficult to solve generally, commonly because the boundary conditions are prescribed on the moving boundary of the system and are time dependent. Though analytical solutions are difficult to find, certain methods have been developed to approximate these solutions. One method, used for long, slender bodies, is to express the force along the system as a convergent series, linear in local body velocity [30]. In cases where fluid flow around portions of the body interacts weakly with other portions of the body or surrounding objects, the local hydrodynamic drag can be modeled using resistive force theory (RFT), which considers just the first term in the series.

RFT for an elongated body (such as a link of our swimmer) takes the fluid forces on the body as linearly related to its velocity [47], and the longitudinal drag coefficient (along the link) as related by a known proportion to the lateral drag coefficient (perpendicular to the link). The drag coefficient ratio is dependent on the slenderness ratio $\varkappa$, or body width divided by body length. In the limit of infinite slenderness ($\varkappa \to 0$), the ratio of longitudinal to lateral drag approaches two [47], so that the

dimensionless forces on a rigid link of length $2L$ are expressed as:

$$F_{i,x} = \frac{\hat{F}_{i,x}}{\mu L^2 \omega} = \frac{L\omega}{\mu L^2 \omega} \int_{-L}^{L} \frac{1}{2} c_0 \mu v_{i,x}^b \mathrm{d}\ell = c_0 v_{i,x}^b \tag{2.1a}$$

$$F_{i,y} = \frac{\hat{F}_{i,y}}{\mu L^2 \omega} = \frac{L\omega}{\mu L^2 \omega} \int_{-L}^{L} c_0 \mu v_{i,y}^b \mathrm{d}\ell = 2 c_0 v_{i,y}^b \tag{2.1b}$$

$$M_i = \frac{\hat{M}_i}{\mu L^3 \omega} = \frac{\omega}{\mu L^3 \omega} \int_{-L}^{L} c_0 \mu \ell (\ell v_{i,\theta}^b) \mathrm{d}\ell = \frac{2}{3} c_0 v_{i,\theta}^b \tag{2.1c}$$

where $c_0\mu$ is the viscous drag coefficient, $F_{i,x}$ and $F_{i,y}$ are the dimensionless longitudinal and lateral forces of the ith link, respectively, and M_i is the moment of that link. The *body velocity*, $\boldsymbol{v}^b$, is the *world velocity*, $\dot{\boldsymbol{g}}$, as expressed in the basis of the instantaneous body frame, illustrated in Fig. 2-1b. All quantities are dimensionless, normalized by length L, dynamic viscosity μ, and frequency of motion ω.

2.2.2 Shape, position, and velocity

The force equations in (2.1) are given in terms of individual link velocities. To find the forces acting on a swimmer, we must relate these individual link velocities to a set of generalized coordinates and velocities that describe the state of the whole swimmer. As a first step in finding these relationships, we decompose the swimmer's configuration into a *shape* and *position*.

The shape of the three-link swimmer is the relative position of points on the body, captured by the joint angles $\boldsymbol{\alpha} = (\alpha_1, \alpha_2)$. The *shape space* for this system is a two-dimensional space defined by the limits of the joint angles, as shown in Fig. 2-1c. Each point in this space corresponds to a specific shape of the three-link swimmer. Trajectories through the shape space represent time-varying deformations of the system and if cyclic, are referred to as gaits or strokes. To fully describe the system's configuration, we combine the joint angle vector $\boldsymbol{\alpha}$ with a position $\boldsymbol{g}$ that describes the location and orientation of a body frame attached to some point on the system (for example, the middle link or center of mass).

Following these definitions, the rate of change of the swimmer's configuration (its

generalized velocity) can be represented as the combination of the *shape velocity* $\dot{\boldsymbol{\alpha}}$ together with either the world velocity, $\dot{\boldsymbol{g}}$, or the body velocity, $\boldsymbol{v}^b$.

Once the configuration coordinates are chosen for the system, the velocity of every point on the body can be determined in terms of the shape $\boldsymbol{\alpha}$, shape velocity $\dot{\boldsymbol{\alpha}}$ and body velocity $\boldsymbol{v}^b$. Here, we are interested in the body velocities of the three links at their centers, which resolve under basic kinematics as

$$\boldsymbol{v}_1^b = \begin{bmatrix} v_{x,1}^b \\ v_{y,1}^b \\ v_{\theta,1}^b \end{bmatrix} = \begin{bmatrix} \cos\alpha_1 & -\sin\alpha_1 & \sin\alpha_1 \\ \sin\alpha_1 & \cos\alpha_1 & -(\cos\alpha_1 + 1) \\ 0 & 0 & 1 \end{bmatrix} \begin{bmatrix} v_x^b \\ v_y^b \\ v_\theta^b \end{bmatrix} + \begin{bmatrix} 0 \\ \dot{\alpha}_1 \\ -\dot{\alpha}_1 \end{bmatrix} \tag{2.2a}$$

$$\boldsymbol{v}_2^b = \begin{bmatrix} v_x^b \\ v_y^b \\ v_\theta^b \end{bmatrix} \tag{2.2b}$$

$$\boldsymbol{v}_3^b = \begin{bmatrix} v_{x,3}^b \\ v_{y,3}^b \\ v_{\theta,3}^b \end{bmatrix} = \begin{bmatrix} \cos\alpha_2 & \sin\alpha_2 & \sin\alpha_2 \\ -\sin\alpha_2 & \cos\alpha_2 & \cos\alpha_2 + 1 \\ 0 & 0 & 1 \end{bmatrix} \begin{bmatrix} v_x^b \\ v_y^b \\ v_\theta^b \end{bmatrix} + \begin{bmatrix} 0 \\ \dot{\alpha}_2 \\ \dot{\alpha}_2 \end{bmatrix}. \tag{2.2c}$$

2.2.3 Forces on a swimmer

By taking the link velocity kinematics in (2.2) together with the force laws in (2.1), we can find the forces acting on the swimmer as a function of its configuration and velocity. These forces can then be summed together to find the net force on the system as

$$\begin{bmatrix} \sum F_x \\ \sum F_y \\ \sum M \end{bmatrix} = \underbrace{\begin{bmatrix} \cos\alpha_1 & \sin\alpha_1 & 0 \\ -\sin\alpha_1 & \cos\alpha_1 & 0 \\ \sin\alpha_1 & -(1+\cos\alpha_1) & 1 \end{bmatrix}}_{\text{link 1 to 2 (body) frame rotation}} \begin{bmatrix} F_{1,x} \\ F_{1,y} \\ M_1 \end{bmatrix} + \begin{bmatrix} F_{2,x} \\ F_{2,y} \\ M_2 \end{bmatrix} + \underbrace{\begin{bmatrix} \cos\alpha_2 & -\sin\alpha_2 & 0 \\ \sin\alpha_2 & \cos\alpha_2 & 0 \\ \sin\alpha_2 & 1+\cos\alpha_2 & 1 \end{bmatrix}}_{\text{link 3 to 2 (body) frame rotation}} \begin{bmatrix} F_{3,x} \\ F_{3,y} \\ M_3 \end{bmatrix}, \tag{2.3}$$

where the matrices serve to rotate the forces on the links into the system body frame and to encode the moment that forces applied to the outer links exert on the body

frame.

Evaluating (2.1) through (2.3) reveals a useful structure to the relationship between the swimmer's configuration, velocity, and forces: the net forces are linear in the generalized velocities, nonlinear in the shape, and independent of the swimmer's position,

$$\begin{bmatrix} \sum F_x \\ \sum F_y \\ \sum M \end{bmatrix} = \mathcal{C}_{3\times 5}(\boldsymbol{\alpha}) \begin{bmatrix} \boldsymbol{v}^b \\ \dot{\boldsymbol{\alpha}} \end{bmatrix}, \tag{2.4}$$

where $\mathcal{C}(\boldsymbol{\alpha})$ is a matrix of the coefficients of velocity resulting from combining (2.1)–(2.3). The structure of (2.4) is of key importance in forming our swimming model, and highlights the usefulness of working with forces and velocities in the basis of the body frame, rather than the world frame. In this treatment, the local dynamics are expressed independently of the system's position, whereas a world-frame representation would need to explicitly include the orientation of the body.

2.2.4 Swimming model

As the final step in building our locomotion model (which relates specified shape velocities to the position velocities that they induce), we combine the net forces in (2.3) with the previously noted condition (§2.2.1) that the net forces on a swimmer at low Reynolds number are in quasi-static equilibrium [24]. This condition acts as a constraint on the system's velocities, such that any physically admissible combination of shape and body velocities on the right of (2.4) must map through the matrix $\mathcal{C}(\boldsymbol{\alpha})$ to produce a vector of zeros on the left. Applying this constraint and separating the $\mathcal{C}(\boldsymbol{\alpha})$ matrix as

$$[0]_{3\times 1} = \mathcal{C}_{3\times 5}(\boldsymbol{\alpha}) \begin{bmatrix} \boldsymbol{v}^b \\ \dot{\boldsymbol{\alpha}} \end{bmatrix} = \mathcal{C}_{B,3\times 3}(\boldsymbol{\alpha})\ \boldsymbol{v}^b + \mathcal{C}_{J,3\times 2}(\boldsymbol{\alpha})\ \dot{\boldsymbol{\alpha}} \tag{2.5}$$

allows us to bring the $\boldsymbol{v}^b$ terms to the left of the equation as

$$\mathcal{C}_B(\boldsymbol{\alpha})\boldsymbol{v}^b = -\mathcal{C}_J(\boldsymbol{\alpha})\ \dot{\boldsymbol{\alpha}}, \tag{2.6}$$

and then invert $\mathcal{C}_B$,

$$\boldsymbol{v}^b = -\mathcal{C}_B^{-1}(\boldsymbol{\alpha})\mathcal{C}_J(\boldsymbol{\alpha})\ \dot{\boldsymbol{\alpha}}, \tag{2.7}$$

to create a mapping between the shape and position components of any velocity.

2.2.5 Reconstruction equation and local connection

Grouping the reconstituted $\mathcal{C}(\boldsymbol{\alpha})$ terms in (2.7) reduces that equation into a *kinematic reconstruction equation* [13, 77, 135] of the form

$$\boldsymbol{v}^b = -\mathcal{A}(\boldsymbol{\alpha})\ \dot{\boldsymbol{\alpha}}, \tag{2.8}$$

in which $\mathcal{A}(\boldsymbol{\alpha})$ is the *local connection*, a Jacobian-like matrix relating the shape velocity, $\dot{\boldsymbol{\alpha}}$, to the body velocity, $\boldsymbol{v}^b$. This derivation originates from those described in [56, 59].

The local connection can be visually represented by its rows as a set of *connection vector fields* that illustrate the local change in position induced by a change in the swimmer's shape, as described by Hatton & Choset [55, 56, 58, 61]. Fig. 2-2 shows the connection vector fields for the three-link swimmer, in x, y, and rotation θ in the body frame (note that a similar figure first appeared in [56]). The body velocity for a given shape velocity vector $\dot{\boldsymbol{\alpha}}$ is found by taking the dot product of the shape velocity vector and vector of $\mathcal{A}_i$ at the current shape, or equivalently, the angle between these two vectors and their magnitudes. Therefore, the body velocity component $\boldsymbol{v}_i^b$ is positive, negative, or zero when these two vectors are aligned (respectively) positively, negatively or orthogonally and is scaled by the magnitudes of $\mathcal{A}_i$ and $\dot{\boldsymbol{\alpha}}$.

The shape vector $\mathbf{a}$ shown in Fig. 2-2 corresponds to a system initially at $(0, 0)$, the fully extended configuration, and moving both outside links away from each other downward. The resultant motion is purely in the positive y direction, or perpendicular

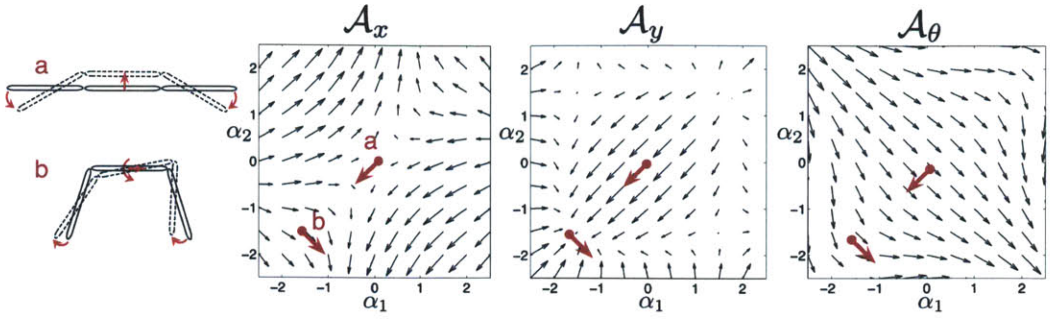

Figure 2-2: Connection vector fields for the three-link swimmer are the rows of the local connection matrix $\mathcal{A}(\boldsymbol{\alpha})$ [56]. The **a** shape vector moves the swimmer purely in the positive y direction as both outside links sweep away from each other, as illustrated in the left subfigure. Moving through shape vector **b** both translates the body in x and rotates it positively.

to the center link, as the shape vector is aligned with the connection vector field. This shape vector moves through a null point in x and is orthogonal to the connection vector field locally in θ. The shape vector **b** is aligned with the x and θ fields and orthogonal to the y field, thus moving the system in the positive x direction while rotating positively.

2.2.6 Net displacement

The connection vector fields illustrate the structure of the local connection matrix and give insight into how shape changes move a system differentially. When studying swimming, however, we are primarily concerned with the net displacement that the system can achieve over longer time periods T,

$$\boldsymbol{g}(T) = \int_0^T \dot{\boldsymbol{g}}(t)\,\mathrm{d}t = \int_0^T \begin{bmatrix} \cos\theta(t) & -\sin\theta(t) & 0 \\ \sin\theta(t) & \cos\theta(t) & 0 \\ 0 & 0 & 1 \end{bmatrix} \boldsymbol{v}^b(t)\,\mathrm{d}t, \tag{2.9}$$

where we take the system as starting at the origin of the space. The matrix in the rightmost expression rotates the body velocity into the global frame for integration. Substituting in the relationship between shape and body velocity in (2.8) finds the

net displacement over a given change in shape (a trajectory $\boldsymbol{\alpha}(t)$ through the shape space with an associated velocity function $\dot{\boldsymbol{\alpha}}(t)$),

$$\boldsymbol{g}(T) = -\int_0^T \begin{bmatrix} \cos\theta(t) & -\sin\theta(t) & 0 \\ \sin\theta(t) & \cos\theta(t) & 0 \\ 0 & 0 & 1 \end{bmatrix} \mathcal{A}(\boldsymbol{\alpha})\ \dot{\boldsymbol{\alpha}}\, \mathrm{d}t. \tag{2.10}$$

Because the local dynamics, and therefore (2.10), are linear in the shape velocity, increasing the rate at which the shape trajectory is followed proportionally increases the rate at which the swimmer moves along the corresponding position trajectory. Therefore, the time integral in (2.10) can be converted into a line integral over the shape space,

$$\boldsymbol{g}(\boldsymbol{\alpha}(T)) = -\int_{\boldsymbol{\alpha}(0)}^{\boldsymbol{\alpha}(T)} \begin{bmatrix} \cos\theta(\boldsymbol{\alpha}) & -\sin\theta(\boldsymbol{\alpha}) & 0 \\ \sin\theta(\boldsymbol{\alpha}) & \cos\theta(\boldsymbol{\alpha}) & 0 \\ 0 & 0 & 1 \end{bmatrix} \mathcal{A}(\boldsymbol{\alpha})\ \mathrm{d}\boldsymbol{\alpha}, \tag{2.11}$$

in which the time-scaling of the motion drops out [57]. This conversion embodies Purcell's principle that swimming at low *Re* is kinematic—the resulting displacement is a function only of the path through the shape space, $\boldsymbol{\alpha}(t)$, and is independent of the pacing with which it is followed.

Equation (2.11) maps changes in the swimmer's shape to the displacements they induce. When considering the motion of locomoting systems we are often concerned with the inverse of this mapping: finding shape changes that produce desired net displacements. In general, such an inversion requires either a parametric "shooting method" optimization of the $\boldsymbol{\alpha}(t)$ trajectory [144] or a closed-form solution to the integral in (2.11). For most combinations of systems and shape inputs, such a closed form solution does not exist—the θ in the integrand's rotation matrix is itself a component of the integrated displacement $\boldsymbol{g}$. A useful approximation of a closed form does exist, however, for an important class of shape changes: strokes or gaits that form closed curves in the shape space.

Strokes are interesting for system analysis because they capture a swimmer's ability to transform internal shape changes into net displacement over large scales. Swimmers' *available* shape spaces are bound by limits on the extent to which they can bend, but a finite ratio generally exists between the amount the system changes shape and the distance it travels (this ratio is explicitly encoded here by the local connection $\mathcal{A}$, but the principle holds even if the system has a dissipative "drifting" or "coasting" term in its equations of motion). To fit arbitrarily-long changes in shape into the bounded shape spaces, therefore, swimmers and other locomoting systems tend to move in cyclic patterns, which can then be characterized by the motion over a single cycle.

Strokes' cyclic nature also makes them easier to analyze than open-ended shape changes, in that they allow us to apply a family of tools called *curvature methods* [6, 13, 56, 77, 101, 135] to find the displacements they induce. These methods are based on the principle that to find the net displacement over a cycle, we do not have to explicitly calculate the intermediate displacements, but only *their failure to cancel themselves out over the course of a cycle.* In general, this failure to self-cancel corresponds to the change in the system dynamics across the gait. If the dynamics remain the same as the swimmer moves away from and then returns to the starting shape, then the translations induced by the return will "undo" the effects of the outbound motion. If, however, the return is executed with different dynamics, then there will be a residual net displacement commensurate with the change in dynamics. For kinematic systems like the low Reynolds number swimmer, the change in system dynamics is measured by the *curvature* of the system constraints encoded in the local connection [55].

The swimmer's net displacement over a gait can be represented as the transformation $\boldsymbol{g}(T)$ between its position at the start and end of the gait cycle, or via the exponential coordinates $\boldsymbol{z}(t)$ of this transformation. The exponential coordinates of a transformation are a vector that describes the constant body velocity required to achieve that transformation in unit time; an average effective body velocity. If the system is spinning while moving forward, it will not move in a straight line. The

pure-translation and pure-rotation motion we consider in this paper correspond directly to the components of $\boldsymbol{z}(\boldsymbol{\phi})$, the net displacement over a gait $\boldsymbol{\phi}$, related to the global position through the exponential map, $\boldsymbol{g}(T) = \boldsymbol{g}(0)\exp(z(\boldsymbol{\phi}))$ [122]:

$$\boldsymbol{z}(\boldsymbol{\phi}) = \iint_{\phi_a} \boldsymbol{\nabla} \times \vec{\mathcal{A}}_i(\alpha_1, \alpha_2)\, \mathrm{d}\alpha_1 \mathrm{d}\alpha_2 + \iint_{\phi_a} [\mathcal{A}_1, \mathcal{A}_2]\, \mathrm{d}\alpha_1 \mathrm{d}\alpha_2 + \text{higher order terms} \tag{2.12}$$

where $[\mathcal{A}_1, \mathcal{A}_2]$ is the local Lie bracket of the vectors $\mathcal{A}_1(\alpha_1, \alpha_2)$ and $\mathcal{A}_2(\alpha_1, \alpha_2)$.

The first two terms on the right hand side of (2.12) are both area integrals over the region of the shape space enclosed by the gait. The first term is the *body velocity integral*, or BVI. The BVI is a "forward minus backwards" definition of net motion measuring total distance traveled (where moving backwards is negative distance) and rotation. The BVI gives an approximate estimate of displacement in the global frame but the accuracy depends heavily on the system and the gait. In special cases, Stokes' theorem is used to find the net motion after one cycle [77, 105, 161]. If the shape change is a gait $\boldsymbol{\phi}$, Green's form of Stokes' theorem converts this line integral into an area integral matching the first term of (2.12),

$$\boldsymbol{\zeta}(T) = \int_0^T \boldsymbol{v}_i^b(\tau)\, \mathrm{d}\tau = \iint_{\phi_a} \boldsymbol{\nabla} \times \mathcal{A}_i(\alpha_1, \alpha_2)\, \mathrm{d}\alpha_1 \mathrm{d}\alpha_2 \tag{2.13}$$

$$= \iint_{\phi_a} \frac{\partial \mathcal{A}_i 2}{\partial \alpha_1} - \frac{\partial \mathcal{A}_{i,1}}{\partial \alpha_2}\, \mathrm{d}\alpha_1 \mathrm{d}\alpha_2 \tag{2.14}$$

where ϕ_a is the area enclosed by the gait.

Changes in the local connection over the shape space determine the value of the BVI. Taking the curl of the local connection is a measure of how nonconservative the connection vector fields are. As such, Hatton & Choset [60] termed the BVI the "nonconservative contribution" to the net motion.

The net displacement of the system depends on the ordering of translation and rotation during the gait and the second term contains this information, capturing the effect of turning. To move laterally, or "parallel park," a car moves back while turning, then forward while turning. The net forward minus back motion may be zero, but net displacement is laterally nonzero and highly dependent on the order

of turning and forward versus back motion. The second term of (2.12) includes a local Lie bracket. In general, the local Lie bracket of two vectors m_1 and m_2 in an $SE(2)$ system finds the result of moving differentially in the $m_1, m_2, -m_1, -m_2$ body directions and is calculated as:

$$\left[\begin{pmatrix} m_1^x \\ m_1^y \\ m_1^\theta \end{pmatrix}, \begin{pmatrix} m_2^x \\ m_2^y \\ m_2^\theta \end{pmatrix}\right] = \begin{pmatrix} m_2^\theta m_1^y - m_1^\theta m_2^y \\ m_2^\theta m_1^x - m_1^\theta m_2^x \\ 0 \end{pmatrix}. \tag{2.15}$$

This second term is referred to as the "primary noncommutative" contribution, as it is found using only the noncommutativity of the columns of $\mathcal{A}$ in the shape space. Together, the first two terms of (2.12) yield the *corrected body velocity* or cBVI. The cBVI is "corrected" because it includes information from the noncommutativity to improve the estimate of net displacement.

The two leading order terms in the series (2.12) are both area integrals, and thus we can visualize them as the volumes enclosed under a set of surfaces that are the components of the integrands in (2.13). For historical reasons related to their differential geometric derivation, these functions are referred to as *constraint curvature functions* and are the scalar representations of $\mathcal{H}^i = \boldsymbol{\nabla} \times \mathcal{A}_i(\alpha_1, \alpha_2) + [\mathcal{A}_1, \mathcal{A}_2]_i$, the integrand of the first two terms in (2.12). Physically, the volume of the curvature function enclosed under the gait is the displacement from the cBVI, therefore plotting the curvature function allows easy identification of gaits which produce desired displacements and rotations. For example, in the bottom row of Fig. 2-3, the gait encloses negative volume in x, and in both y and θ, the positive and negative volumes enclosed cancel, so that net motion is purely in the x direction.

2.2.7 Constraint curvature function analysis

Visually plotting the constraint curvature functions offers significant intuition into the swimmer's system dynamics [6, 56, 101, 133]. The constraint curvature functions for the three-link swimmer in x, y, and θ are shown in Fig. 2-3. The circular stroke

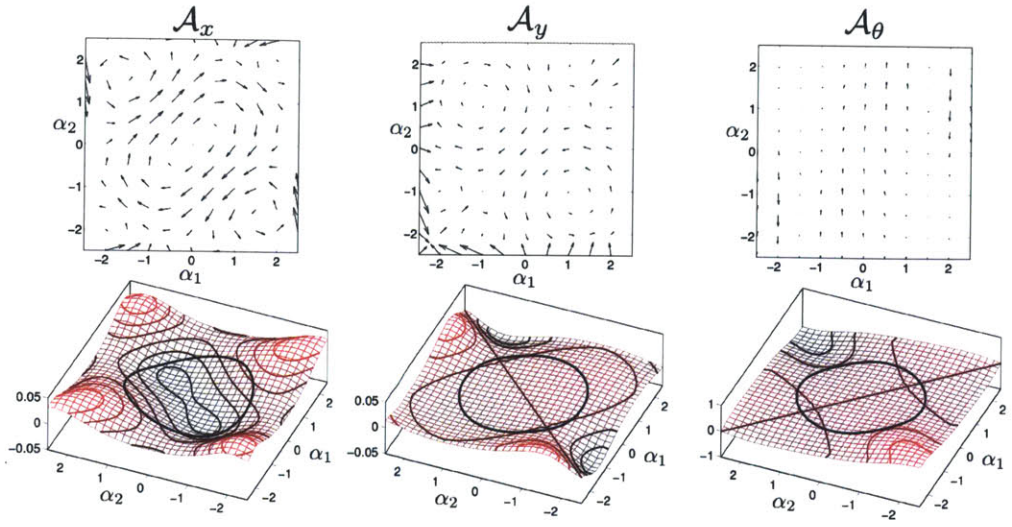

Figure 2-3: Connection vector fields (top) and constraint curvature functions (bottom) for the three-link swimmer. The volume enclosed by a closed curve is an indication of net motion. These fields and functions are for the system's motion in the minimum-perturbation coordinates described in §2.2.8 [58].

plotted on the three subfigures represents a system's shape changes over one cycle. The volumes enclosed by this gait on the three functions are the components of the cBVI approximation of the net displacement over a cycle, in the respective directions. The stroke encloses a non-zero volume on the function associated with $\mathcal{A}_x$ and so the three-link swimmer moves in x over each cycle; on the x and y plots, it encloses balanced positive and negative regions, and so produces no net displacement in these directions. This volume enclosure is a direct visual interpretation of the cBVI from (2.12) and demonstrates the power of these tools: the constraint curvature functions visually represent all of the system dynamics. With these plots, one can quickly estimate a system's motion resulting from any gait and identify optimal gaits.

There are two key, quickly identifiable features of the constraint curvature functions. The first is the zero contour that separates sign-definite regions. These contours enclose purely positive or negative regions, and so represent local maxima or minima in terms of net displacement per cycle. Any gait larger than this contour will enclose regions of the opposite sign, and will therefore move less distance per cycle. Gaits

smaller than the contour will enclose a subset of the sign-definite region, and therefore will also achieve less net displacement. The second easily identifiable feature is sets of symmetric axes on each constraint curvature function. The three curvature functions in Fig. 2-3 exhibit symmetry across the $\alpha_1 = \alpha_2$ and $\alpha_1 = -\alpha_2$ axes. The odd symmetries present in the curvature functions associated with $\mathcal{A}_y$ and $\mathcal{A}_\theta$ account for the net zero sum enclosed by the path in those figures. Symmetries of the curvature function in the shape space also simplify motion planning. Once one desired stroke is selected, a reflection across an axis of symmetry will give an identical magnitude of net motion. Further, our analysis generalizes comparisons between two systems; simply plot their constraint curvature functions to identify similarities and differences, as we will in §2.4 to compare two models of fluid forces acting on the swimmer's links.

2.2.8 Minimum perturbation coordinates

Error introduced by truncating the expression for translation in (2.12) is related to intermediate rotation and is dependent on the choice of coordinates used. While the dynamics of the system are coordinate-system invariant, the estimation of net displacement depends strongly on the choice of coordinates [57]. The error will remain small if the orientation of the system remains fairly constant during a stroke.

Orientation is preserved in general when gaits have a small amplitude, as previous works on Lie algebra analysis have shown [101, 135]. From a locomotion point of view, these small amplitude gaits are often very inefficient gaits, resulting in a strong need to investigate a range of higher amplitude gaits when searching for optimal strokes. Further details on the calculation of the minimum perturbation coordinate frame and reference points are discussed in [56] and [57].

Avron & Raz [6] and Melli *et al.* [100] both used link-attached frames that rotated significantly during locomotion to design gaits for swimming robots, with gait amplitudes proportional to the joint angle amplitudes. This system rotation limited their results to net rotation or the translation induced by very small strokes. Hatton & Choset [57] recognized that the body-frame rotation is coordinate-dependent; for instance, the mean orientation line can be used for the orientation component of

position, and rotates considerably less than any individual link and so is a preferred coordinate choice to a link-attached frame. Building on this observation, Hatton & Choset identified the optimal choice of coordinates for curvature analysis as the *minimum perturbation body frame*, that is, the weighted average of the link positions and orientations that differentially moves the least in response to changes in shape. This coordinate choice is the one for which the magnitudes of the rows of the local connection $\mathcal{A}$ are smallest, and can be found by applying a modified Hodge-Helmholtz decomposition to the vector fields from the original coordinates [57]. Fig. 2-3 shows the connection vector fields and constraint curvature functions in these minimum perturbation coordinates. Note that changing to minimum perturbation coordinates does *not* reduce the net motion of the system. Instead, it is essentially finding the point on the swimmer that moves in the "straightest line" between beginning and ending configurations, and so has the shortest pathlength traveled during the motion out of all points on the swimmer.

Using minimum perturbation coordinates, how reliably can we use the cBVI to measure the net displacement? Fig. 2-4 shows the exact displacement and displacement from the cBVI in original and minimum perturbation coordinates for circular strokes with increasing amplitude. The error will vary with different strokes: in areas of the shape space that are relatively small in $\mathcal{A}_\theta$, the displacement from the cBVI will be a very close approximation of actual displacement. For the three-link swimmer, we observe a large divergence between using minimum perturbation versus original coordinates to calculate the cBVI for stroke amplitudes greater than one. While both cBVI measurements increase initially, the cBVI in minimum perturbation coordinates reveals an optimal stroke amplitude at approximately 1.6. Larger amplitude strokes begin to enclose volume of the opposite sign, decreasing the net displacement of the system. The exact displacement and cBVI in minimum perturbation coordinates are in good agreement for all stroke amplitudes [53].

To review, we first model the system in a convenient coordinate frame (the body frame of the center link) and then perform a simple change of coordinates to a frame that minimizes error, allowing us to use the more geometric, visually represented body

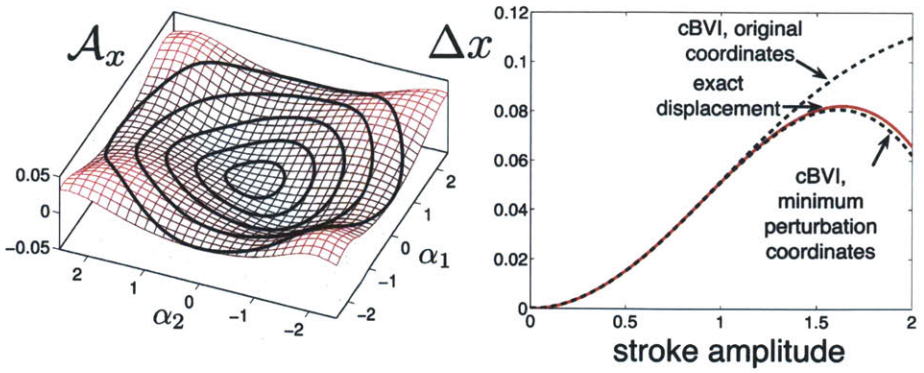

Figure 2-4: Displacements calculated from the cBVI in original coordinates and minimum perturbation coordinates, compared to the exact displacement for the circular strokes shown to the left, with increasing amplitude.

velocity and its components to draw out useful gaits and details about the system's dynamics.

2.3 Optimal strokes

To compare systems and identify the morphology best suited for, say, speed or efficiency, it is essential to first identify each system's most effective motion. Therefore, determining optimal strokes is an important part of ensuring fair comparisons and allows us to draw meaningful conclusions about systems and gaits. To find "good" swimming gaits, it is common to begin by selecting known stroke patterns from nature or intuition and comparing the resulting forces and displacements.

2.3.1 Maximum displacement

Maximum distance per cycle strokes are easy to find with our methods and are useful benchmarks in finding maximum efficiency strokes. Previous work, such as [144], has found the maximal displacement stroke in x by direct parameterized optimization. However, using the constraint curvature functions, we can directly identify maximal displacement strokes by looking for the zero contour to identify sign-definitive regions

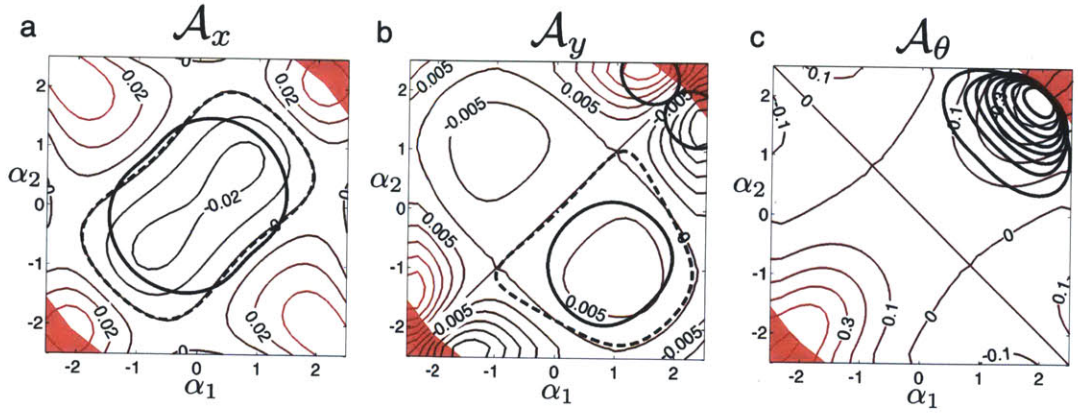

Figure 2-5: a) Optimal displacement per cycle (dashed line) and efficiency (solid line) strokes on the x curvature functions for a three-link swimmer. b) Locally and globally optimal efficiency strokes for y motion (solid lines) and maximum displacement per cycle stroke (dashed line). c) The largest amplitude stroke is the optimal efficiency rotation stroke. Small concentric strokes are optimal for quantized rotations to be used in motion planning. The shaded regions in the corners of each shape space represent configurations of the three-link swimmer where the links overlap.

of the constraint curvature function, as discussed in §2.2.7. Comparing these strokes against parameter-optimized strokes shows that this result is intuitively satisfying. If the stroke were any larger or smaller, it would enclose less volume on the curvature function and the system would have smaller net displacement, thus the stroke maximizes the displacement integral. The resulting x stroke is shown in Fig. 2-5a (originally from [56, 59]) and, as expected, agrees with previous results from Tam & Hosoi [144]. The maximum displacement stroke for y is in Fig. 2-5b. Avron & Raz [6] made a similar observation using their curvature analysis, but the error in their methods resulted in only qualitative agreement with the "pinched" feature on the x stroke. The actual stroke they predicted was significantly different quantitatively and produces almost no displacement.

2.3.2 Maximum efficiency

The maximum displacement per cycle assumes that any cycle has the same cost. However in many cases, cycles have different effort costs, so that comparisons of

displacement per effort, or efficiency, are more informative measures of system performance. Definitions of hydrodynamic efficiency have evolved in the past several decades. Many early definitions were based on the Froude efficiency of a propellor, or the useful power output over the total power input. Lighthill [91] defined efficiency as the ratio of the power that an external force would spend to translate the system at the average speed to the average power expended by the swimmer during a stroke. Many definitions focus on forward translational motion, such as the definition by Wiggins & Goldstein [166], who defined hydrodynamic efficiency as the comparison of power for longitudinal propulsion to the power dissipated in transverse motions. More generally, Tam & Hosoi [144] defined efficiency as the fraction of the total energy spent to propel the swimmer in a useful direction and Lauga & Powers [85] use the minimum work required to pull the system through the fluid over the work actually done. Another metric commonly used in animal locomotion is the cost of transport, C, defined as the energy needed to move a fixed distance divided by the total mass. Efficiency is indirectly related to the cost of transport (non-dimensionalized by swimming speed) by $C^2 = \varepsilon^{-1} = c\bar{P}/\bar{P}_v$, where $\bar{P}$ is the time-averaged power generated during swimming and $\bar{P}_v \sim \overline{v}^2$ is the power required to drag the swimmer at low Reynolds number. Therefore, choosing the best efficiency is identical to choosing the best cost of transport.

The aforementioned metrics involve time integrals and so cannot be directly incorporated into the geometric framework we outline. However, various researchers in the geometric mechanics community [6, 59] have developed a geometric formulation that is based on the idea that large joint angle motions cost more than small joint angle motions, so the cost of a given motion is related to its arclength in the shape space. The differential cost of executing joint motions is not uniform across the shape space, so this geometric formulation weights the arclength measurement accordingly. The form of this weighting also conveniently non-dimensionalizes the cost, so that we can avoid explicitly considering pacing when comparing strokes.

Following the derivation of the cost metric given in Hatton & Choset [59], we first identify that the differential work required to make a differential shape change

is equivalent to the power required to move with a given shape velocity. The power dissipated by the joints is the dot product of shape velocity with torque acting on the joints:

$$P = \dot{\boldsymbol{\alpha}} \cdot T(\boldsymbol{v}^b, \dot{\boldsymbol{\alpha}}) \tag{2.16}$$

The torque on the joints is calculated by applying the forces and moments from RFT to the links, and is a linear function of the body and shape velocities. Using the linear dependency of $\boldsymbol{v}^b$ on $\dot{\boldsymbol{\alpha}}$ defined in the local connection, we can express torque as a linear function of shape velocity only, so that $T(\mathcal{A}\dot{\boldsymbol{\alpha}}, \dot{\boldsymbol{\alpha}}) = f(\boldsymbol{\alpha})\dot{\boldsymbol{\alpha}}^T$, resulting in an expression for power dissipation that depends only on shape and shape velocity:

$$P = \dot{\boldsymbol{\alpha}} f(\boldsymbol{\alpha}) \dot{\boldsymbol{\alpha}}^T \tag{2.17}$$

Further, we can express shape velocity as $\dot{\boldsymbol{\alpha}} = \mathrm{d}\boldsymbol{\alpha}/\mathrm{d}t$ and separate $\mathrm{d}\boldsymbol{\alpha}$ and $\mathrm{d}t$,

$$\mathrm{d}s_P^2 = P\ \mathrm{d}t^2 = \begin{bmatrix} \mathrm{d}\alpha_1 & \mathrm{d}\alpha_2 \end{bmatrix} \underbrace{f(\boldsymbol{\alpha})}_{\mathcal{M}_P} \begin{bmatrix} \mathrm{d}\alpha_1 \\ \mathrm{d}\alpha_2 \end{bmatrix}. \tag{2.18}$$

In this formulation, $\mathrm{d}s_P = \sqrt{P}\ \mathrm{d}t$ is a differential arclength through the shape space, weighted by $f(\boldsymbol{\alpha})$, that accounts for the effort required to change shape by $(\mathrm{d}\alpha_1, \mathrm{d}\alpha_2)$. The cost for a longer motion corresponds to the integral of this arclength over the shape trajectory. The relationship between this arclength, the power dissipated by the swimmer, and the time required to make the shape change encapsulates previous definitions in defining hydrodynamic efficiency as the work required to move the system at a certain speed over the power dissipated to move the swimmer at that speed.

At low Reynolds number, the cost of a motion depends on both the path the system takes through the shape space and the speed at which the motion is executed. Using our metric has the convenient effect of removing the need to consider pacing from the effort evaluation. Pacing, or the speed with which the system traces out the stroke in the shape space, was examined by Beckter *et al.* [7]. They found that the

optimal pacing is achieved when power dissipation is constant in time. Other previous literature took the position that to find the optimal efficiency stroke, it was necessary to fix the swimming speed for a given distance or, equivalently, a fixed time [6]. Our approach has equivalent results but eliminates the need to consider pacing within a stroke in optimization, as the time and power terms are collected into a single metric. The appropriate treatment of efficiency is therefore to use the distance through the shape space, as measured by the power dissipation metric for normalization [59]. In general, a trade off between speed and power exists, so that moving very quickly draws more power.

The stroke for maximum efficiency per cycle in the x direction is shown in Fig. 2-5a, originally from [59]. The geometric interpretation of the maximum efficiency stroke is roughly the curve that encloses the most volume while minimizing the perimeter, weighted by the local "effort" to move to different configurations. The weighting reflects a penalty associated with changing shape along the symmetric axis. The maximum efficiency stroke is more compact than the maximum displacement stroke and encloses the main peak of the curvature function. It is more efficient to execute multiple high-efficiency cycles than to significantly increase the cost of each cycle for little gain. The maximum efficiency stroke forgoes the more extreme areas of the shape space enclosed by the maximum displacement stroke, and even overlaps into the positive region of the curvature function. The cost of including a small part of the positive region is not great enough to incur the cost of extra pathlength and curvature to exclude it.

For optimal motion planning, we are also interested in identifying the optimal strokes in the direction orthogonal to x and for rotation. Fig. 2-5b and c show these strokes, respectively, overlaid onto the curvature functions in those directions in minimum perturbation coordinates. For optimal motion in y (ignoring any motion in x), the curvature constraint function indicated two potential regions for optimal strokes. One is a figure eight stroke in the upper right-hand corner. The other possible optimal stroke is the rounded gait in the lower right corner of Fig. 2-5b. Comparing the efficiencies for these two strokes revealed that the figure eight stroke was more

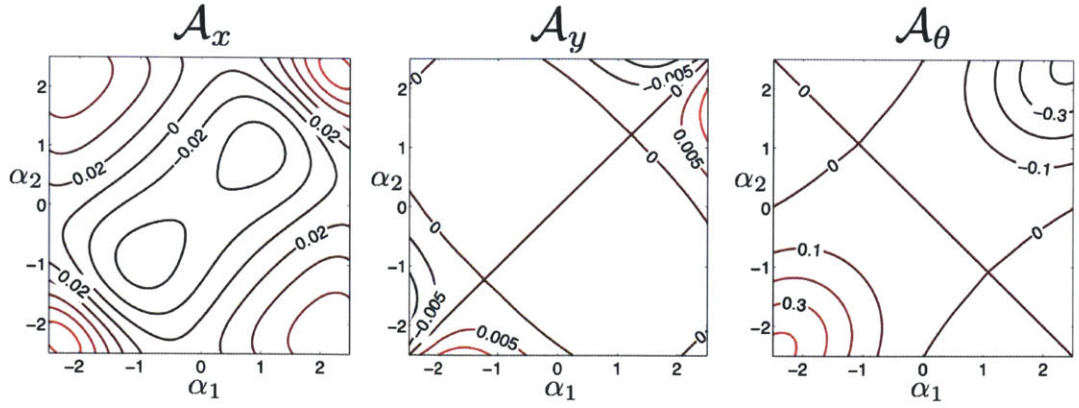

Figure 2-6: Curvature functions for the three-link swimmer using SBT with slenderness ratio $\varkappa \simeq 10^{-4}$. The largest discrepancies from curvature functions found using RFT (figure 2-5) are in the corners of the shape space, at extreme α_1 and α_2 values. In these regions, the links become close and their fluid flows interact.

efficient, but crossed into the region of the shape space where the links of the swimmer self-intersect, leaving the stroke towards the center as the optimal efficiency stroke within the physically achievable regime of the shape space. For either of these strokes, taking advantage of symmetry across the even $\alpha_1 = \alpha_2$ and odd $\alpha_1 = -\alpha_2$ axes allows us to quickly transfer these results to the two domains in the left corners, identifying additional strokes that give identical net displacements. The maximum efficiency rotation stroke is the largest stroke in Fig. 2-5c. Smaller, quantized rotations are also shown in Fig. 2-5c so that the swimmer may reorient itself by a fixed angle, presumably to then move optimally along a straight line in that direction. These strokes were found by requiring that the system undergo a fixed net rotation and identifying the stroke that achieved that rotation with the least amount of power.

2.4 Slender body theory (SBT) versus resistive force theory (RFT)

As discussed in §2.2.1, resistive force theory [47] considers only the first term in the solution to the Stokes equations, the force on each link due to its motion through the

surrounding fluid. In some cases, such as when designing a new swimming system, we may require higher accuracy in our estimate of net displacement. Slender body theory uses the next highest order term to include the coupled forces acting on the link arising from the motion of the other links. SBT, therefore, is a more accurate solution to the Stokes equation. As a link becomes infinitely slender, the effect of its motion on other links by moving nearby fluid becomes negligible and results from SBT approach those from RFT. As an example, Fig. 2-6 shows the curvature functions in minimum perturbation coordinates using SBT for slenderness ratio $\varkappa \simeq 10^{-4}$, where RFT is considered valid because the links are very slender. Typically, making broad comparisons of using these two theories to model the system's motion can be difficult, as examining specific strokes or motions is easier and more accessible but is fairly restrictive. However, examining the height of curvature constraint functions for each theory allows a clear comparison. For instance, identifying the approximate net motion from any stroke for each theory provides a general idea of error between them, and indicates where in the shape space this error is the greatest. For the three-link swimmer, the differences between the two theories are most prevalent in the corners of the shape space, at extreme α_1 and α_2 values, or where the links become close and the coupled forces are important. Ignoring these regions of self-intersection between the links avoids the regions with the largest differences without compromising the main region of interest, the center of the shape space, where the optimal distance and efficiency strokes were found.

Whereas comparing Figs. 2-5 and 2-6 highlights the differences between the two theories for a single slenderness ratio, the real value of our approach is the ability to show how well RFT performs against SBT over a range of slenderness ratios. Fig. 2-7 shows the optimal strokes for distance and efficiency in x for several slenderness ratios. These strokes qualitatively agree with the stroke found using RFT and become more and more similar as the slenderness ratio decreases. Fig. 2-8 shows the (a) distance and (b) efficiency evaluated using the SBT model for both the optimal strokes from RFT and SBT, at several slenderness ratios. If those values agree, it is appropriate to use the stroke from RFT to evaluate the distance or efficiency for

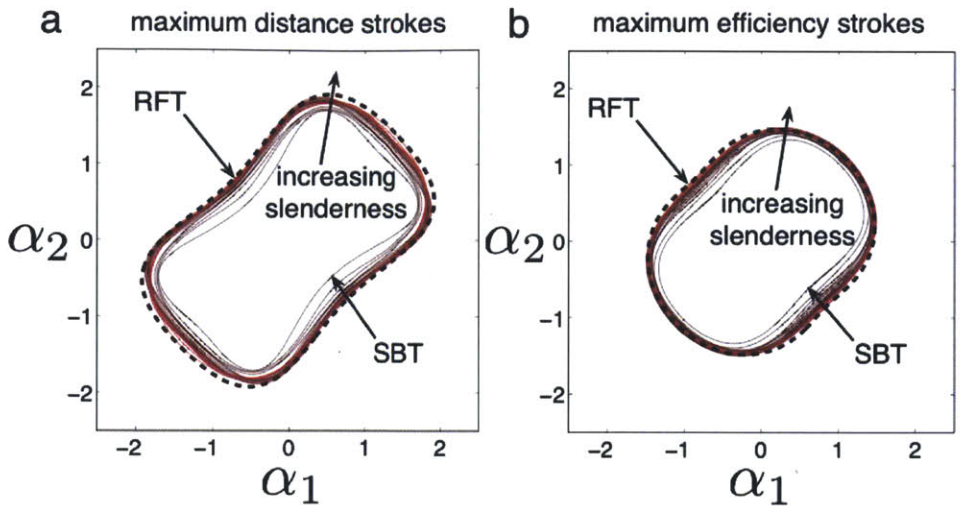

Figure 2-7: Comparison of optimal a) distance and b) efficiency strokes using RFT (dashed line) and SBT for several slenderness ratios (solid lines). Slenderness ratio decreases as the stroke size increases.

three-link swimmer with any slenderness ratio and doing so saves considerable computation time. Although calculating the curvature constraint function using SBT for different systems is computationally very fast, directly finding the optimal stroke for those same systems is not. Evaluating a metric for a set of points in the shape space is straightforward; considering the higher dimensional space of all paths through that space is significantly more complex. From Fig. 2-8a, we see that distances measured using the optimal RFT stroke and the optimal SBT stroke are a close match for very slender links, and this agreement diverges as the links become less slender. Measurements of efficiency, on the other hand, are in close agreement for all slenderness ratios (Fig. 2-8b). There are two conclusions we can draw from these results. First, the dynamics at the center of the shape space (where the efficiency strokes are focused) are less affected by including the SBT terms because in these configurations, interaction between the links is minimal, making the higher order SBT terms less significant. Second, characterizing a system using RFT strokes gives meaningful results for three-link systems with approximately $\varkappa \lesssim 10^{-3}$.

In this chapter we applied a geometric mechanics-based framework and accompa-

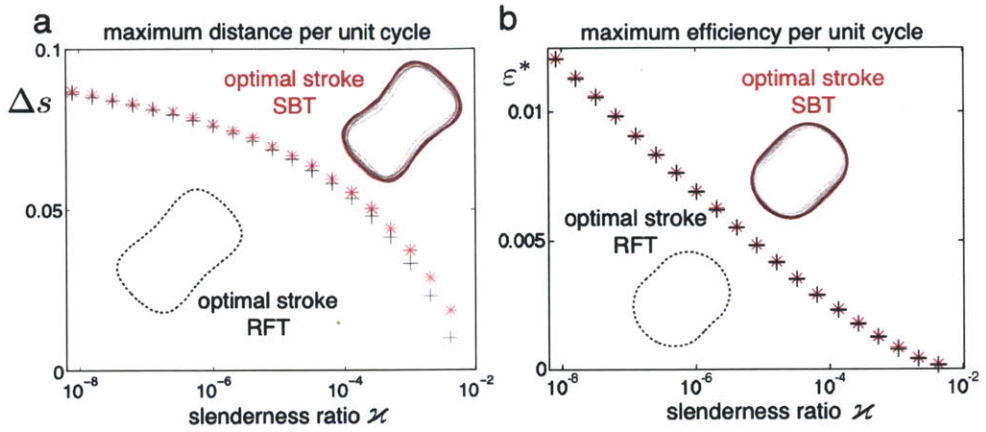

Figure 2-8: a) Distance per cycle calculated using the RFT model evaluated with the optimal SBT strokes (*) and RFT strokes (+). b) Efficiency calculated using the RFT model evaluated with the optimal SBT strokes (*) and RFT strokes (+). For slenderness ratios $\varkappa \lesssim 10^{-3}$, this method can be used with very close quantitative agreement between the two methods.

nying visualization tools, the connection vector fields and constraint curvature functions, to further understanding of the complete dynamics of a system, specifically the three-link swimmer. Using these techniques, we found globally optimal strokes for both maximum distance per cycle and maximum efficiency for translation and rotation. While previous research was limited to using geometric tools for only rotational or small amplitude strokes, our methods took advantage of recent developments using minimum perturbation coordinates, allowing those tools to be applied to a wider range of motion and systems.

We compared resistive force theory (RFT) to the higher order slender body theory (SBT) to determine the effects of the presence of links on each other. We found that for swimmers with slenderness ratios less than approximately 10^{-3}, it is appropriate to use RFT to find an optimal stroke whose value (either distance or efficiency) can be calculated using SBT to save considerable computation time.

Together, the framework and tools will serve as the basis to study systems swimming at low Reynolds number in the upcoming chapters, namely a two-link swimmer with offset centers of mass and buoyancy (Chapter 3), serpenoid swimmer (Chapter

4) and spermatozoa (Chapter 5 and 6). However, this framework and tools extend to a wider class of systems. For instance, the three-link kinematic snake at high Reynolds number systems [56] and a three-link snake in granular media (shown to obey a type of resistive force theory) [34] have been studied. In the following chapter, we address unactuated degrees of freedom by considering a two-link swimmer with offset centers of buoyancy and mass at low Reynolds number [19]. In this case, there is less freedom to choose gaits based on the curvature function. Instead, there is only one prescribed degree of freedom and the other is determined by the dynamics of the system.

Chapter 3

The two-link swimmer

In this chapter, we explore an unactuated degree of freedom by building upon the framework established in Chapter 2 and adding a static separation of the system's centers of mass and buoyancy. This separation gives the neutrally buoyant system an equilibrium orientation to which it passively returns. As the two-link swimmer deforms its body, it changes the orientation of the line between its centers of mass and buoyancy. This rotation is countered by gravity that acts to restore the swimmer to its equilibrium orientation with the center of buoyancy above the center of mass, an effect observed in live microorganisms [118]. If the time scales for these two effects are comparable, the swimmer can translate. We visualize this conclusion by extending the geometric mechanics-based framework introduced in Chapter 2. This model allows for both simple computation and optimization in motion planning.

3.1 System description

The two-link swimmer model is illustrated in Fig. 3-1. Both links are assumed to be rigid and slender with length L and radius R. The swimmer is neutrally buoyant. The *drag arm* is massless, while the *buoyant arm* has mass m. This arm's mass is distributed such that the center of buoyancy is a distance l further than the center of mass from the joint, producing a buoyant moment on that arm. The system's shape is described by the angle α between the buoyant arm and the drag arm; its position

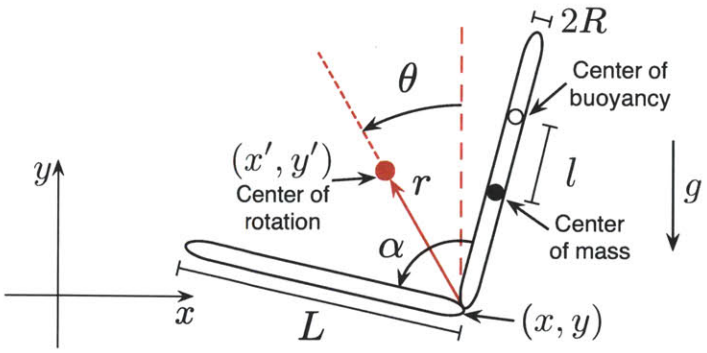

Figure 3-1: Schematic of the neutrally-buoyant, two-link swimmer with centers of mass and buoyancy separated by a distance l.

in the inertial reference frame is given by (x, y), the location of the joint axis, and the orientation θ of the medial line bisecting the swimmer, measured from the vertical.

If the centers of gravity and buoyancy were collocated, opening or closing the joint would only serve to propel the swimmer back and forth along its medial line. Separating the centers gives the system a tendency to return the buoyant arm to a vertical configuration and thus allows it to passively reorient between the opening and closing motions, producing a net displacement. The attractive feature of this mechanism lies in its simplicity which manifests as a passive response to a stationary field. Note that the swimmer can translate upwards against gravity.

3.2 Fluid dynamics and kinematics model

At the low Reynolds numbers we are considering, viscous drag forces dominate and inertial effects are negligible. As in Chapter 2, this has several key consequences we can exploit to represent the equations of motion in a concise manner. First, the net force on the swimmer is zero. Second, the drag forces acting on the system are linear in the velocities of the links, which are in turn linear in the system's shape and position velocities and independent of the location (but not the orientation) of the system in the inertial frame. Taken together, these properties form the force-balance

equation

$$\begin{bmatrix} F_g^x & F_g^y & F_g^\theta \end{bmatrix}^T = -\begin{bmatrix} F_d^x & F_d^y & F_d^\theta \end{bmatrix}^T = \beta^{3\times 4}\begin{bmatrix} v_x^b & v_y^b & v_\theta^b & \dot{\alpha} \end{bmatrix}^T \tag{3.1}$$

where F_g denotes the net generalized forces applied by gravity, F_d denotes the drag forces that balance these external forces, and $\beta(\alpha, \theta)$ is a linear map relating these forces to the system velocities.

Separating β into two sub-blocks as $\beta = [\beta_1^{3\times 3}\ \beta_2^{3\times 1}]$ allows us to rearrange (3.1) into a form

$$\boldsymbol{v}^b = \begin{bmatrix} v_x^b & v_y^b & v_\theta^b \end{bmatrix}^T = \mathcal{A}(\alpha, \theta)\dot{\alpha} + \mathcal{C}(\alpha, \theta), \tag{3.2}$$

where $\mathcal{A}(\alpha, \theta) = \beta_1^{-1}\beta_2$ linearly maps an input shape velocity $\dot{\alpha}$ to the resultant $\boldsymbol{v}^b$ position velocities, and $\mathcal{C}(\alpha, \theta) = \beta_1^{-1}F_g$ is an additional position velocity induced by the buoyant forces. Equation (3.2) is the reconstruction equation [13] and $\mathcal{A}$ the local connection for this system, similar to those presented for three-link systems in Chapter 2.

The two-link model has two notable differences from those previously developed [57, 73, 101]. We now include the *buoyant function* $\mathcal{C}$, which has not appeared previously and whose closest antecedent is the momentum terms included in works such as Ostrowski & Burdick [113] and Shammas, *et al.* [134]. We have chosen to express the reconstruction equation in terms of inertial-frame velocities, rather than the body-frame velocities used in the previous work. This choice, prompted by the dependence of $\mathcal{C}$ on θ regardless of the frame chosen, avoids any problems posed by integrating in a body frame to find the swimmer's trajectory [57]. Unfortunately, it also results in the unactuated orientation θ appearing on the right-hand side of the reconstruction equation, preventing the direct specification of the right-hand side input trajectories. In this chapter, we address these problems with a combination of analytical and numerical limit cycle analyses in the (α, θ) phase space of the swimmer.

As a prelude to this limit cycle analysis, it is useful to briefly review the physics of low Reynolds number swimming that give rise to Eq. (3.2), and to expand techniques we have previously developed for visualizing locomoting system dynamics [57] to

encompass the present system. In general, the β matrix that produces the drag forces in Eq. (3.1) can be found by solving Stokes equations around the links. For this analysis we once again assume a small aspect ratio, $R/L \ll 1$, and use resistive force theory [47] to approximate the drag forces acting on the links. As a reminder, with this model the lateral and longitudinal drag forces on each link are proportional to the lateral and longitudinal velocities by drag coefficients κ and $\kappa/2$, respectively.

Standard kinematic techniques [106] relate these velocities to the generalized coordinate velocities in Eq. (3.1) and also provide the rotations to bring them into a common frame for summation into F_d^x and F_d^y. The drag moments are handled similarly, with the note that F_d^θ is the sum not only of the rotational drag moments, but also of the moments resulting from the drag forces acting normal to the link. Resistive force theory does not capture long-range hydrodynamic interactions between the links or any viscous effects that arise from bringing the links close to each other, but it is useful for this initial investigation as it allows an analytical representation of the drag forces. Including the lowest-order long-range interactions by using slender body theory [30] was addressed in Chapter 2 and shown to have minimal effect when links maintain sufficient distance between them.

The gravitationally generated forces in Eq. (3.1) are similarly derived from the system geometry. Because the swimmer is neutrally buoyant, F_g^x and F_g^y are zero. The moment exerted on the system by the separated gravitational and buoyant forces is given by $F_g^\theta = mgl\sin(\alpha/2 - \theta)$.

Rescaling the equations of motion, we take the characteristic translational velocity of the system as ωL and the characteristic angular velocity as ω, where ω^{-1} is the characteristic time scale of our input "flapping" motions corresponding to a dimensionless time $\hat{t} = \omega t$. Combining these velocities in a dimensionless parameter $\gamma = (mgl)/(\kappa\omega L^2)$, corresponding to the ratio of gravitational and drag forces,

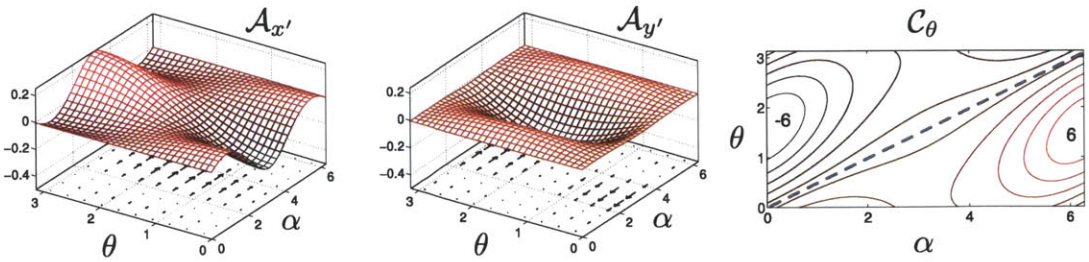

Figure 3-2: Visualization of the components of the equations of motion in (3.5) for $\gamma = 1$. Left: Connection vector fields for $\mathcal{A}_{x',y'}(\alpha, \theta)$, along with their curvature functions, capture the contribution to translation from changes in shape. Right: $\mathcal{C}_\theta(\alpha, \theta)$, represents the contribution to rotation from the buoyant moment. The dashed line indicates the equilibrium orientation.

Eq. (3.2) becomes

$$\begin{bmatrix} \hat{v_x^b} \\ \hat{v_y^b} \\ \hat{v_\theta^b} \end{bmatrix} = \frac{\sin(\alpha/2)}{3 - \cos\alpha} \begin{bmatrix} -\sin\theta \\ \cos\theta \\ 0 \end{bmatrix} \hat{\dot{\alpha}} + \frac{3\gamma}{3 - \cos\alpha} \begin{bmatrix} (\sin(\alpha - \theta) - \sin\theta)\cos\theta \\ (\sin(\alpha - \theta) - \sin\theta)\sin\theta \\ (3 + \cos\alpha)\sin(\alpha/2 - \theta) \end{bmatrix}, \quad (3.3)$$

revealing the characteristic trajectory of the system to be a function only of the chosen flapping motion $\hat{\dot{\alpha}}$ and the parameter γ. The dimensionless parameter γ has a second interpretation, relating the settling time of the swimmer to the characteristic time scale of flapping.

3.2.1 Optimal coordinates

Our choice of the medial line as the swimmer's orientation has a convenient effect on the form of Eq. (3.3). In these coordinates, the two links open and close symmetrically around the orientation line, which consequently does not rotate in response to changes in the joint angle; this symmetry leads to the third row of $\mathcal{A}$ being zero. The swimmer also has a second, less intuitive, symmetry that allows further reduction of the reconstruction equation. Because the gravitational forces are a pure moment applied to the system, they induce a rigid rotation of the swimmer about a shape-dependent center of rotation defined by the interactions of the drag forces on the links. By symmetry, this center of rotation is on the medial line, and we can most

easily calculate its distance r from the joint by recognizing that the moment-induced motion of the joint is along an arc around the center of rotation, and thus

$$\hat{r} = r/L = -\mathcal{C}_x/(\mathcal{C}_\theta \cos\theta) = 2\cos(\alpha/2)/(3+\cos\alpha). \tag{3.4}$$

Changing the reference location of the system from the joint to the center of rotation by selecting $(\hat{x}', \hat{y}') = (\hat{x} - \hat{r}\sin\theta, \hat{y} + \hat{r}\cos\theta)$ is a form of optimal coordinate choice [57], and has the effect of reducing $\mathcal{C}_x$ and $\mathcal{C}_y$ to zero, producing a new reconstruction equation,

$$\begin{bmatrix} \hat{v}_x^{b\prime} \\ \hat{v}_y^{b\prime} \\ \hat{v}_\theta^{b} \end{bmatrix} = \begin{bmatrix} \mathcal{A}_{x'}\hat{\dot{\alpha}} \\ \mathcal{A}_{y'}\hat{\dot{\alpha}} \\ \mathcal{C}_\theta \end{bmatrix} = \begin{bmatrix} -\sin\theta\left(\frac{\sin(\alpha/2)}{3-\cos\alpha} + \frac{\mathrm{d}\hat{r}}{\mathrm{d}\alpha}\right)\hat{\dot{\alpha}} \\ \cos\theta\left(\frac{\sin(\alpha/2)}{3-\cos\alpha} + \frac{\mathrm{d}\hat{r}}{\mathrm{d}\alpha}\right)\hat{\dot{\alpha}} \\ \frac{3\gamma}{3-\cos\alpha}(3+\cos\alpha)\sin(\alpha/2-\theta) \end{bmatrix} \tag{3.5}$$

in which the translational velocity is generated entirely by the local connection, and the rotational velocity is dictated exclusively by the buoyant terms.

3.2.2 Visualizing system dynamics and strokes

The components of the reconstruction equation in Eq. (3.5) are displayed graphically for $\gamma = 1$ in Fig. 3-2. The two leftmost plots represent the rows of the local connection $(\mathcal{A}_{x'}, \mathcal{A}_{y'})$ using the *connection vector field* metaphor previously described in Chapter 2. The dot products of an input $\hat{\dot{\alpha}}$ with the vector fields produce the contribution of the shape velocity to the position velocity, as per the first line in Eq. (3.5). The curls of the rows of $\mathcal{A}$ capture all the information about the net contribution of this opening and closing action over a full cycle. By Stokes' theorem, line integrals along closed loops, which represent cyclical body deformations, are equal to the area integrals of the fields' curls over the region enclosed by the loops. At the right of the figure, the contour plot illustrates $\mathcal{C}_\theta$ and can be interpreted as the prescribed rotational velocity imposed on the system by the buoyant moment.

The chief weakness of this form of the reconstruction equation is the presence of θ as an unactuated configuration component on the right-hand side. The first step in analyzing strokes for the swimmer, then, is to identify the limit-cycle behavior of

θ in response to given cyclic α inputs; once this behavior is found, the translatory component of the motion can be found by evaluating Eq. (3.5) for the corresponding (α, θ) trajectory.

To find this limit cycle, we take advantage of the structure of Eq. (3.5), specifically the property that the orientation trajectory is entirely defined by the buoyant moment, $\hat{\dot{\theta}}(\hat{t}) = \mathcal{C}_\theta(\alpha, \theta)$. For strokes covering large ranges of α, $\mathcal{C}_\theta$ is sufficiently nonlinear that we take recourse to numerical methods when solving for θ. For small strokes, however, we can find an analytical expression for this trajectory by linearizing the buoyant moment as $\mathcal{C}_\theta = k(\theta_n(\alpha) - \theta)$, where $k = 6\gamma$ acts as a linear restoring spring driving θ towards its equilibrium value of $\theta_n = \alpha/2$, indicated by the dashed line in the $\mathcal{C}_\theta$ plot in Fig. 3-2. This linearization then allows $\hat{\dot{\theta}}(\hat{t})$ to be rewritten as the ordinary differential equation

$$\hat{\dot{\theta}}(\hat{t}) + k\theta(\hat{t}) = k\alpha(\hat{t})/2. \tag{3.6}$$

We now select an input shape trajectory $\alpha(\hat{t}) = \alpha_0/2 + \alpha_0 \sin(\hat{t})/2$, i.e., a sinusoidal opening and closing motion with frequency determined by the characteristic time scale. Substituting this input into Eq. (3.6) and solving the differential equation produces the limit cycle for the θ trajectory corresponding to this input,

$$\theta(\hat{t}) = \frac{\alpha_0}{4} + \frac{\alpha_0 k}{4(1+k^2)}(k\sin(\hat{t}) - \cos(\hat{t})), \tag{3.7}$$

which depends only on the amplitude of the input α_0 and the parameter γ.

Together, $\alpha(\hat{t})$ and Eq. (3.7) form elliptical trajectories in the (α, θ) space, sheared such that the θ components of the tangent vectors are zero where the trajectory crosses the equilibrium line, and enclosing areas $a = (\pi\alpha_0^2 k)/(8(1+k^2))$ in the (α, θ) plane. Comparing these ellipses to exact integrals of Eq. (3.3) for the input in $\alpha(\hat{t})$, as in Fig. 3-3, shows the approximate trajectories to be a reasonable representation of the system behavior for input amplitudes of $\alpha_0 < 1.5$. At larger amplitudes, the nonlinearities in $\mathcal{C}_\theta$ start to play a significant role, with their first effect being a reduction in the restoring force below the equilibrium line. This reduction pulls the

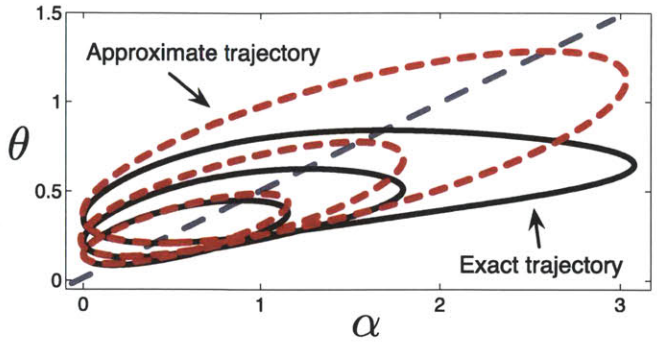

Figure 3-3: Comparison of exact stroke limit cycles with the shape predicted by the linearized model, for $\gamma = 1/6$ and $1.2 < \alpha_0 < 3.1$. Dashed lines indicate trajectories from the linearized solutions, solid lines indicate exact trajectories.

$\alpha_{\max}$ tips of the trajectories down to lower values of θ.

With the (α, θ) limit cycles in hand, we can now consider the efficiencies $\mathcal{E}$ of strokes at different amplitudes and frequencies, which we take as the ratio of the power required to pull the swimmer at its nondimensionalized mean speed $\hat{s}$ (relative to the flapping frequency) to the time averaged mechanical power applied through the joint to generate the system's motion [7]. Calculating this efficiency numerically is straightforward, generating the contour surface in Fig. 3-4. Note that $\hat{s}$ can be calculated either by integrating (3.5) or by using the area integrals of the curvature functions over the regions enclosed by the strokes to find the net displacement per cycle. The dominating features of this plot are the three peaks in efficiency for γ values between 10^{-1} and 10^{0}, when the time scales of flapping and settling are comparable. Mean speed, represented as a gradient surface behind the contours in Fig. 3-4, is closely correlated to the efficiency. This correspondence is explained by recognizing that $\hat{s}$ can alternately be taken as a measure of displacement per stroke, and thus as a kind of efficiency measure in its own right.

Independently, these peaks highlight the best choices of input amplitude and frequency to generate efficient motion. Combining them with information from the curvature functions in Fig. 3-2 provides further insight into several key features of the system dynamics. Physically, the curvature functions measure the extent to which reorienting the system breaks the time symmetry. By observing the interactions of

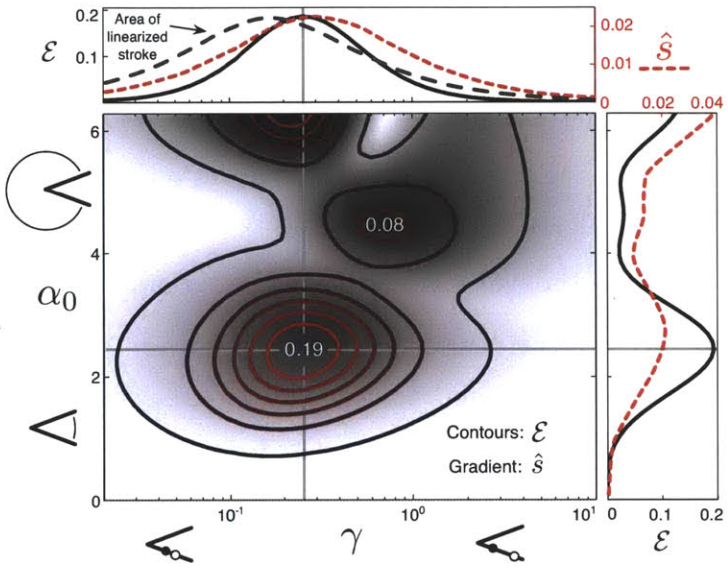

Figure 3-4: Contours: efficiency, $\mathcal{E}$, (in percent) of the system as a function of stroke amplitude α_0 and time scale parameter γ. Gradient background: dimensionless mean speed, $\hat{s}$. Top and side panels: qualitative comparison of the efficiency with the mean speed $\hat{s}$ of the system relative to the flapping frequency. The mean speed corresponds to the area integral of the curvature functions over the region of the (α, θ) space enclosed by the stroke; the top panel additionally presents the dependence of the enclosed area on γ for the linearized stroke.

the strokes with the curvature functions, we can elucidate the system behaviors that give rise to the peaks.

Starting at $\alpha_0 = 0$ and moving up the plot, the first peak represents optimal system behavior for $\alpha_0 < \pi$. For these amplitudes, the optimal γ values are very close to the values that maximize the area a enclosed by the (α, θ) trajectory, as illustrated in the top panel of Fig. 3-4. Returning to the curvature functions in Fig. 3-2, we see that for small strokes both curvature functions are positive-definite, and thus maximizing the area enclosed by the stroke maximizes the net displacement achieved over the control effort. The drift of the optimal efficiency towards larger γ values (i.e., strokes that are slower or settle more quickly) is largely explained by the differences between the true and linearized strokes noted in Fig. 3-3. Reducing the flapping frequency allows the system more time to reorient itself during the part of the cycle that passes through the low-magnitude region of $\mathcal{C}_\theta$, thus reducing the pinching effect on the larger trajectories.

The second peak's origins lie in the dependence of the curvature functions on α and θ. As the amplitude increases, the enclosed regions of the curvature function are no longer positive-definite. The newly-added negative regions (especially present for the y component) first cancel out the positive contributions, causing a dip in efficiency, and then grow to dominate the solution at the second peak. Strokes near this peak spend the majority of their cycle in the low-magnitude region of $\mathcal{C}_\theta$, pushing the peak's γ value significantly above the optimum for the linearized strokes.

Finally, the third peak reflects a similar dip and increase in the area integral magnitudes, with very large strokes enclosing a significant negative region of the y curvature function. This final increase in amplitude also places the stroke back in larger-magnitude regions of $\mathcal{C}_\theta$, pulling the peak's maximum efficiency back down to lower values of γ (i.e., strokes that are faster or settle more slowly). As compared to the first peak, strokes near this peak have greater displacement over each cycle (and thus a greater mean speed $\hat{s}$), but this increased displacement is not enough to offset the increased control effort, leaving the first peak as representing the most efficient motion.

3.3 Comparison to the three-link swimmer

While the same basic framework was applied to the three-link swimmer (Chapter 2) and the two-link swimmer, a fundamental difference appeared to treat the unactuated degree of freedom. Unlike in the case of the three-link swimmer, we were not given the freedom of choosing a stroke exactly for the two-link swimmer. Instead, we prescribed the actuated degree of freedom (the joint angle) and solved for the resulting unactuated degree of freedom, the orientation. Further, at low Reynolds number, timing on strokes can often be ignored. Executing a stroke for the three-link swimmer at one speed and at twice that speed will result in the same net displacement. The same is not true for our two-link swimmer, which fundamentally depends on timing due to the gravitational reorientation that is responsible for achieving any non-zero net displacement.

Chapter 4

Curvature and the serpenoid swimmer

The theory and framework presented in Part I are applicable to any system that may be described by shape parameters and whose equations of motion may be written in the form of the reconstruction equation (2.8). However, visualizations of the system dynamics, such as the connection vector fields and constraint curvature functions introduced in Chapter 2, are limited to systems with a two-element parameterization of the shape. As we will demonstrate in this and the following chapters, with just two parameters we can describe a wide range of continuously deformable (flexible) systems. Here we explore the serpenoid swimmer at low Reynolds number, a system that has a shape comprised of sinusoids in the curvature space. We find the visualizations of the system dynamics for this swimmer and compare its optimal performance to that of the three-link swimmer.

4.1 The curvature space

For flexible systems, it is convenient to work in the curvature space of the system's shape, $\kappa(s)$, where s is the arclength along the swimmer. Curvature is related to the system's shape through the spatial rate of change of the unit tangent vector, $\mathbf{T}(s,t)$, along the length of the system or $\kappa(s,t) = d\mathbf{T}(s,t)/ds$. The shape resulting

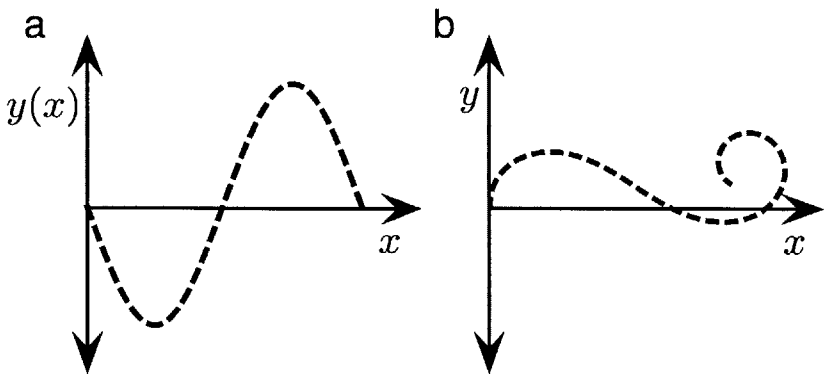

Figure 4-1: a) A shape described by a function $y(x)$, where every x corresponds to a unique value of $y(x)$. b) A shape that cannot be described by $y(x)$ because for some x values, there exist multiple values of y.

from curvature is found by solving the following set of coupled ordinary differential equations:

$$\begin{aligned} \frac{d\theta(s,t)}{ds} &= \kappa(s,t) \\ \frac{dx(s,t)}{ds} &= \sin\theta(s,t) \\ \frac{dy(s,t)}{ds} &= \cos\theta(s,t). \end{aligned} \tag{4.1}$$

Examining curvature along the length of the system offers several advantages over describing the shape as a function such as $y(x)$ in Fig. 4-1. Limiting the representation of the swimmer to a function restricts the shape of the swimmer, eliminating the possibility of highly curved shapes like that in Fig. 4-1b, and requires additional constraints to preserve the length of the swimmer for all shapes in time. Moving to the curvature space allows us to model flexible systems such as flagella and highly-articulated systems with coupled joint angles.

To represent a system's kinematics—its shape moving in time—we will use the curvature $\kappa(s,t)$, a function of both space (along the system's body length) and time. This curvature can be decomposed into N spatial and temporal components, or the

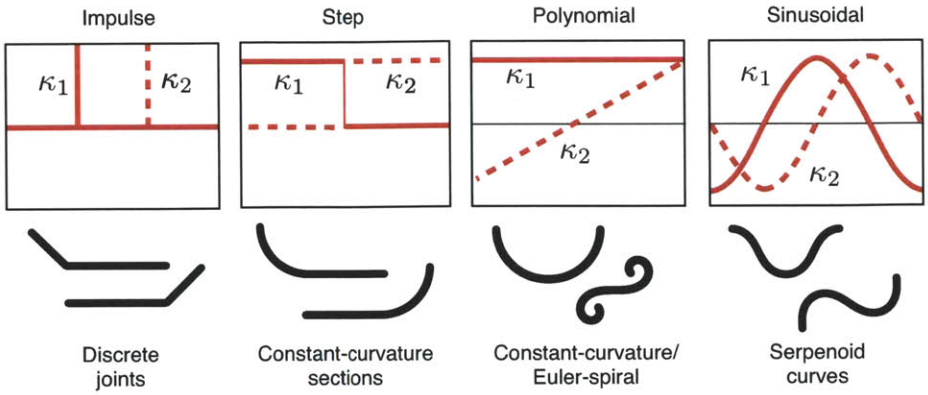

Figure 4-2: Basis functions in the curvature space along the length of the swimmer allow an extensive range of shapes. The resulting shapes of a swimmer using (from left to right) Dirac delta, Heaviside (step), polynomial, and sinusoidal functions. Courtesy of Ross Hatton.

curvature basis functions, $U_i(s)$, and their amplitudes, $a_i(t)$, respectively:

$$\kappa(s,t) = \sum_{i=1}^{N} a_i(t) U_i(s), \tag{4.2}$$

where the set of $a_i(t)$ are the dimensionless shape parameters. The curvature basis functions $U_i(s)$ have units of curvature, are predetermined, and stay constant in time. For a system with two degrees of freedom, $N = 2$ and Eq. (4.2) becomes

$$\kappa(s,t) = a_1(t)U_1(s) + a_2(t)U_2(s), \tag{4.3}$$

where $a_1(t)$ and $a_2(t)$ are comparable to the joint angles α_1 and α_2 for the three-link swimmer. In that case, the basis functions to represent two discrete bends in the curvature space along the swimmer correspond to two Dirac delta functions, one at each joint of the system (Fig. 4-2). The amplitude of the Dirac delta function in time determines the joint angle [59]. These shape parameters define the shape space and together, they describe shape changes for the system. If $a_1(t)$ and $a_2(t)$ are periodic, the shape change they define is a gait. Fig. 4-2 illustrates a variety of curvature basis functions for $N = 2$ and corresponding mode shapes including

Heaviside (step), polynomial, and sinusoid functions, where the free parameters are typically the amplitudes of the basis functions.

Shapes created by sinusoidally varying curvature (Fig. 4-2) are termed 'serpenoid' curves and are commonly considered in the snake robot literature [152]. The corresponding shape space for a serpenoid swimmer, a swimming system represented by serpenoid curvatures, is illustrated in Fig. 4-3a. These shapes are somewhat biological in nature, representative of typical 'snake-like' shapes. For the remainder of this chapter, we will model and visualize the dynamics of the serpenoid swimmer using the framework introduced in Chapter 2.

4.2 Dynamics visualization and optimal strokes

Comparing two systems, such as the three-link swimmer and the continuously deformable serpenoid swimmer, is typically done by focusing on the optimal strokes of each. Applying the framework presented here, we can perform a more global comparison. A complete visualization of the dynamics is straightforward to obtain in both cases. To form the kinematic reconstruction equation (2.8), we assume the serpenoid swimmer can be approximated (locally) as a circular cylinder and again use resistive force theory (§2.2.1) for low Reynolds number motion to find the hydrodynamic forces and torques on the swimmer. As in §2.2.3-§2.2.4 for the three-link swimmer, we find the net force and torque on the system, set those expressions to zero, and solve for the body velocity $\boldsymbol{v}^b$ to find:

$$\boldsymbol{v}^b = -\mathcal{A}(\boldsymbol{a})\, d\boldsymbol{a}. \tag{4.4}$$

Fig. 4-3b shows the curvature constraint functions of the serpenoid swimmer in minimum perturbation coordinates (§2.2.8) and the corresponding optimal stroke in the x, y and rotation directions. The maximum efficiency stroke is compact, round, and is centered around the peak. The y and θ optimal maximum efficiency strokes are figure eight strokes, taking advantage of the symmetry readily apparent from the curvature functions by reflecting across the axis of symmetry to double the distance traveled per cycle. The performance of the continuously deformable swimmer is noticeably higher

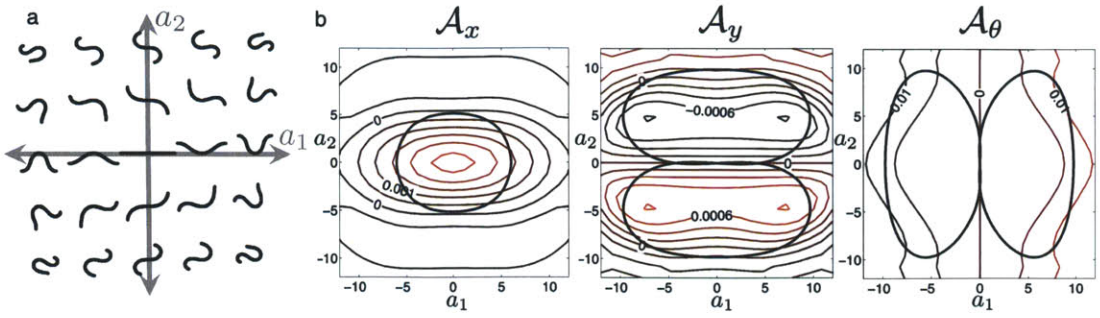

Figure 4-3: a) The shape space for the serpenoid swimmer, using sinusoidal basis modes in the curvature space to parameterize the system. b) Constraint curvature functions and optimal efficiency strokes for the serpenoid swimmer in the x, y and rotational directions. The three maximum efficiency strokes are all centered at the origin of the shape space and take advantage of the two-fold rotational symmetry in each constraint curvature function. The strokes in y and θ are figure eight shaped due to the odd rotational symmetry present for those curvature functions.

than the three-link swimmer: the optimal translational efficiency for the serpenoid swimmer is 278% of the three-link swimmer's maximum efficiency.

4.3 Beyond serpenoid curves

The straightforward application of our visualization framework and substantial improvement in efficiency of the serpenoid swimmer over the three-link swimmer is encouraging and naturally leads to several questions, including: What are optimal basis functions? Can we extend this analysis to biological systems? Do biological systems perform optimally, given their morphology? How can we represent biological motion using just two parameters?

We begin to address these questions in Part II. We develop a general method of determining the curvature basis functions that best mimic biological behavior and apply this method to sea urchin spermatozoa. In Chapter 6, we narrow our focus on the representation of biological kinematics and what we can infer by examining the curvature basis functions for systems in changing environments and during different biological processes.

Part II

Kinematic analysis of biological systems

Chapter 5

Kinematic decomposition

Swimming strategies exhibited by animals consistently outperform man-made underwater vehicles, as illustrated by Fig. 1-1. While many bio-inspired underwater robots are modeled after these animals (e.g., [27, 31, 37, 65, 94, 95, 98, 110, 146, 148, 153]), it remains a challenge to reconcile the inherently discrete nature of mechanical components used in robots with the continuously deformable shape of biological systems. Snake robots, for instance, may have several joints and actuators to enable smooth 'snake-like' motion, but we still desire low-dimensional representations of the kinematics to allow fast and effective motion planning and gait optimization. One solution is to couple the joint motion and reduce the degrees of freedom in the system considerably (as in [62]), allowing these tasks to become manageable in finite time.

The state-of-the-art for describing biological kinematic motion includes measuring an animal's motion and extracting a number of kinematic parameters (e.g., velocity, tail beat frequency, wavelength and wave speed of traveling waves down the body, and amplitude of several points along the body [83]), fitting the kinematics to sines and cosines [116], or plotting the kinematics (as illustrated in Fig. 5-1b and c, either through a time lapse image of the changing body shape in time or through the curvature matrix directly). These methods require anywhere from 8 to 30 parameters. Here we consider complex biological systems and ask: How can we represent the system's shape using only a few parameters in time?

In this chapter, we develop the *kinematic decomposition*, a novel method to de-

scribe the kinematics of inherently complex systems with generalized curvature decomposition. We apply this method to sperm of the sea urchin *Arbacia punctulata*, a model organism shown in Fig. 5-1a, to explore *chemotaxis* (the directed movement in the presence of an attractant gradient) and identify the flagellar mechanics and gait modulation that leads to turning. Further, we develop a metric to identify whether or not the sperm is chemotaxing using kinematics alone.

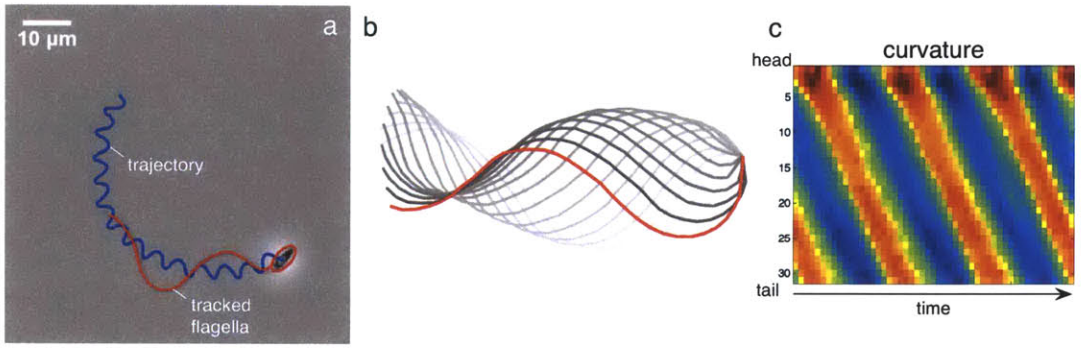

Figure 5-1: a) The shape of the sea urchin sperm flagella and the trajectory are tracked from high-speed microscopy images [50]. b) The kinematics of the sea urchin sperm are illustrated by a time-lapse of the flagella shape in time. c) A typical visualization of flagella kinematics is created by directly plotting the curvature matrix. Each column represents the curvature of the flagella at that time step. General trends and periodicity are easily obtained from plotting the curvature matrix, but more detailed analysis and comparison is difficult.

5.1 Spatial curvature

The initial step in our analysis is to calculate, filter, and normalize (by body length) the spatial curvature of the sea urchin sperm flagella at every time step, or $\kappa(s,t)$ as in Chapter 4. Working in the curvature space automatically simplifies our analysis, as we now analyze kinematics along the body and can ignore the orientation and distance of the body from the origin. The curvature space also allows us to accurately describe highly curved shapes like those in Fig. 4-1b.

We describe the flagella curvature with S points along the body that change in time for T time steps. The S spatial points always correspond to the same distance

along the body, such that the first point is at the base of the head and the last is at the end of the flagella. We express this curvature as a discretized form of the previous curvature equation (4.2),

$$\kappa[s,t] = \sum_{i=1}^{N} a_i[t]U_i[s], \tag{5.1}$$

where the square brackets indicate that space and time are now discrete and N is the number of basis functions and terms included. The spatial basis functions $U_i[s]$ are multiplied by the coefficients $a_i[t]$ at each time step to represent the contribution of that basis function to the motion of the sea urchin sperm. If $N = S$, the number of basis functions equals the number of spatial points and we have sufficient degrees of freedom to describe the curvature exactly. We have the freedom to choose $U_i[s]$ and by selecting optimal basis functions (those that best describe the motion), we can minimize N and use fewer parameters to accurately capture the kinematics. We aim to use just two parameters, $N = 2$, so that we may take advantage of the visualization framework and tools developed in Part I.

A common choice for spatial basis functions are Fourier modes, or sines and cosines. Fourier modes are orthogonal, successfully create snake-like shapes (as seen in Chapter 4 for the serpenoid swimmer) and therefore may also represent the motion of sea urchin sperm well. Fig. 5-2b illustrates the mean absolute error induced by using N Fourier modes to capture the curvature of the sea urchin sperm. Overall, Fourier basis functions reproduce the dominant features of the sea urchin sperm. However, when limited to a small number of basis functions, or small N, the Fourier modes fail to represent more extreme motions, such as when the curvature at the head of the sperm is small while the tail's curvature is very large, as in Fig. 5-2a. In this example, $N = 2$ so that $U_1[s] = \sin[s]$ and $U_2[s] = \cos[s]$.

5.2 Singular value decomposition (SVD)

Rather than selecting known functions like sines and cosines for basis functions, we wish to find optimal basis functions, those functions that account for the greatest

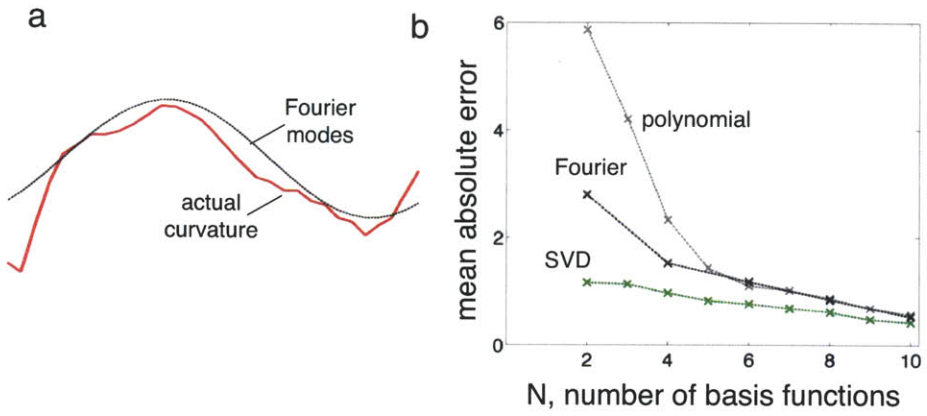

Figure 5-2: a) Fourier basis functions (dashed black line) fail to capture the features present in the actual curvature (solid red line) in representing the curvature of the flagella. b) Using the basis functions from the kinematic decomposition to represent the curvature gives the smallest mean absolute error, when compared to Fourier or polynomial basis functions.

amount of variability in curvature. The singular value decomposition (SVD) does precisely this operation. By applying an SVD to our data, we can identify the optimal bases, $U_i[s]$, and the corresponding amplitudes in time, $a_i[t]$.

In general, the SVD factors an m x n matrix M into three matrices:

$$M_{(m,n)} = U_{(m,m)}\Sigma_{(m,n)}V^*_{(n,n)} \tag{5.2}$$

where $U_{(m,m)}$ are the left singular vectors, a set of orthonormal basis vectors, $\Sigma_{(m,n)}$ is a diagonalized matrix of singular values ($\sigma_{i,i}$) in decreasing order, $V_{(n,n)}$ are the right singular vectors and * denotes the conjugate transpose. $U_{(m,m)}$ and $V_{(n,n)}$ are both unitary matrices, so that $UU^* = U^*U = I$ and $VV^* = V^*V = I$. This sets the scaling of U, V, and $\sigma_{i,i}$.

$M_{(S,T)}$ is a matrix populated by the spatial curvature at each time step, filled column-wise, so that S is the number of spatial points and T is the number of time steps, as shown schematically in Fig. 5-3a. (Note that this matrix is exactly the matrix illustrated in Fig. 5-1c). For all of our tracked biological data, there are more time steps than spatial points along the body ($S < T$). We will assume this

relationship holds when considering the details of our analysis, though the analysis is general for any matrix size. The matrices that result from the SVD are very powerful: the columns of $U_{(S,S)}$ are directly the optimal curvature basis functions, the diagonal elements of $\Sigma_{(S,T)}$ indicate the variability accounted for by each basis function, and $\Sigma_{(S,T)}V^*_{(T,T)}$ gives the corresponding amplitudes of the basis functions at each time step. Including all S basis functions guarantees that the curvature is exactly reproduced.

We are interested in representing kinematics using only a few parameters in time and will therefore limit the number of basis functions. For now, we set that limit to $N = 2$, but our method is general for any N up to S. In most cases, including just a few of the basis functions associated with the largest singular values will capture a bulk of the original motion. With two functions, the discretized curvature equation (5.1) becomes

$$\kappa[s,t] \simeq \sum_{i=1}^{2} a_i[t]U_i[s] = a_1[t]U_1[s] + a_2[t]U_2[s]. \tag{5.3}$$

We can quantify how well using N basis functions represents the exact kinematics by computing the fraction of variance represented, $\mathcal{V}_N$, with the singular values:

$$\mathcal{V}_N = \frac{\sum_{j=1}^{N} \sigma_j}{\sum_{i=1}^{S} \sigma_i}, \tag{5.4}$$

where σ_i is the ith singular value or the (i,i)th entry of the $\Sigma_{(S,T)}$ matrix. Again, the singular values are sorted such that $\sigma_1 > \sigma_2 > ... > \sigma_S$ and the basis functions representing the largest variance are first. When all of the basis functions are utilized, $\mathcal{V}_{N=S} = 1$, or all of the system's motion is described.

Fig. 5-3 illustrates the output of applying an SVD to spatial curvature data in time. The basis functions $U_1[s]$ and $U_2[s]$ (Fig. 5-3b) represent the spatial component of the kinematics, while the basis function amplitudes, $a_1[t] = \Sigma_{1,T}V^*_{T,T}$ and $a_2[t] = \Sigma_{2,T}V^*_{T,T}$ represent the temporal kinematic component (Fig. 5-3c). The shape space corresponds to the U_1 and U_2 basis functions and illustrates the family of possible shapes achievable, as in Fig. 5-3d. Overlaying the strokes onto the shape space is

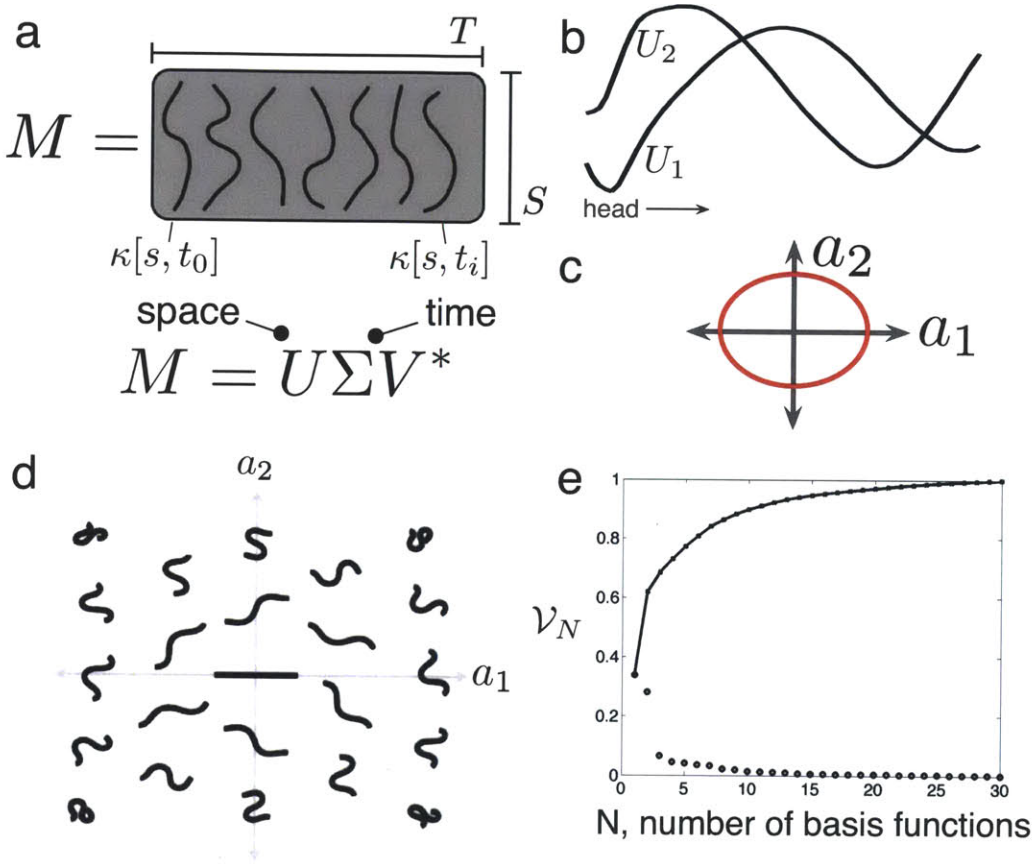

Figure 5-3: a) The matrix M is populated with the curvature at each time step, $\kappa[s,t]$. Performing an SVD on M separates the time dynamics and the spatial dynamics of the kinematics. U is a matrix of curvature basis functions. b) The first two basis functions account for the most variance, $U_1[s]$ and $U_2[s]$, and are illustrated here. c) The dynamics associated with the first two basis functions are visualized by a stroke in the shape space, $a_1[t]$ and $a_2[t]$. d) Together, the first two curvature basis functions resulting from the SVD, U_1 and U_2, form a shape space to represent the achievable shapes from some combination of those basis functions. e) The variance accounted for by each basis function is calculated as $\mathcal{V}_N$ in (5.4). The first two basis functions are responsible for over 60% of the variability, while the third (and higher) basis function contributes far less energy than the each of the first two basis functions.

a convenient method of visualizing the kinematics of the system, as we see through several examples in Chapter 6. Fig. 5-3e shows the variance accounted for by including additional basis functions. With only two basis functions, over 60% of the variability is represented, while higher basis functions contribute significantly less to the overall motion. The mean absolute error incurred by using SVD basis functions is illustrated in Fig. 5-2b. Basis functions from the SVD outperform Fourier and polynomial basis functions in representing flagellar curvature for any N. For large N, the difference becomes negligible, but for $N = 2$, the error associated with SVD basis functions is approximately half the error of Fourier basis functions.

Given a set of basis functions, we can project the motion of any system onto those basis functions. This calculation is convenient when comparing the strokes of several systems, as we require the strokes to be in the same shape space for a meaningful comparison. If the curvature data for system 1 at one time step is a vector $\vec{Q}$ of length S and the basis functions from system 2 are described by a subspace R, an orthonormal basis of vectors S in length, then the projection of $\vec{Q}$ onto R is described as

$$\text{proj}_R(\vec{Q}) = R(R^*R)^{-1}R^*\vec{Q}. \tag{5.5}$$

The result of this operation is a vector of coefficients (one element for each basis function) included in the subspace. Repeating this operation for each time step results in the strokes of system 1 projected onto the basis functions of system 2.

5.2.1 Comparison to existing methods

The process of performing an SVD on a data matrix is related to other tools, such as Proper Orthogonal Decomposition (POD) or Principal Component Analysis (PCA). These methods are used to determine the principal components of a signal via orthogonal transformation [68, 84]. Empirical Orthogonal Functions (EOF) is another closely related method, often used in geophysics to track scalar variables such as temperature or pressure, in both space and time. Depending on the application, the decomposition may be performed on mean-centered data or a data covariance matrix

[12, 84]. For a kinematic decomposition of curvature, the *mean* of the curvature data is significant. A non-zero mean curvature contributes to the overall shape through the non-linear transformation between curvature and body shape, a relationship described in Eq. (4.1). Mean-centering our data would result in a loss of useful information.

With a data covariance matrix, the matrix is square and an eigenvalue decomposition factors the matrix. Recall that the SVD of a matrix yields $M = U\Sigma V^*$. The eigenvalue decomposition of the covariance matrix from M is $eig(MM^T) = U\Sigma^2 U^*$ while $eig(M^T M) = V\Sigma^2 V^*$. Together, both eigenvalue decompositions of the covariance matrices M^*M and MM^* give identical results to the kinematic decomposition (that is, the matrices U, Σ, and V), though the SVD offers a more compact analysis, as only one decomposition is needed to recover all three matrices [84]. Taking advantage of "economic" SVDs, or SVDs that only compute the largest singular values and their associated vectors, tremendously reduces the computational cost of this operation. In MATLAB, these efficient decompositions are accessed through `svd(M,0)` and `svds(M)`, respectively.[1] Best practices for implementing the kinematic decomposition are detailed in Appendix A.

The application of decompositions to biological kinematic analysis is novel. The closest antecedent is work by Stephens, *et al.* [139], who examined the shape of *C. elegans* crawling on agar gel. The authors of this study used mean-centered curvatures and performed an eigenvalue decomposition on the covariance matrix with the goal of representing kinematics in reduced dimensions. They focused on the four "eigenworms," or spatial basis functions, that result from the eigenvalue decomposition. These four functions account for 95% of the variance for crawling *C. elegans.* Further, Stephens *et al.* considered the time dynamics of kinematics by examining the probability density function of the amplitudes for the first two basis functions. For a physical locomotion model, they related the time derivative of body curvature (the "phase velocity") to the crawling speed through a Brownian motion model. The major distinction in our work is through our analysis and process—we consider swimming

[1]Note that $\mathcal{V}_N$ in (5.4), the variance account for by N basis functions, cannot be calculated if only the largest singular values and their associated vectors are computed. Instead, singular values can be compared to each other to gauge the relative importance of their basis function vectors.

(rather than crawling) organisms, avoid mean-centering the curvature, apply an SVD to the data directly, and are able to study the physics through the resistive force theory model described in Chapter 2. Several studies utilize POD and PCA to perform analysis on complex structures, such as the work by Bozkurttas *et al.* [15] where the authors tracked approximately 280 points on a pectoral fin of a sunfish for 20 frames and were able to reconstruct the motion using just five basis functions. Other studies identify dominant frequencies within a parameterized gait. Gong *et al.* [45] employed the two-dimensional Fast Fourier Transform (FFT) to examine the frequencies of a wave surface comprised of joint angles along the snake robot's body and identified the dominant temporal and spatial frequencies of a parameterized sidewinding gait. Reducing the dimensionality of the model enables identification of a tunable parameter used to successfully control the turning radius of the snake robot. Kinematic decomposition is conceptually similar to the idea in legged locomotion from Full & Koditschek [43] of "templates," simple, low-dimensional representations of a locomoting system to enable easier modeling and optimization, though kinematic decomposition finds the best "template" based on the motion of an existing system.

Kinematic decomposition, or the method of applying an SVD to a matrix describing kinematics in time, is a powerful and general method that can be applied to a number of systems. In this thesis, we will apply kinematic decomposition to sperm, eel, trout, and *C. elegans*. These methods are also straightforward to apply to systems with discrete bending, such as terrestrial locomotion like human walking, where the columns of the data matrix are filled with the joint angles of the ankle, knee, hip, shoulder, elbow, wrist, etc. rather than calculated curvature.

5.3 Visualization of sea urchin spermatozoa dynamics

Arbacia punctulata sperm are approximately 50μm in length and swim at an average speed of 200μm/s in water or at a Reynolds number of approximately 10^{-2}. Therefore,

if we can successfully represent the kinematics with just two parameters, the low Reynolds number fluid dynamics models and visualization framework developed in Part I are appropriate to apply here. Tracked midline data of swimming *Arbacia punctulata* sperm were provided by J.S. Guasto from high speed (750 fps) microscopy video. A still image is shown in Fig. 5-1a. These experimental methods are detailed by Guasto *et al.* in [50].

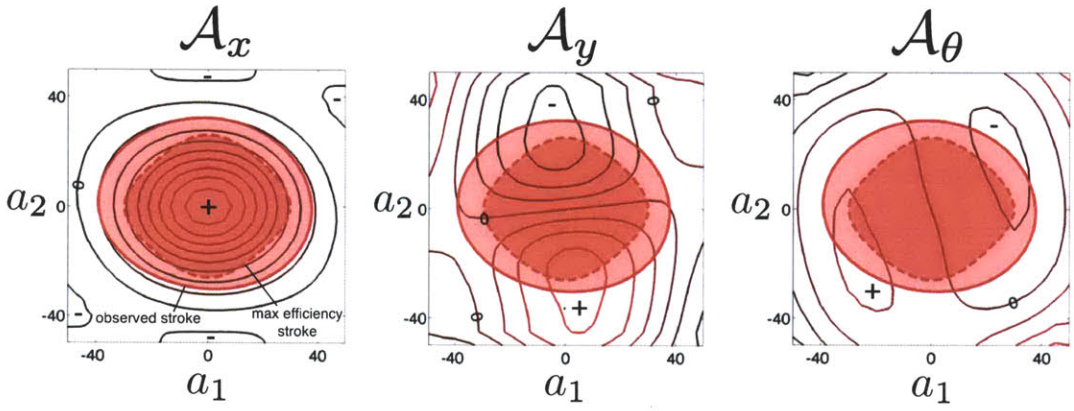

Figure 5-4: The constraint curvature functions for sea urchin (*Arbacia punctulata*) sperm reveal two-fold rotational symmetries in the x, y, and rotational directions. The empirical stroke (solid red line) is slightly broader than the maximum efficiency stroke for x (dashed red line), but lies almost entirely within the zero contours of x. The maximum efficiency stroke is just 17% more efficient than stroke observed in situ.

Again, we approximate the flagella locally as a circular cylinder and use resistive force theory to model the relative lateral and longitudinal forces acting on the swimmer [47]. The constraint curvature functions for the *Arbacia punctulata* sperm in the x and y translational directions and θ rotational direction are illustrated in Fig. 5-4. We can quickly learn about the system dynamics from these three plots. First, each of the three directions possess two-fold rotational symmetry. Therefore, we can predict the net motion resulting from any two-fold rotational symmetric stroke centered at $(a_1, a_2) = (0, 0)$: this stroke would move the system in the positive x direction because the x curvature function is evenly symmetric and encloses a non-zero net volume. The y and θ curvature functions possess odd rotational symmetry, so the net volume enclosed by a stroke is zero and there is no net motion in the y or θ directions.

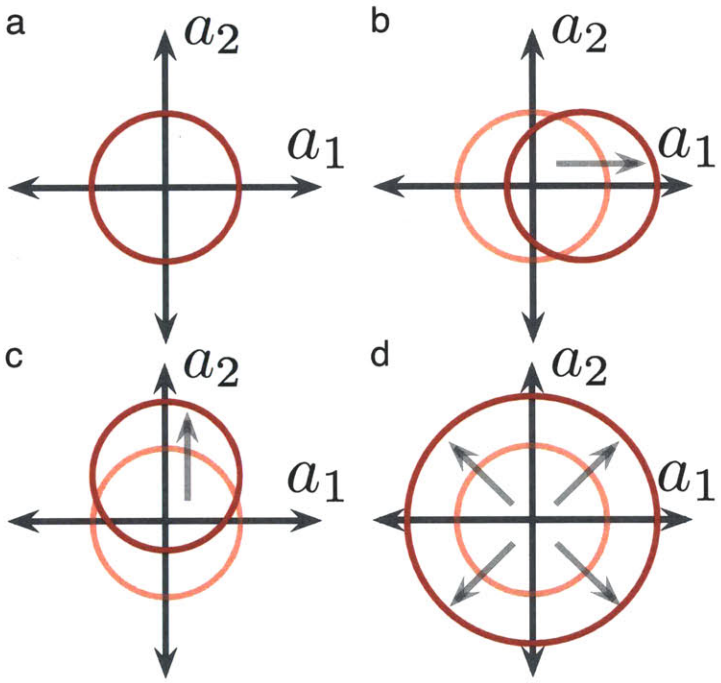

Figure 5-5: Considering the corresponding constraint curvature functions in Fig. 5-4, we can predict the net motion that results from a variety of strokes for sea urchin sperm. a) A centered, circular stroke encompasses non-zero net volume of the curvature constraint functions (Fig. 5-4) in the x direction only, therefore this stroke moves the system forward. b) Shifting the stroke along the a_1 axis increases turning and c) shifting the stroke vertically along the a_2 axis increases motion in y and θ. d) Increasing the amplitude of the centered stroke moves the sea urchin sperm farther per stroke in the x direction.

Considering perturbations from this basic stroke and the constraint curvature functions in Fig. 5-4, we can extract information about how the system will behave for a wide range of strokes. For simplicity, we will compare motions to a circular stroke centered at the origin, illustrated in Fig. 5-5a. If this stroke is perturbed by a positive offset along the a_1 axis (as in Fig. 5-5b)—we expect a slight reduction in x motion, a slight increase in y, and a small, positive rotational net motion, as the changes in the net motion of sea urchin sperm are reflected by the change in volume enclosed by the stroke on the curvature functions in Fig. 5-4. If, instead, the stroke is offset positively along the a_2 axis (as in Fig. 5-5c), the net motion will be less in x, negative in y, and slightly positive in θ. We can glean from this analysis that moving the stroke along the a_2 axis has an impact on both net rotation and vertical displacement and moving the stroke along the a_1 axis has a larger impact on net rotation than vertical displacement. Therefore, if we could control the stroke of a sea urchin sperm and desired net rotation over each stroke, we would introduce a constant offset to $a_1[t]$ to enclose more net volume in the θ curvature function.

Now we consider the effect of changing the amplitude of our circular, centered stroke (Fig. 5-5d). Increasing the amplitude of the stroke increases net motion in x until the stroke crosses the zero contour. At that point, the net volume enclosed by the stroke begins to decrease. Net motion in y and θ remains at zero due to the odd two-fold rotational symmetries in the y and θ constraint curvature functions.

As in Chapters 2-4, we find the $a_i[t]$ that results in the maximum efficiency stroke for the $U_i[s]$ basis functions, using the efficiency definition described in §2.3.2. For the first time, we can compare this stroke to an empirical stroke. The strokes overlaid onto Fig. 5-4 are the observed stroke (projected onto the $U_1[s]$ and $U_2[s]$ basis functions) and the optimal efficiency stroke. We find that the maximum efficiency stroke is slightly more compact and just 17% more efficient than the stroke observed. The observed stroke is slightly off-centered along the a_2 axis, signifying that some of the energy the sea urchin sperm puts into this stroke results in net rotation. Net rotation does not contribute to 'useful work' (the numerator in our translational efficiency metric).

5.4 Chemotaxing

During fertilization, a sperm must identify and locate an egg to succeed in transferring genetic material. Sperm have the ability to sense chemical attractants released from eggs, thereby initiating oriented behavioral movement towards the attractant source, termed *chemotaxis*. Chemotaxis and fertilization have both been well studied (e.g., [1, 44, 63, 75, 102, 162, 171]), however the relationship between the internal response of the organism and locomotion is still not well understood. Motility of sperm has been of interest in the fluid dynamics and biology literature for several decades [14, 17, 47, 49, 85, 144, 145].

When a cell encounters a chemoattractant plume, the attractant binds to a receptor on the cell surface initiating an intracellular transduction cascade involving calcium (Ca^{+2}) signaling that propagates throughout the flagella. As a result, dynein motors in the flagella generate internal stresses, deforming the flagellum. The internal stresses are balanced by elastic restoring forces in the flagella and hydrodynamic drag from the fluid. These stresses are indicative of the local flagellar curvature. Changes in curvature lead to the organism's net displacement and turning towards the attractant gradient [2, 85, 125].

Recently, several studies have focused on the role of Ca^{+2} during chemotaxis in various organisms [28, 29, 51, 169]. Alvarez *et al.* [2] found that the curvature of the sperm's trajectory is modulated by the time rate of change of Ca^{+2} within the cell. Therefore, the gradient of attractant initiates intracellular signaling and this leads to directed motion towards high concentrations of attractant. However, the biomechanics in this process remains unclear: How do the flagella respond to the intracellular signaling? How is this response related to the locomotion? These questions are ultimately questions of kinematics and are answered using kinematic decomposition.

5.4.1 The mechanics of turning

By applying the kinematic decomposition to the *Arbarcia puntulata* data, we conveniently decouple the spatial and temporal characteristics of the kinematics and can now visualize the time dynamics alone. We examine $a_i[t]$, the coefficients of the basis functions. The amplitudes for the first few basis functions are periodic and regular. They are well represented by a first-order Fourier series approximation, $a_i[t] = \mathsf{a}_{i,0} + \mathsf{a}_{i,1}\cos[t] + \mathsf{b}_{i,1}\sin[t]$. These parameters ($\mathsf{a}_{i,0}, \mathsf{a}_{i,1}$ and $\mathsf{b}_{i,1}$) control the stroke offset and size, respectively.

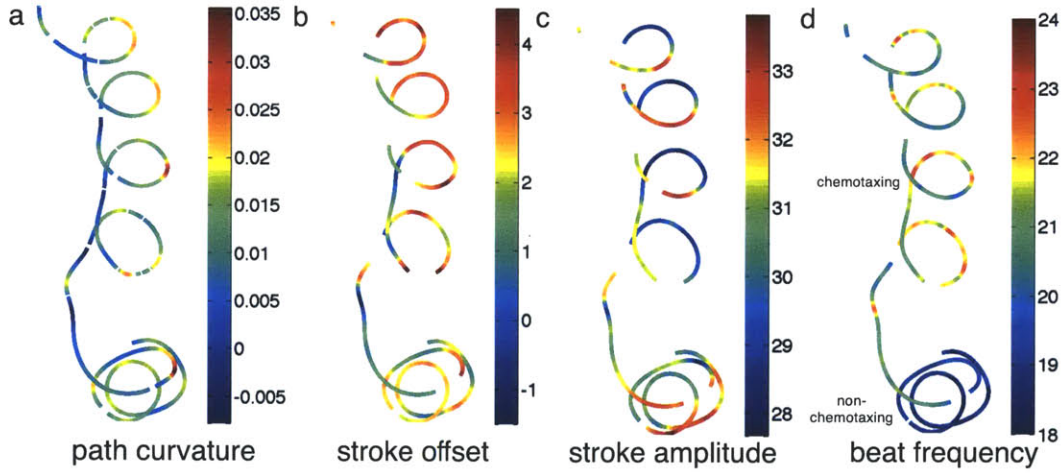

Figure 5-6: a) Curvature of the sperm's path. Alaverez *et al.* [2] demonstrated that path curvature and propagation of Ca^{+2} along the flagella, a response to sensing attractant, are correlated. b) The stroke offset shown is left-right offset along the a_1 axis. When the sperm travels straight, towards the attractant, the stroke offset is small, while a large offset results in turning, or higher path curvature. c) Stroke amplitude is calculated as the widest dimension of the stroke over one tail beat. As the sperm senses a gradient of attractant, the stroke grows in size and it moves more quickly toward the higher concentration of attractant. d) Beat frequency clearly demonstrates the onset of chemotaxis. Once the sperm senses the gradient of attractant, beat frequency increases by about 30%. These trends are consistent with what is observed in the curvature functions: to turn, the stroke must be offset and large. To move forward, the stroke need not be large, but should be centered.

Fig. 5-6 illustrates the stroke parameters with reference to the trajectory of the sea urchin sperm. Left-right stroke offset is calculated as $\mathsf{a}_{1,0}$ in Fig. 5-6b and stroke amplitude (Fig. 5-6c) is measured as the widest dimension of the stroke over one tail

beat. As predicted from the curvature functions in Fig. 5-4 and model strokes in Fig.5-5, the greater the stroke offset, the more tightly the sea urchin sperm turns. This observation offers a biomechanical explanation to Alvarez *et al.* [2] who demonstrated that path curvature and rate of Ca^{+2} were correlated. As the sperm senses a gradient of attractant, Ca^{+2} propagates along the flagella, causing it to execute gaits that are off-centered and larger in our shape space. Off-centered strokes, as discussed previously, lead to turning toward the attractant, and thus chemotaxis.

The stroke amplitude shows that gaits are smaller going into a turn and grow as the sea urchin sperm's motion is directed toward the attractant. This corresponds nicely to chemotaxis and moving at a higher speed when the sperm faces the desired direction. Examining the tail beat frequency in Fig. 5-6d gives us a clear indication of the onset of chemotaxis, which may also be verified by measuring Ca^{+2} along the flagella, a measurement not gathered simultaneously with high-speed images of the flagella due to experimental limitations. While chemotaxing, the beat frequency is approximately 30% higher than when non-chemotaxing.

5.4.2 Classifying chemotaxis

Data for chemotaxing and non-chemotaxing sea urchin (*Arbacia punctulata*) sperm was gathered via high speed microscopy by J.S. Guasto [50]. To capture chemotaxing, the egg-derived attractant Resact was introduced into the top of a micro-channel and allowed to diffuse across the channel. The right panel of Fig. 5-7 displays a typical chemotaxing path: the sperm initially swims in a circular trajectory and when a chemical gradient is identified, the sperm moves toward the higher concentration of attractant.[2]

We first separate the flagellar curvature data into two sets: chemotaxing and non-chemotaxing. The primary and secondary spatial basis functions resulting from the kinematic decomposition differ slightly between chemotaxing and non-chemotaxing, as shown by the red and green curves in Fig. 5-7, while the third basis function shows

[2]Turning is partially due to the sperm's proximity to the glass slide during the experiment, as boundaries are known to increase the tendency to turn in low Reynolds number locomotion [38].

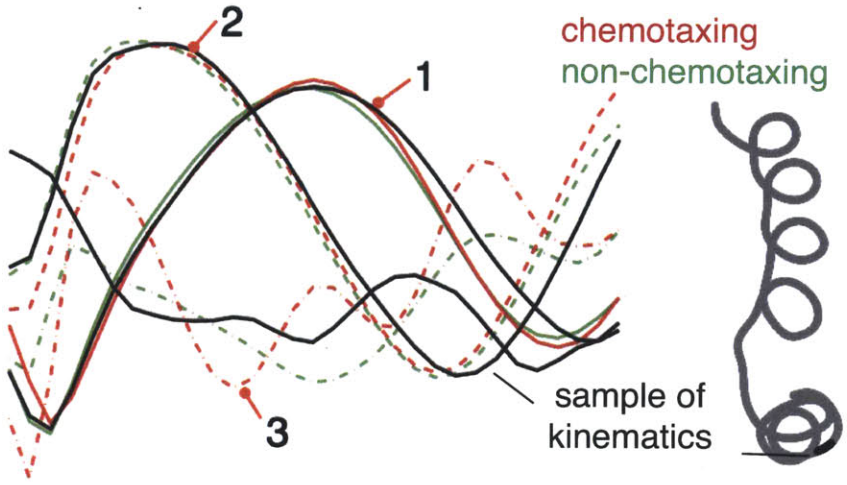

Figure 5-7: The first, second, and third basis functions are calculated from all chemotaxing data (denoted in red), all non-chemotaxing data (denoted in green), and a random sample of three tail beats (denoted in black). By comparing the sample basis functions to the chemotaxing and non-chemotaxing basis functions through metrics $\mathbf{M}_C$ and $\mathbf{M}_N$, we classify the sample as chemotaxing or non-chemotaxing.

remarkably more variation for the chemotaxing case when compared to the non-chemotaxing case. We develop a metric to classify if a sperm is chemotaxing based solely on the kinematics, without any information of the environment. First, we calculate the basis functions for three periods of curvature data, selected randomly along the trajectory, as indicated in Fig. 5-7. We then compare the sample basis functions ($\hat{U}_i$) to the basis functions for chemotaxing ($U_{C,i}$) and the basis functions for non-chemotaxing ($U_{N,i}$). Using metrics based on the inner products of the first three basis functions, we quantify this comparison,

$$\begin{aligned} \mathbf{M}_C &= |\langle U_{C,1}, \hat{U}_1\rangle \cdot \langle U_{C,2}, \hat{U}_2\rangle \cdot \langle U_{C,3}, \hat{U}_3\rangle| \text{ and} \\ \mathbf{M}_N &= |\langle U_{N,1}, \hat{U}_1\rangle \cdot \langle U_{N,2}, \hat{U}_2\rangle \cdot \langle U_{N,3}, \hat{U}_3\rangle|, \end{aligned} \tag{5.6}$$

so that $\mathbf{M}_C$ and $\mathbf{M}_N$ vary from 0 (basis functions are orthogonal) to 1 (basis functions are collinear). For a given set of sample basis functions $\hat{U}_i$, if $\mathbf{M}_C > \mathbf{M}_N$, the sample is classified as chemotaxing and if $\mathbf{M}_C < \mathbf{M}_N$, the sample is classified as non-chemotaxing. We apply these metrics to many random samples, illustrated in

Fig. 5-8a, and find a misclassification rate of just 4.2% for our data, meaning that just 4.2% of the samples were classified as chemotaxing when their true state was non-chemotaxing, or vice versa. Including an optimal spatial linear weight so that the basis function metric is weighted toward the head, we obtain a misclassification rate of just 2.5% (Fig. 5-8b).

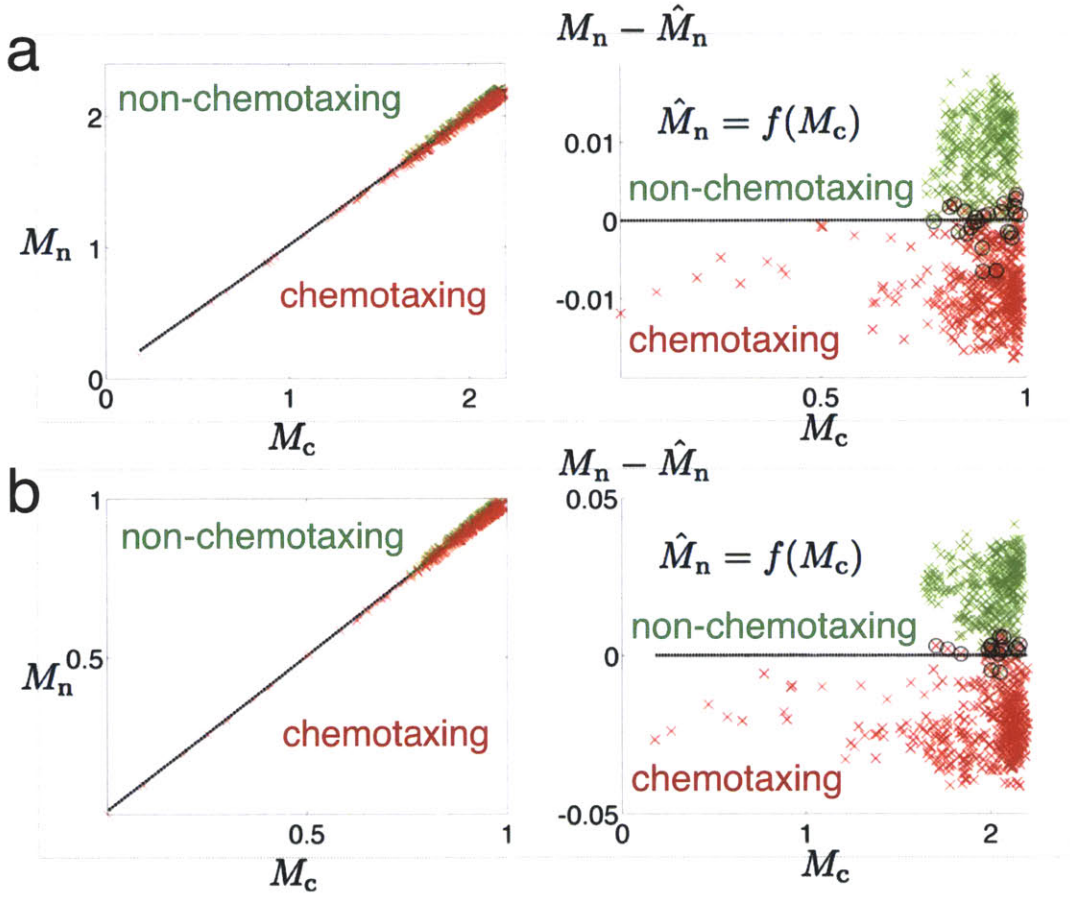

Figure 5-8: a) We compare sample basis function calculated from the flagellar kinematics of just three tail beats to the basis functions found from all chemotaxing (red) and non-chemotaxing (green) data. Using inner product based metrics, $\mathbf{M}_C$ and $\mathbf{M}_N$, we classify the sample as chemotaxing if $\mathbf{M}_C > \mathbf{M}_N$ and non-chemotaxing if $\mathbf{M}_N > \mathbf{M}_C$. With these metrics, our misclassification rate is just 4.2%. b) Including an optimal linear spatial weighting reduces the misclassification rate to just 2.5%.

In this section, we applied the kinematic decomposition to solve two problems. First, we described the sea urchin sperm's motion using basis functions from kinematic decomposition and projected the stroke during a single trajectory onto that basis

function set. Parameterizing and examining the stroke and corresponding curvature functions allowed us to, for the first time, visualize and rationalize the kinematics during chemotaxis and connect flagellar kinematics and the sensory system of the sea urchin sperm. Second, we compared the basis functions for chemotaxing and non-chemotaxing sperm to successfully create a classification metric based solely on the kinematics.

5.5 Three dimensional curves

The methods presented here are generalizable to three dimensional curves, like those formed by sidewinding snakes. When describing a curve in three dimensions, *torsion*, τ, in addition to curvature, κ, must be considered. Torsion describes the twisting component of a curve in three dimensions. These quantities are calculated using the Frenet-Serret equations.

$$\begin{aligned} \frac{d\mathbf{T}}{ds} &= \kappa\mathbf{N} \\ \frac{d\mathbf{N}}{ds} &= -\kappa\mathbf{T} + \tau\mathbf{B} \\ \frac{d\mathbf{B}}{ds} &= +\tau\mathbf{N} \end{aligned} \tag{5.7}$$

where $\mathbf{T}$ is the tangent unit vector, $\mathbf{N}$ is the normal unit vector, and $\mathbf{B}$ is the binormal unit vector, calculated as $\mathbf{B} = \mathbf{T} \times \mathbf{N}$. The addition of torsion may be handled in multiple ways, inspired by those methods used in other fields like turbulence in fluid dynamics. One method is to create two matrices, M_κ and M_τ, one for curvature and another for torsion. Each of these is treated separately in the kinematic decomposition and the three-dimensional curve is reconstructed by combining the basis functions and amplitudes from each. Here we can treat the torsion and curvature separately and independently choose the number of basis functions needed to accurately represent the system. This is advantageous if, for example, most of the torsion can be accounted for by a single basis function while three basis functions are needed to represent curvature.

The second method combines the data into one matrix, $M_{\kappa,\tau}$ by creating one column for each time step, with the curvature vector stacked on top of the torsion vector. The SVD of $M_{\kappa,\tau}$ results in basis functions that must be split before the shape resulting from those basis functions can be calculated. This approach more closely ties together the torsion and curvature, but prevents us from selecting different degrees of freedom for each.

5.6 A powerful kinematic tool

The methods of applying kinematic decomposition via an SVD to a matrix of curvatures for each time step are powerful tools for a range of analyses. From the decomposition, we extract optimal spatial basis functions and their associated strokes in the shape space. The decomposition *separates* the kinematics into spatial and temporal components. Further, reducing the dimension of the kinematics lends itself to easier visualizations of the system and its dynamics, as in Fig. 5-3. With these visualizations, we can calculate optimal strokes (Fig. 5-4), understand the gait modulations that lead to turning (Fig. 5-6), and classify whether or not an individual is chemotaxing (Fig. 5-8). Our kinematic decomposition is robust, leading to meaningful results even with missing data in time or coarse spatial resolution along the body. In the next chapter, we continue to explore the value of these kinematic methods by quickly and effectively comparing the motion of *Arbacia punctulata* to other species. We expand to study the the effect of viscoelasticity on swimming *C. elegans* and gaits of high Reynolds number swimmers (trout and eel).

Chapter 6

Applications of the kinematic decomposition

In this chapter, we demonstrate the utility of the kinematic decomposition developed in Chapter 5. We begin by applying our decomposition methods to compare the kinematics for the sperm of several sea urchin species, namely *Arbacia punctulata*, *Lytechinus variegatus*, *Lycaon pictus*, and *Strongylocentrotus purpuratus*. We then expand our analysis to include the sperm of two very different organisms, *Ciona intestinalis*, a sea squirt and one of the closest invertebrate relatives to vertebrates, and a bull, an internal fertilizer and a vertebrate. We then move to examine *C. elegans*, an organism that swims at a slightly higher Reynolds number than sea urchin sperm in water. Here we gauge the effect of environment on swimming gaits by studying *C. elegans* at a range of viscosities, in water and in a viscoelastic fluid. This study is followed by another of gait change–namely, the trout's gait in uniform flow compared to the gaits that result when swimming (both actively and passively) in a vortex stream. Lastly, we apply our kinematic decomposition tools to find the differences between steady and accelerating gaits in eels and compare these results to previous research. These examples demonstrate that the kinematic decomposition is robust, easy to apply, and leads to effective visualization and a wealth of information about the system. We summarize the characteristics of the organisms studied in this chapter in Table 6.1.

Organism	Length	Speed	*Re*
Arbacia punctulata sperm	46μm	207μm/s	$1.4 \cdot 10^{-2}$
L. variegatus sperm	50μm	250μm/s	$1.8 \cdot 10^{-2}$
L. pictus sperm	50μm	248μm/s	$1.8 \cdot 10^{-2}$
S. purpuratus sperm	50μm	192μm/s	$1.4 \cdot 10^{-2}$
Ciona intestinalis sperm	50μm	315μm/s	$2.2 \cdot 10^{-2}$
Bull sperm	56μm	117μm/s	$9.4 \cdot 10^{-3}$
C. elegans (buffer)	10^{-3}m	$3.5 \cdot 10^{-4}$m/s	$3.4 \cdot 10^{-1}$
C. elegans (viscoelastic)	1mm	$2.5 \cdot 10^{-4}$m/s	$5 \cdot 10^{-4}$
Trout	10cm	0.5m/s	$5 \cdot 10^{4}$
Eel	20cm	1m/s	$2 \cdot 10^{5}$

Table 6.1: Organisms included the kinematic curvature decomposition analysis. Length is the body length of the organism, speed is the translational speed and *Re* is the Reynolds number.

6.1 Interspecies comparison in sperm

Comparing kinematics between species is inherently difficult. In this section, we will exploit the tools developed in Chapter 5 to effectively analyze and compare the kinematics of swimming in water for six types of sperm: *Arbacia punctulata*, *Lytechinus variegatus*, *Lycaon pictus*, *Strongylocentrotus purpuratus* (all sea urchins), *Ciona intestinalis*, and bull. Sperm are unicellular and therefore have extremely simple sensory, control and biomechanical systems. Understanding how such simple organisms work is an important first step to understanding larger, more complex systems. A comparison of the body length, speed and Reynolds numbers for these organisms is summarized in Table 6.1. As illustrated in Fig. 6-1, we investigate whether the kinematics of *Ciona intestinalis* sperm are more representative of the genetically similar bull sperm (and therefore dominated by nature), the environmentally similar sea urchins (and therefore dominated by nurture), or some combination of the two.

For all of these samples (excluding the bull sperm), data was again gathered by J.S. Guasto via high speed microscopy while swimming in water in a micro-channel [48]. The bull sperm video is supplementary material for a paper by Friedrich *et al.* [41]. All videos were digitized using MATLAB and body curvature was calculated and filtered from (x, y) data of the head and flagella.

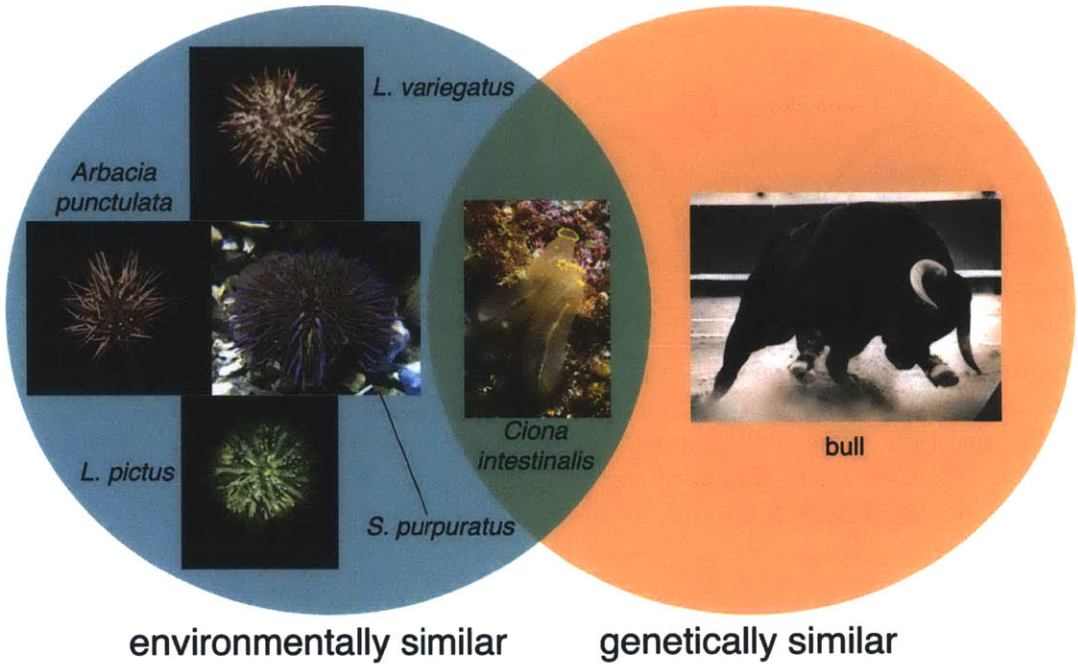

Figure 6-1: *Ciona intestinalis* is an external fertilizer, like the sea urchins pictured on the left, but is genetically more similar to the bull on the right.

The kinematic decomposition was applied to each set of data separately, so that basis functions $U_i[s]$ were found for each species independently. The primary and secondary basis functions are illustrated in Fig. 6-2 and show several intriguing results. First, the basis functions for the sea urchin sperm are remarkably similar, indicating that the flagellar mechanics among sea urchin sperm are extremely consistent and perhaps fundamental to these systems. The bull sperm, the only internal fertilizer of the six organisms, is noticeably distinct from the other basis functions. As an internal fertilizer, bull sperm evolved to use swimming strategies effective in viscous biological fluids, a strikingly distinct environment from open water. Fig. 6-3 shows ν_N, the fraction of variance account for by N basis functions (5.4) for all six organisms. With just two basis functions, the basis functions account for between 50% and 70% of the variance of motion.

Ciona intestinalis offers interesting insight to the connection between sea urchin sperm and bull sperm. *Ciona intestinalis*, a sea squirt, is genetically very similar to

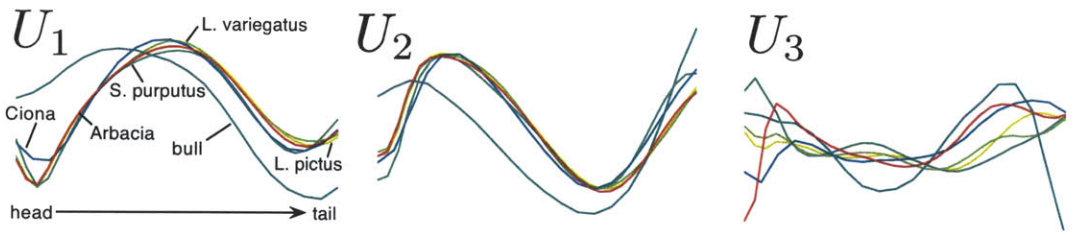

Figure 6-2: The first, second, and third basis functions for the sperm of four sea urchins (*Arbacia punctulata*, *L. pictus*, *L. variegatus* and *S. purputus*), *Ciona intestinalis*, and bull. The first and second basis functions, U_1 and U_2, for all four sea urchins and *Ciona intestinalis*–all external fertilizers–can successfully be represented by a single set of basis functions, as shown in Fig. 6-4a.

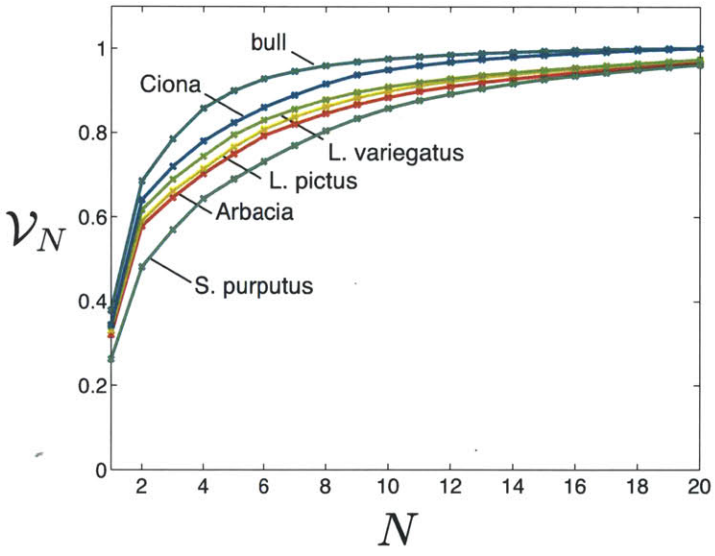

Figure 6-3: The fraction of variability accounted for by N basis functions ($\mathcal{V}_N$) shows that two basis functions covers a majority of the variability for all organisms (*Arbacia punctulata*, *L. pictus*, *L. variegatus* and *S. purputus*, *Ciona intestinalis*, and bull sperm).

vertebrates. Though *Ciona intestinalis* has far fewer genes than vertebrates, those gene families it does have are very closely matched to vertebrate gene families [33]. However, *Ciona intestinalis* externally fertilizes, like the sea urchin sperm. We see from Fig. 6-2 that its basis functions are notably close to (and highly correlated with) the sea urchin basis functions. Therefore, the kinematics of sperm appear to be a result of the *environment* through which it swims, rather than its genetic makeup.

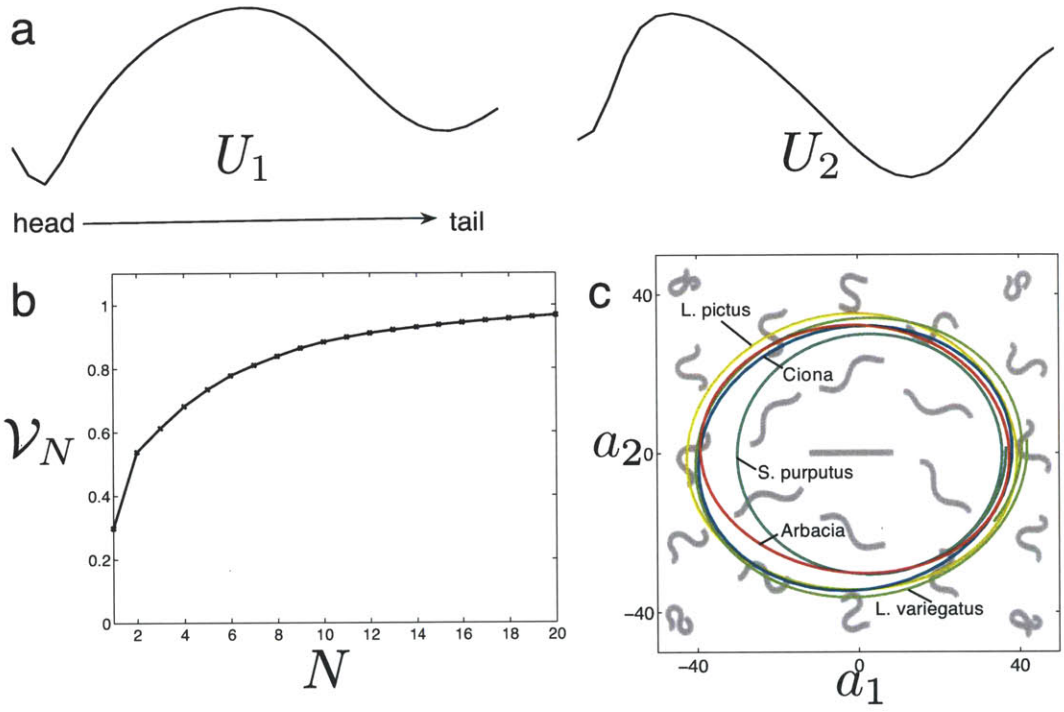

Figure 6-4: a) We find a set of basis functions for multiple organisms by combining the data for all sea urchins (*Arbacia punctulata*, *L. pictus*, *L. variegatus* and *S. purputus*), and *Ciona intestinalis*. b) A majority of the variance of motion for *five different* organisms is accounted for by just two basis functions. c) With a single set of basis functions, we can compare the strokes for all five organisms. All four sea urchin strokes and the stroke for *Ciona* are representative of each other. Most strokes are centered around the peak of the x constraint curvature function in Fig. 6-5 and within the zero contours.

The similarity between all four sea urchin basis functions and the *Ciona intestinalis* basis functions (Fig. 6-2) suggests that by combining the curvature data for these five organisms, a single set of basis functions may represent the motion for all five organisms. Not surprisingly, from Fig. 6-4a, we see that the basis functions that result from

combining the curvature data are similar to those in Fig. 6-2 for *Arbacia punctulata* alone. Thus, we find that the basis functions from the combined data form constraint curvature functions (Fig. 6-5) containing two-fold rotational symmetry and differ only slightly from those in Fig. 5-4 for *Arbacia punctulata*. As such, the optimal efficiency stroke is again compact and centered around the origin of the shape space. With a single set of basis functions, two basis functions account for approximately 55% of the variance (Fig. 6-4b).

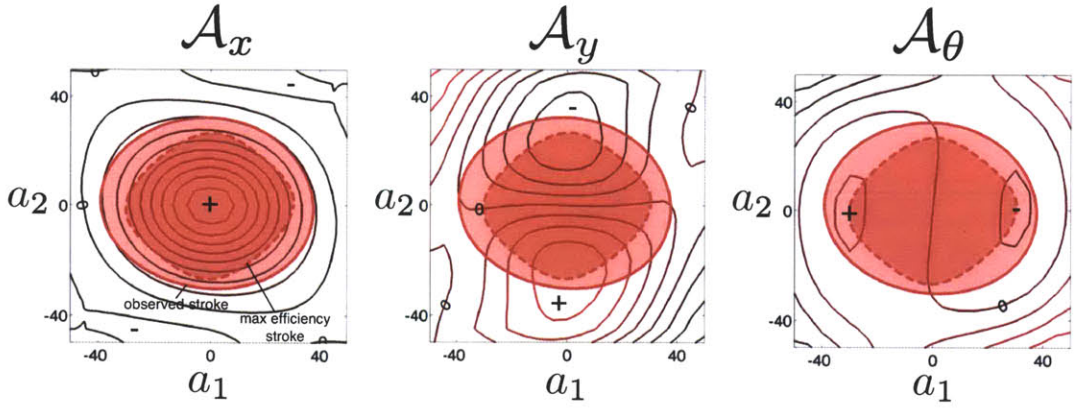

Figure 6-5: Constraint curvature functions for a single set of basis functions, created by combining the curvature data for the sea urchin sperm and *Ciona intestinalis* sperm. Two-fold rotational symmetry is observed in all three graphs, with odd symmetry in the y and θ fields. The observed stroke and maximum efficiency stroke are both centered in the shape space and stay within the zero count ours of the x curvature function, though the maximum efficiency stroke is more compact.

Projecting the motion of each of the five organisms onto this set of basis functions allows us to easily compare strokes. From Fig. 6-4c, we see that the strokes for the four types of sea urchin sperm and *Ciona intestinalis* are comparable in size and shape, though *S. purpuratus* is slightly off-centered from the others.

Lastly, we create constraint curvature functions for the bull sperm from its primary and secondary basis functions. From Fig. 6-6, the two-fold symmetry is again readily apparent in all three subfigures. The maximum efficiency stroke is larger than the observed stroke in this instance, though the data for the bull sperm was more limited in both temporal and spatial resolution when compared to the other data sets, which may account for the discrepancy.

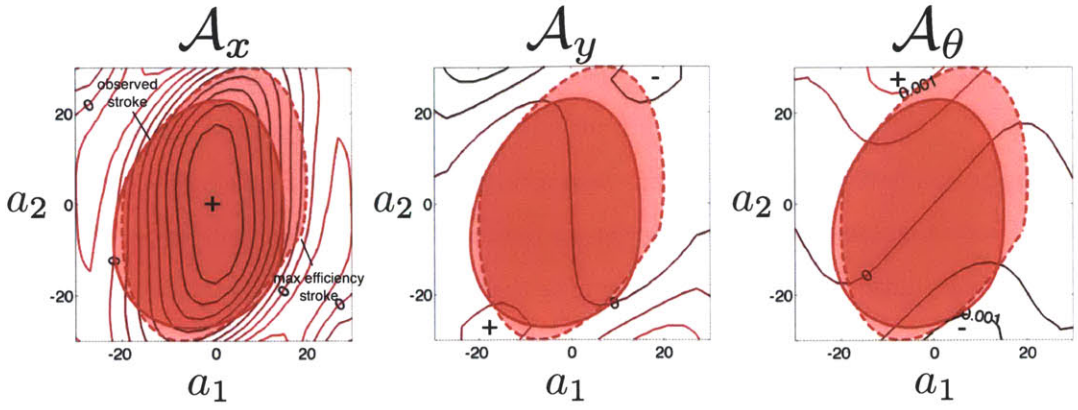

Figure 6-6: Constraint curvature functions for bull sperm also exhibits the two-fold rotational symmetry present in the previous curvature functions. For the bull sperm, the maximum efficiency stroke is larger than the observed stroke.

6.2 The effect of viscoelasticity on *C. elegans*

Caenorhabditis elegans is a nematode approximately 1 mm in length that exhibits highly periodic undulatory swimming behavior. *C. elegans* is a model organism with only 302 neurons and 95 muscle cells lining its dorsal and ventral sides [165]. For locomotion, approximately 200 neurons are involved, about 50 of which are responsible for undulations [26]. Studies on *C. elegans* cover a wide range of topics, including the relationship between the nervous system and kinematics [22, 74, 82, 111, 112], determining the biomechanical properties (Young's modulus and tissue viscosity) of the nematode [140, 141, 142] and the influence of many environmental changes on kinematics, including movement through saturated soil [69, 70], viscoelastic media [9, 136], viscous fluids [82, 136], agar gel [116], wet surfaces [138], and lattice structures [96]. A majority of these studies use wavelength, frequency, wave speed and other parameters as kinematic descriptions of the gait. Krajacic *et al.* [83] developed a method of describing gaits with 18 kinematic and biomechanical features to compare different mutations of *C. elegans*. Padmanabhan *et al.* [116] used piecewise harmonic curvature with six parameters to describe the shape of *C. elegans* and its path as it crawls on agar, with excellent agreement. Stephens *et al.* [139] represented the kinematics of a crawling *C. elegans* with an eigenvalue decomposition of a mean-centered

covariance matrix.

Our kinematic decomposition is distinct from these methods in that our analysis extracts the spatial basis functions from the original, rather than the mean-centered curvature, and we gather significant temporal information from a single decomposition. Taking the mean-centered curvature fails to account for any curvature bias the system may have, such as in the case of a turning *C. elegans* when the body maintains curvature throughout the turn. Further, our analysis requires as few as two parameters to describe the kinematics at each time step and allows straightforward incorporation into our swimming model using resistive force theory.

Here we apply kinematic decomposition methods to address the role of viscosity in kinematics and whether or not the gait in viscoelastic fluid versus a water (buffer) solution are unique. Pierce-Shimomura *et al.* [119] found that the swimming gait and crawling gaits for *C. elegans* were fundamentally distinct and described the gaits as "C-shaped" and "S-shaped," respectively, suggesting that the choice of gait was determined by the animal's sensory response to the environment. The motions were compared through an examination of the amplitude and frequency of curvature at different points along the body.

Conversely, Berri *et al.* [9] found that *C. elegans* uses a single gait and performs a continuous modulation according to the environmental properties. Their analysis was based on measures of beat frequency, and the wavelength and amplitude of curvature. Similarly, Shen *et al.* [136] compared kinematics in viscoelastic media and a buffer solution and discovered that elasticity leads to slower propulsion due to the enhanced resistance to fluid flow. Also, the beat frequency and wave speed of the traveling wave along the body decrease with increasing viscoelastic effects, suggesting that viscoelasticity affects the speed of motion rather than the swimming kinematics (the shape of the stroke).

The kinematic decomposition allows us to visualize whether or not distinct gaits are observed in different environments. If the gaits are the same, the basis functions resulting from each environment and the corresponding strokes in the shape space will be similar, as we observed with the sea urchin sperm and *Ciona intestinalis* in

Fig. 6-4. Rather than being forced to select a few points along the body to track in time or summarizing the kinematics with limited parameters like amplitude and wavelength, we are able to completely visualize the kinematics during locomotion.

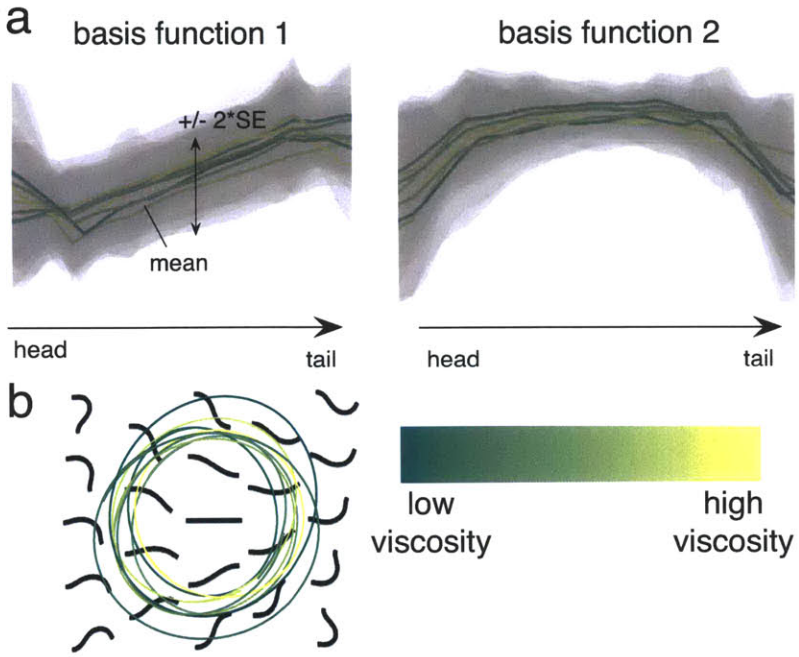

Figure 6-7: a) The basis functions for all viscosity levels are overlaid, with the mean (over all of the individuals at that viscosity level) shown by a solid colored line, and two standard errors above and below the mean denoted by the gray shaded regions. There is excellent consistency over both basis functions, signifying that the fundamental kinematics for *C. elegans* is the same for swimming in a range of viscosities. The data ranges from low viscosity (30ppm in blue) to high viscosity (3000ppm in yellow). b) The strokes for the eight levels of viscosity are projected onto a single set of basis functions for comparison. While the lowest viscosity strokes (30ppm and 100ppm) are slightly larger than the higher viscosity strokes, no distinct stroke pattern emerges as a function of viscosity level. The shape space for these basis functions is shown in the background.

We begin our analysis with curvature data provided by Shen and Arratia [137]: eight sets of data for *C. elegans* in different viscosities (30ppm, 100ppm, 300ppm, 500ppm, 1000ppm, 1500ppm, 2000ppm, and 3000ppm of carboxymethyl cellulose where salt ions in the buffer solution eliminate viscoelastic effects) and two sets of data to examine viscoelasticity, one for *C. elegans* swimming in water and one for *C.*

elegans swimming in a viscoelastic fluid (3000 ppm of carboxymethyl cellulose). For each environmental condition, data for 10-25 individuals is included. Data collection details can be found in [136].

Examining the spatial basis functions in Fig. 6-7a for swimming at eight distinct viscosities reveals that the fundamental kinematics across all viscosity levels are consistent. For both the first and second basis functions, the mean basis functions (over all individuals at that viscosity levels, denoted by a solid line) are similar and the gray shaded regions, which represent two standard errors above and below the mean basis functions, almost overlap entirely. The motion at each viscosity level is projected onto a single set of basis functions and these strokes are shown in Fig. 6-7b, over the shape space of body shapes achievable by the single set of basis functions. While the lowest viscosity strokes (30ppm and 100ppm) are slightly larger than higher viscosity strokes, there is no clear pattern that suggests distinct gaits are executed based on viscosity level. The larger strokes correspond to executing more highly curved shapes while swimming, as reflected in the shape space shown in the background of Fig. 6-7b.

Performing a kinematic decomposition on the water (buffer) versus viscoelastic data sets results in the basis functions in Fig. 6-8. Most noticeably, the basis functions for motion in the buffer solution are much more consistent across the ten individuals than the basis functions found for swimming in a viscoelastic media. However, the means of each basis function set (denoted by the black lines in Fig. 6-8) are similar, though the primary basis function for motion in buffer solution corresponds to the secondary basis function in viscoelastic media and vice versa. This swapping of basis functions is not physically significant, as the variance plots in Fig. 6-9a reveals that the first two functions of both basis functions sets account for approximately the same amount of variance ($\sim$35%), so that the basis functions are interchangeable. The shaded regions of Fig. 6-8 show two standard errors above and below the mean. The second row of Fig. 6-9 shows that the stroke amplitudes in the shape space are comparable for each, though the strokes in the viscoelastic solution are noisier. Our findings here are in agreement with Berri *et al.* and Shen *et al.*, who indicated that changing the environmental properties does not result in a distinct gait change, as

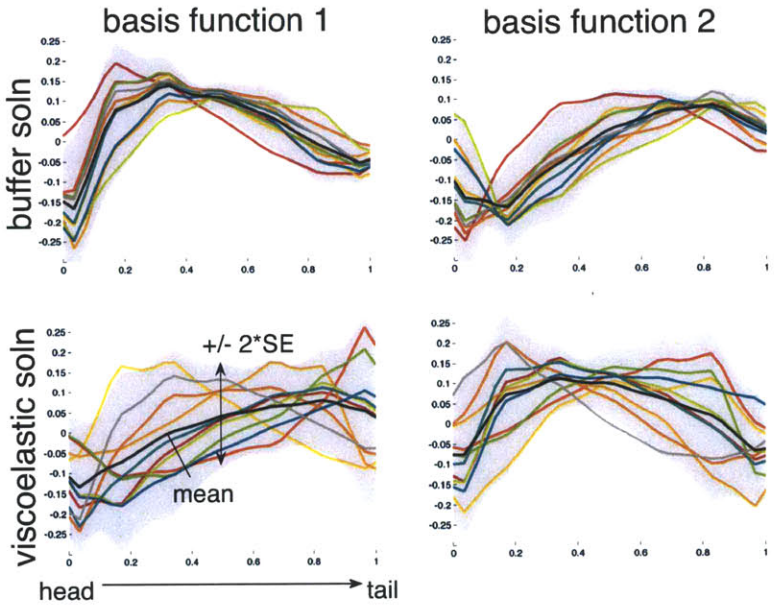

Figure 6-8: The top row shows the first and second basis functions for *C. elegans* swimming in a buffer solution (water). The solid black line is the mean of the basis functions for the ten individuals and the shaded gray regions are two standard errors above and below the mean. Comparing these basis functions to those found for swimming in a viscoelastic media (bottom row) shows that the motion in the buffer solution is much more consistent, but the mean basis functions in each environment are similar, when comparing the primary basis function of one system to the secondary basis function of another.

previously suggested in [119]. Instead, moving from a buffer solution to a viscoelastic media affects the beat frequency. For our data, the time for one beat is 23% longer in viscoelastic media. The similar basis functions resulting from both cases also agrees with previous studies where the authors found no significant change in wavelength [9, 136].

Our approach greatly simplifies the analysis. Rather than considering many parameters, we are able to separate the spatial and temporal components of kinematics and optimally represent the motion in a low-dimensional manner. We determined that the fundamental swimming kinematics of *C. elegans* is the same across many levels of viscosity. Additionally, we found that viscoelasticity is responsible for more variation in gaits from individual to individual. This suggests that while *C. elegans* may use a single control mechanism and gait for motion in any environment, viscoelasticity introduces larger perturbations to that base gait. Our conclusion is in agreement with results reported by Berri *et al.* [9] that outside forces play a small role in locomotion.

The more meaningful result of this study lies in the basic process we have introduced to model *C. elegans* locomotion and its potential impact. Recent advancements enable real-time targeting of single motor neurons via laser to manipulate *C. elegans* behavior (i.e., to move forward or backwards) [86] and interneurons to elucidate chemotaxing and the neural circuit function [52, 80]. These studies enable identification of the coupling behavior of excitatory and inhibitory motor neurons that give rise to locomotion. Incorporating our kinematic decomposition into these systems would enhance the understanding and control of the *C. elegans* neural system and motor circuit. Together, this research is an important breakthrough in neurobiology that will lead to improved understanding of more complex systems, like humans.

6.3 The Kármán gait in rainbow trout

Fish are subjected to complex three-dimensional flows in nature. The relationship between perturbations to the free stream and a fish's behavior has been studied

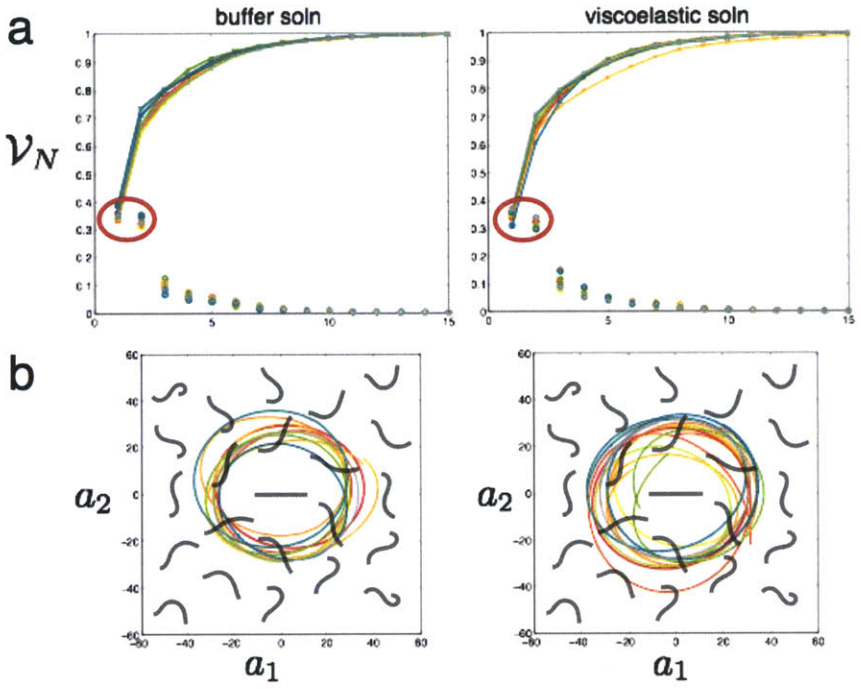

Figure 6-9: a) The fraction of variance accounted for by each basis function shows that the first two basis functions encompass approximately the same energy in both water and viscoelastic media. b) Comparing the strokes in both environments reveals that while they are approximately the same amplitude, the strokes through viscoelastic media are more irregular.

for many fluid processes, including the influence of turbulence [117, 163], fish in schools (which exploit regions of reduced flows and vortex capture) [40, 163, 164], and perturbations due to an obstacle in the flow [16, 64, 159]. These studies consider the physiological costs, along with the kinematic and sensory responses of the fish when subjected to altered flows [89].

One commonly studied flow perturbation is flow around a cylinder. If the Reynolds number is between 300 and 150,000, the flow behind the cylinder is unsteady and generates a Kármán vortex street, or regularly shed and alternating vortices. Rainbow trout have been observed to synchronize their body motion to the vortex shedding frequency [90]. This motion, termed the "Kármán gait," is recognized by larger body amplitudes in the lateral direction and lower beat frequencies when compared to motion in free stream flow of comparable velocity. Liao *et al.* [87, 88] showed that steady swimming kinematics and the Kármán gait are distinct. During the Kármán gait, a trout weaves between vortices and the lateral (mostly passive) displacement is dependent on the lateral component of flow resulting from the previous vortex [90].

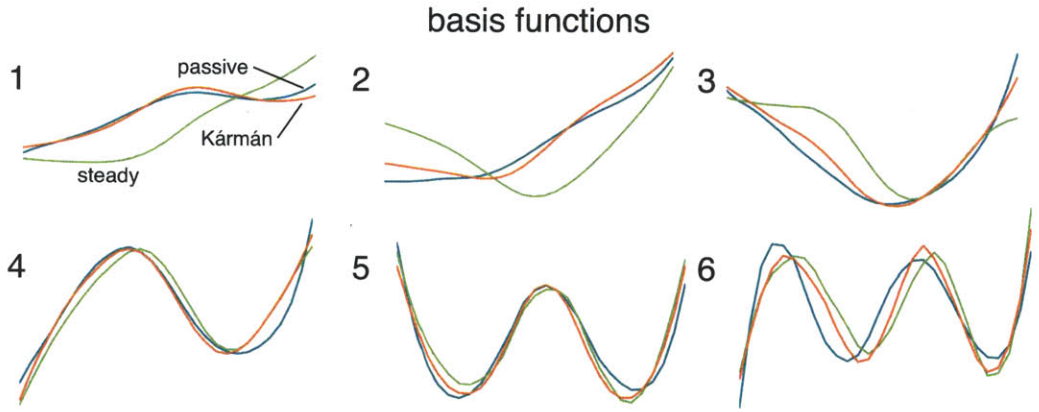

Figure 6-10: The first three basis functions for three gaits in trout (steady, Kármán, and passive in a vortex street) reveal the similarities between Kármán and passive gaits. The following three basis functions show excellent agreement between all three motions and exhibit higher spatial frequencies than observed in the first three basis functions.

From videos, we extract midline data of trout in three states: actively swimming in steady flow, actively swimming in a Kármán vortex street, and passively swimming

(dead) in a vortex street [87]. We apply our kinematic decomposition methods to distinguish the difference in gaits and conjecture as to whether or not the Kármán gait is primarily passive. Fig. 6-10 illustrates the first six basis functions for each of the three gaits (steady, Kármán, and passive). Basis functions 1-3 (from the figure) indicate that the Kármán and passive basis functions are highly correlated, while the steady basis functions are approximately the same wavelength but differ in shape. Basis functions 4-6 show an excellent match between all three sets of basis functions, and show increasing spatial frequencies (shorter wavelengths). The variance captured by these first six basis functions is over 98%, as illustrated in Fig. 6-11a. The first two basis functions are responsible for over 70% of the variance. Fig. 6-11b shows the correlation (a measure of the similarity between two basis functions) for each pair of basis functions and confirms that the Kármán and passive states are highly correlated for the first several basis functions. The two active motions, steady and Kármán, have the highest correlation for basis functions 4-7. The consistency of the higher basis functions suggests that the motion related to these basis functions is inherent to the structure of the trout, as they are present in the dead trout that responds only passively to the flow. Examining the time dynamics of the steady stroke reveals lower beat frequencies for the Kármán and passive gaits when compared to the steady gait, as previously reported by Liao [87].

Because the Kármán and passive gaits share basis functions, we can examine their strokes in a single shape space. Fig. 6-11c illustrates that the amplitude of the passive stroke is larger than the Kármán stroke for all basis functions. Higher amplitudes result in more highly curved shapes executed throughout the passive gait. These results suggest that the muscles activated while in a Kármán vortex street act to stiffen the body and reduce the lateral motion that would be present for the dead fish in a vortex street.

Liao [87] directly measured the muscle activity through electromyography by surgically implanting electrodes into six muscles. He observed that there was substantially less muscle activity during the Kármán gait than the steady gait and conjectured that this muscle activity was primarily for stability and control. While directly measur-

ing the muscle activity and flow field provide a more detailed view, our approach leads to similar results—that is, that the Kármán gait is more similar to the passive gait but with more constrained motions, likely for stability and control—and is an excellent initial step to investigate this system. In general, the results from the kinematic decomposition may guide the next steps of research so that invasive or costly measurements are performed only when necessary.

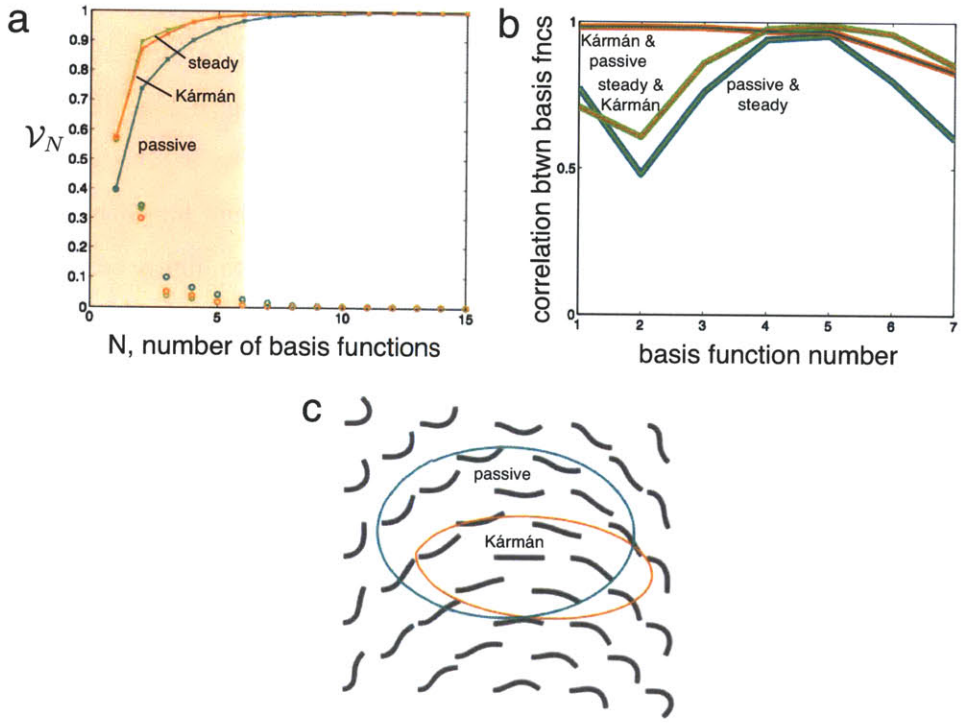

Figure 6-11: a) The first two basis function account for over 70% of the motion and the six basis function in Fig. 6-10 encompass at least 98% of the motion. b) The correlation between basis functions measure how similar any two basis functions are to each other. The Kármán and passive gaits are highly correlated for the first several basis functions, indicating similarities in those gaits, though the steady and Kármán gaits (the two "active" gaits) outperform other combinations for basis functions 4, 5, and 6. c) The basis function amplitudes for the passive gait are larger than the Kármán gait amplitudes, revealing that the shape changes in the passive are more highly curved than in the Kármán gait.

While the details of how the trout interacts with the vortices requires a simultaneous study of flow visualization and the kinematics, we are able to quickly understand

and compare three different gaits using our kinematic decomposition. The basis functions (Fig. 6-10) and their pairwise correlation (Fig. 6-11b) give an informative static comparison to the motions observed for each gait, without requiring a synchronization of video or flow data. In the next section, we examine another high Reynolds number swimming animal, the eel, to compare accelerating and steady motions.

6.4 Steady versus accelerating gaits in eels

While eels undulate a larger portion of their body than other fishes, they maintain only small lateral motions in their head [151]. These kinematics are poorly described by predetermined functions like sines and cosines in the curvature space and therefore are an excellent candidate for kinematic decomposition. In this section we separate the effects of acceleration from the steady motion to classify when an eel (*Anguilla rostrata*) is accelerating.

Previously, Tytell [149] examined both the kinematics and the hydrodynamics, or the wakes produced by accelerating and steady-moving eels, to determine the consequences of accelerating. He found that during acceleration, eels primarily change their tail-tip velocity. In steady swimming, the Strouhal number remains fairly constant ($St = 0.32$) and the body wave speed is the best kinematic predictor of velocity. The Strouhal number is the ratio of tail velocity to swimming velocity, $St = fA/u$, where f is the tail beat frequency, A is the tail amplitude, and u is the swimming speed. Tytell noted that changes in the axial fluid momentum in the wake were indicative of gait changes between steady and accelerating strokes. Further, lateral jets in the wake have more axial momentum during acceleration. An increase in momentum is expected for an accelerating eel because the overall momentum must change, unlike the steady swimming case, where the fish's momentum remains constant [149, 151].

The primary kinematic parameters used in the analysis in [149] were tail amplitude, head amplitude, average tail velocity, body wave speed, and body wavelength. Tail beat frequency, body wavelength, and body wave speed increased significantly with increasing wave speed for steady swimming. During acceleration, an increase

in body amplitude was observed, most noticeably at the head. Deviation of the tail velocity from steady swimming was the best predictor of acceleration.

Tytell determined that the kinematic parameters most indicative of swimming speed and acceleration were body wave speed and tail-tip velocity. Eels vary wave speed during steady swimming to maintain a constant Strouhal number (presumably for efficiency), while during acceleration, they vary their tail tip velocity to increase or decrease thrust [149, 150]. For more details of the experimental materials and methods, see [149].

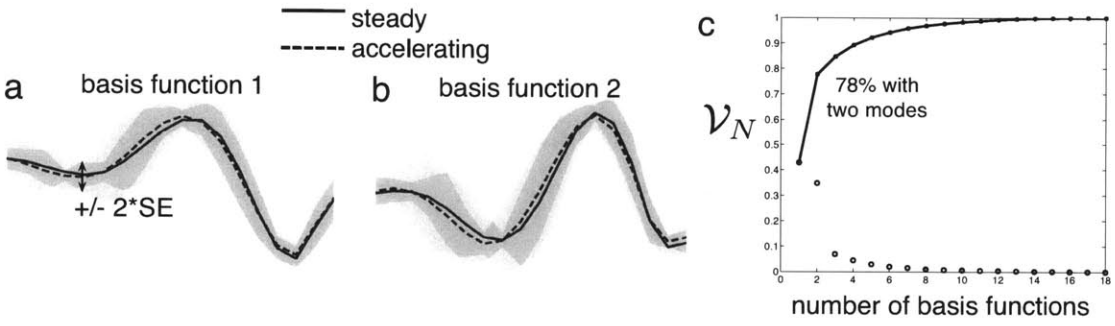

Figure 6-12: The mean a) primary and b) secondary basis functions found for steady (solid line) and accelerating (dashed line) strokes for six eels are highly correlated. The gray shaded regions show two standard errors above and below the mean and almost completely overlap for the two sets of basis functions. c) Aggregating all of the data to get a single set of basis functions, we achieve approximately 78% of the variance with just two basis functions.

In this section, we perform our kinematic decomposition on the data of swimming eels in [149] to verify our method as a way to examine kinematic changes and explore the distinction between steady and accelerating gaits. Fig. 6-12a and b illustrate the primary and secondary basis functions for the body curvature during all steady motions (solid line) and accelerating motions (dashed line) for six eels. The shaded regions around the basis functions are two standard errors above and below the mean basis functions. These regions almost entirely overlap, indicating that the basis functions for the two gaits are similar. We combine the steady and accelerating curvature data results in a single set of basis functions, which describe approximately 78% of the variance with just the primary and secondary basis functions (Fig. 6-12c). Of the

animals studied in this thesis, this is highest variation accounted for with only two basis functions.

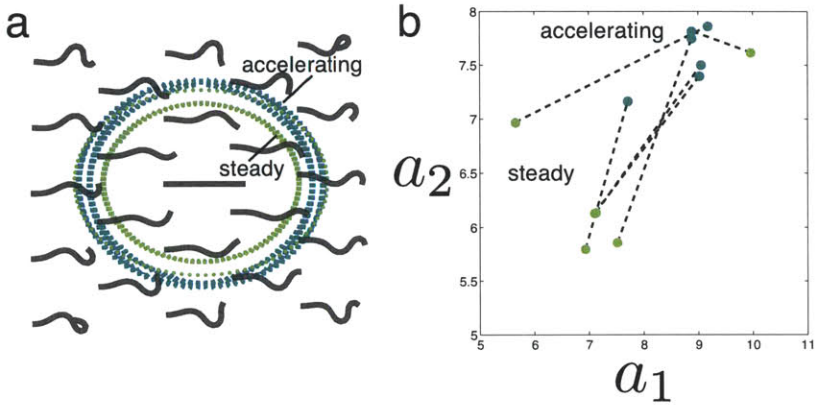

Figure 6-13: a) In all cases, the amplitude of the second basis function, or the height of the stroke in the shape space, is greater when accelerating. b) Examining the characteristic amplitudes of the strokes in the shape space reveals that accelerating gaits are larger than steady strokes for an individual eel for five of the six eels. A larger stroke in the shape space corresponds to a shape with higher curvature, and higher tail amplitude, as previously reported by Tytell [149].

Using a single set of basis functions allows us to create a single shape space of body shapes (Fig. 6-13a) and to overlay the strokes onto this shape space for the steady and accelerating gaits. Fig. 6-13 reveals that the strokes for steady motion are in general smaller in amplitude than their accelerating counterparts. For the eel, larger amplitude strokes correspond to higher curved shapes, as shown in the shape space. The conclusions drawn in the previous study [149] are in agreement with the results from the kinematic decomposition. The larger strokes in the shape space for accelerating motions have higher amplitude motions and give rise to larger deviation in tail velocity, as the tail must move further per stroke. Examining the tail tip velocity and the head motion can be considered more generally here as the speed at which the eel moves through the shape space, or $\dot{a_1}$ and $\dot{a_2}$ and the stroke size. Though we do not have a reconstruction equation for this system, we know that velocity is directly scales with the shape velocity, as discussed in Chapter 2 in Eq. (2.8). In the case where both drag and inertia are important, we expect this general

relationship to hold.

Applying the kinematic decomposition allowed us to verify our methods using known results and uncover new distinctions and phenomena in other systems. By studying the kinematic decompositions for four sea urchin species, *Ciona intestinalis*, and bull, we concluded that the *environment* is most indicative of similar kinematics rather than genetics. While *Ciona intestinalis* and bulls are genetically more similar (than *Ciona intestinalis* is to any of the sea urchins), the kinematics of *Ciona intestinalis* and the sea urchins are indistinguishable. For *C. elegans*, we used the kinematic decomposition to demonstrate that the gaits in a buffer solution (water), at several viscosity levels and a viscoelastic media are actually the same, and the beat frequency is responsible for the change in speed. The viscoelasticity also led to more variability from individual to individual. In trout, we found that the Kármán basis functions match the passive basis functions in a vortex stream, though the stroke is much smaller, signifying that the muscles engaged in trout during the Kármán gait minimize the curvature along the body, likely to stabilize the fish. Lastly, we showed that to accelerate, eels execute higher amplitude, more curved motions, but employ the same basis functions used for steady swimming.

Chapter 7

Conclusion

The work presented in this thesis advances the current standard for visualizing and understanding locomoting systems, for the benefit of both robotic systems (through improved motion planning and modeling) and biological systems (by creating an effective method of analyzing and comparing systems). We developed methods of examining the dynamics and kinematics of a swimming system and applied these results to both idealized systems and to organisms with Reynolds numbers that span seven orders of magnitudes and vary greatly in terms of environment, genetics and complexity.

7.1 Visualization of low Reynolds number swimming dynamics

In Chapter 2, we developed a geometric mechanics-based visualization framework using the three-link swimmer at low Reynolds number. In this framework, we took advantage of the kinematic nature of motion at low Reynolds number (that the external velocity can be exactly described by the system's shape changes) and resistive force theory to express the equations of motion in the form of a kinematic *reconstruction equation.* The reconstruction equation (2.8) contains the *local connection* matrix, a Jacobian-like matrix that contains all of the system dynamics, from which

we produce three *constraint curvature function* plots (Fig. 3-2) that allow us to completely visualize all of the dynamics inherent to the system. The volume enclosed by any stroke on the curvature functions is an approximation of the net displacement in x, y, and θ (the rotational direction) a result that employs Stokes' theorem. With this result, we can estimate the net displacement of any stroke in the shape space and identify globally optimal strokes, in terms of maximum displacement per stroke and maximum efficiency per stroke (Fig. 2-5). Using minimum perturbation coordinates ensures that the net displacement approximations are close to the actual net displacement (Fig. 2-4). Further, we examined the effect of interaction between the links on the three-link swimmer using slender body theory. We found that only for large joint angles (when the links become close), do slender body theory and resistive force theory differ significantly.

With the visualization tools developed in Chapter 2, we explore a neutrally buoyant two-link swimmer with offset centers of mass and buoyancy in Chapter 3 (Fig. 3-1). The tendency to rotate toward its stable equilibrium introduces an unactuated degree of freedom for the two-link swimmer, which we manage by including a *buoyant function* term to the reconstruction equation (3.2). As before, we identify the optimal strokes (Fig. 3-4), now in terms of the single joint angle and the dimensionless parameter γ that describes the ratio of time scales for reorienting and flapping.

In Chapter 4, we broaden the scope of our visualization framework by studying a swimmer whose shape is described by sines and cosines in the curvature space, the serpenoid swimmer (Fig. 4-2). The shape space for the serpenoid swimmer reveals 'snake-like' shapes and demonstrates the ability to describe highly curved and continuous shapes with only two parameters. We calculate the constraint curvature functions and optimal strokes in x, y, and θ (Fig. 4-3), noting that the odd two-fold rotational symmetry in the y and θ plots leads to figure eight shaped optimal strokes.

7.2 Kinematic decomposition

In Part II, we focused on developing and demonstrating the utility of the *kinematic decomposition*. The kinematic decomposition is a straightforward and robust method that separates the time and spatial dynamics of a locomoting system, enabling straightforward comparison between different systems or a single system under varying conditions. This method offers an alternative to current standards like choosing several parameters to represent the kinematics or fitting the body shape in time to predefined functions.

In Chapter 5, we described how to perform a kinematic decomposition, beginning with creating a curvature matrix from tracked midline data of a system. An SVD of the curvature matrix yields three matrices that describe the spatial and temporal characteristics of the locomoting system. One matrix, denoted as U, encompasses an orthogonal set of basis functions that define the set of shapes achievable by that system, which we visualize using a shape space as in Figure 5-2b. A second matrix, Σ, indicates the amount of variance accounted for by each basis function. For all systems studied, just two basis functions described over 50% of the variance. Combining two of the matrices (ΣV^*) results in the strokes and time dynamics of the system. Plotting these strokes onto the shape space allows a clear comparison between systems or conditions within a system. Basis functions, strokes, and the associated variability are calculated for *Arbacia puntulata* (sea urchin) sperm (Fig. 5-3). With the reconstruction equation from Part I and the first two basis functions, we found the constraint curvature functions and optimal gaits for the sea urchin sperm in Fig. 5-4.

The second part of Chapter 5 is dedicated to exploring chemotaxis in sea urchin sperm, using the kinematic decomposition. First, we combined results from the kinematic decomposition and constraint curvature functions to demonstrate the connection between flagellar mechanics, strokes, and turning. We then developed a metric to predict whether or not an individual was chemotaxing, based solely on a sample of the kinematics with a misclassification rate of just 2.5% (Fig. 5-8b).

We continued analysis using the kinematic decomposition in Chapter 6, starting

with a comparison between the flagellar kinematics of four types of sea urchin, *Ciona intestinalis* (a sea squirt), and a bull. Though the bull and *Ciona intestinalis* are genetically more similar than *Ciona intestinalis* is to any of the sea urchins, we found that the basis functions and strokes for *Ciona intestinalis* sperm were indistinguishable from the sea urchins. We concluded that these organisms likely have evolved to execute similar swimming strategies because they locomote in the same environment.

Kinematic decompositions of *C. elegans* data confirmed previously published results that motion in different environments are not distinct gaits (as reported by [119]), but rather modulations of the same gait. Analyzing motion of trout gaits in free stream and in a Kármán vortex street revealed that the gait observed in a Kármán vortex street is primarily passive, and that the muscles used in this gait minimize the lateral displacement that would occur otherwise. Lastly, we identified the gait modulation in eels to move from steady swimming to accelerating. More generally, we found greater variation between individuals of the same species for more complex organisms, i.e., the variation was smallest in the single-celled sperm and largest in the eels. As the animal's control system increases in complexity, we expect that finding a globally optimal locomotion solution in this high dimensional space to be increasingly difficult. Instead, it is likely that these organisms have robust control systems and find near optimal motions that are sufficient. The varied motions we observe may well fall into this class of near optimal strokes and thus explain the variation.

The kinematic decomposition best practices are described in Appendix A. In Fig. 7-1, we outline the possible conclusions from the results of performing kinematic decomposition for comparison. First, find and compare the basis functions for each system. If they are not similar, then the systems are fundamentally different. Plotting the shape spaces, strokes, and constraint curvature functions (if possible) will provide static visualizations of the individual system dynamics and kinematics. If the basis functions are similar, compare the strokes. If the strokes are also similar, then the gaits for the two systems are the same. If the strokes are dissimilar, then the systems share a basic biomechanical structure or control system, but the gaits are different.

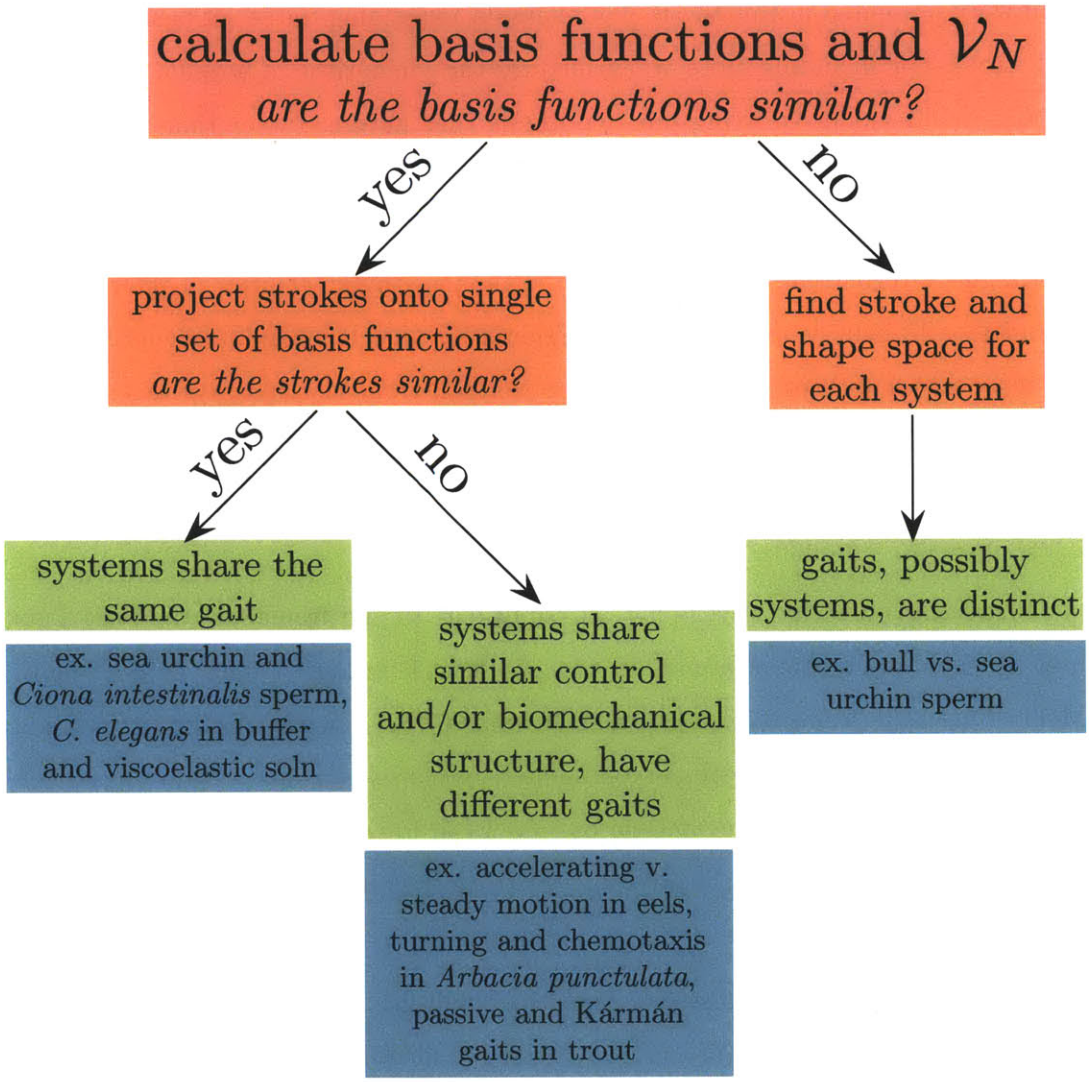

Figure 7-1: Performing the kinematic decomposition on multiple systems allows one to compare the basis functions and strokes, leading to one of three possible conclusions.

7.3 Future work

The development of visualization and kinematic decomposition tools leads to the possibility of answering some intriguing research questions, many of which build directly from work presented in this thesis. For example, expanding the set of basis functions and strokes (by including more organisms) for the comparison of flagellar kinematics in §6.1 would aid in verifying our hypothesis that nature, rather than nurture, is dominant in determining kinematics. If a more accurate physical model is required, including the drag effects due to the sperm's head and interaction between the links is straightforward [143]. For *C. elegans*, examining the kinematics of intermediate viscosities will help us explain the gait modulation that is apparent when observing the more extreme cases studied here. The work on trout and eels may be expanded to predict swimming speed and acceleration based on the kinematics alone. Further, combining this analysis with a high Reynolds number model would nicely connect the kinematics and dynamics of the systems.

A starting point for developing an equivalent to the framework in Part I for high Reynolds number swimmers in the potential flow limit begins with work by Melli *et al.* [101], Kanso *et al.* [73] and Shammas [132]. Though all of our systems were accurately described with two parameters, some systems may require higher dimension descriptions. Our geometric framework in Part I is generalizable to higher dimensions, though we lose the ability to visualize the results as we do in two dimensions.

More generally, applying these tools to other biological systems provides a straightforward method of comparison and may be used to identify the effects of environment (particularly in complex environments like granular media [34, 72, 97] or wet soil [69, 70]), secondary evolution (such as a snake that crawls and swims, or a fish that swims and flies), or a number of biological processes. With increasingly sophisticated measurement techniques, we now have more and more data on neural activity. The kinematic decomposition can aid in linking the sensory systems with locomotion, similar to our study on chemotaxis in sperm. Further, these tools lend themselves to

reconcile the differences between man-made systems and biological systems, leading to effective control and design of new soft robotic components and identification of biological characteristics that may be incorporated into robotic design. Motion planning and gait optimization are commonly time consuming and at best locally optimal. Kinematic decomposition offers the possibility of quick, globally optimal solutions.

The kinematic decomposition can be extended to three-dimensional motions like sidewinding, as described in Chapter 4, and for surfaces like fins and rays, similar to the study by Bozkurttas *et al.* [15]. Incorporating the identification of dominant temporal frequencies may be achieved through combining the kinematic decomposition with a method like dynamic mode decomposition (DMD) as described by Rowley *et al.*, [84, 126, 130]. Though the examples studied in this thesis did not require DMD, broadening the scope of our analysis to other applications and types of biolocomotion (including terrestrial, digging, or aerial locomotion) may benefit from this method.

Once kinematic decomposition is applied to a number of diverse systems, clusters by similar basis functions and strokes may be formed, elucidating similarities between organisms that have possibly remained unobserved. We also expect for heuristic classifications, like those for types of swimming (i.e., anguilliform, carangiform, subcarangiform, thunniform, etc.) to emerge from similar analysis.

Appendix A

Kinematic decomposition best practices

The applications presented in this thesis (turning and chemotaxis in sea urchin sperm, the effect of environment on *C. elegans*, the study of accelerating versus steady gait in eels, and trout kinematics in free stream versus in a vortex street) follow the same general procedures. These procedures can be modeled as a general means to approach many problems and are outlined here.

- **Gather data.** Midline data (that is, (x,y) points along a body) was used for the examples in Chapters 5 and 6, but any measurable quantity that remains at a fixed location on the body is appropriate. This data may be measured directly or gathered from digitized images.

- **Clean, filter and transform data.** Find and remove any erroneous data and filter if necessary. Decide how to manage missing data. Omitting occasional time steps should not affect the results, assuming several periods of motion are included and that the data omitted is not a significant portion of the data set. Normalize all data by body length.

- **Calculate curvature.** Calculate the curvature along the body at each time step. Discretized derivatives can introduce noisy signals and some filtering may

be required. Whenever filtering, avoid over smoothing and erasing meaningful features present in the data. In this thesis, we used one-dimensional Gaussian filters in MATLAB.

- **Populate the M matrix.** Using the curvature at S points along the body at each of T time steps as columns, create the $M_{S,T}$ matrix.

- **Take the SVD.** Performing the singular value decomposition on M will give three matrices: U, Σ and V. Scientific computing software will have a built in function for this, e.g., `svd(M)` in MATLAB. `svds(M)` returns only the vectors associated with the first six singular values and is considerably faster if M is large.

- **Examine the first few columns of U.** The first columns of U are the primary spatial basis functions for the system. If comparing multiple sets of data (either multiple individuals, gaits, or organisms), compare the basis functions of each to identify possible similarities.

- **Examine Σ.** For each set of data, calculate the fraction of variance accounted for by N basis functions, $\mathcal{V}_N$ (Eq. 5.4) from the singular values σ_i in Σ. If $\mathcal{V}_N$ is above a predetermined threshold set by the project's end goal (e.g. 50%, 95%), then N basis functions are appropriate to use for the project. Note that using `svds(M)` to perform the SVD prevents the ability to calculate $\mathcal{V}_N$, as only the first six singular values are found. Instead, the singular values can be compared to each other to gauge their relative importance.

- **Examine ΣV^*.** Study the amplitude of the basis functions to understand the time dynamics of the system's motion. If comparing multiple systems with similar basis functions, project the motion of each system onto a single set of basis functions by employing Eq. (5.5).

- **Perform the analysis.** Fig. 7-1 illustrates some of the possible conclusions one can draw from kinematic decomposition results. If the basis functions are different, the systems are fundamentally different. If the basis functions and strokes

are similar (similarity can be quantified with correlation), then the gaits for the two systems are the same. If the basis functions are similar but the strokes are different, then the systems share a fundamental biomechanical structure or control system, but the gaits are different.

- **Limitations and combining data.** If the curvature matrix is very large, taking the SVD is computationally expensive. A simple solution to this problem is to randomly sample curvatures to create a smaller matrix. The kinematic decomposition is robust and does not require that the curvatures be in sequential order. Taking a representative sample will yield basis functions that are highly correlated to the true basis functions.

  A large curvature matrix may result from either recording data for many time steps, recording data at high spatial or temporal resolution, or by combining the data for several individuals. If combining the data for several individuals, first perform the kinematic decomposition on each individual and plot both basis function sets with mean and standard errors. If the standard error regions overlap and/or the means are similar enough (as defined before the experiment begins), sample from each individual equally, so that the final curvature matrix for, say, 10 individuals has 1/10th the data from each individual.

Appendix B

Can flexibility help you float?

B.1 Introduction

In his treatise *On Floating Bodies* [5], Archimedes examined the stability of objects wholly or partially submerged in a fluid. He surmised that if an object is less dense than the suspending fluid, it will partially project above the surface, displacing a volume of fluid with a weight equal to its own. This proposition, commonly known as Archimedes' Principle, is true for large objects, but neglects capillary effects that arise at small scales, specifically, at scales small relative to the capillary length. Keller [76] generalized Archimedes' Principle to small floating bodies by showing that the vertical force from surface tension is equal to the weight of liquid displaced by the meniscus. We here extend this class of problems by elucidating the role of flexibility in interfacial flotation.

Many biological organisms that float, like hydrophytes (*e.g.*, water lilies) and water walking insects [20], are not entirely rigid. There are several reasons for organisms to be flexible, including decreased weight and increased robustness when subjected to external forces [99]. *Hydrophytics* are aquatic plants rooted in the soil. During times of flood, their petals bend and close, thereby protecting their genetic material in response to increasing hydrostatic pressure [124]. Flexibility is exploited by several creatures that reside at the water surface, both individually and collectively. The insect *Anurida* attracts others of its kind by bending its back and deforming the

interface, so that a colony can behave like a self-assembling raft [20]. Other such living rafts may form from assemblages of mosquito eggs [155] or whirligig beetles [160]. Though individual ants flounder at the interface, ant rafts, comprised of thousands of individuals, are able to stay afloat for months in the flood-prone rain forests of Brazil [103]. Might such interfacial organisms, as individuals or a collective, exploit flexibility to support a greater load?

The role of flexibility in interfacial flotation has only recently been considered. Vella *et al.*[158] examined the weight-bearing characteristics of a raft composed of thin rigid strips. As a model of the leg of a water-walking insect, Vella [156] examined the flexure of a floating cylindrical rod forced at one end. Floating hydrophobic rods of various cross-sectional shapes were studied by Liu *et al.* [93]. Reis *et al.* [124] computed the shape of a floating two-dimensional strip subjected to a point force at its center. For floating plates, one expects surface tension forces to dominate forces resulting from hydrostatic pressure for plates much smaller than the capillary length. The equilibrium shape of such small plates will thus have little influence on the maximum load the plate can support, which will be prescribed by its edge length. Conversely, large plates will be supported predominantly by hydrostatic pressure on the plate; consequently, maximum loads will be supported by plates that displace the most fluid.

In §B.2, we consider a two-dimensional hinged plate with a torsion spring, so that bending is permitted only at a single point. To determine whether flexibility is advantageous, we derive the maximum load (specifically, the maximum plate density) that can be supported. The effect of increasing spring stiffness on the equilibrium plate shape is determined. These results are useful in developing intuition for §B.3, where we generalize our model to the case of continuously deformable plates. The limiting cases of small and large plates are considered, and plate configurations and approximations for the optimal spring stiffness (those capable of supporting the greatest load) are derived. Our results are reviewed in §B.4, where their bearing on the form of some aquatic plants is discussed.

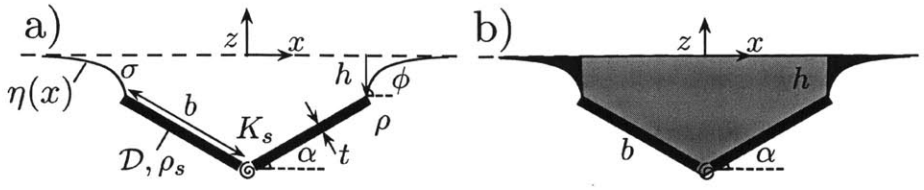

Figure B-1: a) Two-dimensional geometry of the hinged two-plate configuration. Two plates, each of length b, thickness t, and density ρ_s are connected by a torsion spring with spring constant K_s. The outer plate edges are a distance h below the undisturbed interface. Flexure causes the plates to lie at an angle α with respect to the horizontal. The density of the liquid is ρ and the surface tension is σ. b) Dark shaded regions show fluid displaced above the meniscus, whose weight is equal to the vertical component of surface tension, while the light shaded region shows the volume of fluid displaced above the plate.

B.2 Flotation of hinged plates

Here we examine the simplified case of two rigid plates connected by a torsion spring. Consider the two-dimensional geometry in which two infinitely long rigid plates of width b and thickness t (such that $b \gg t$) are connected by a torsion spring with spring constant K_s (Fig. B-1a). The air density is assumed to be negligible relative to that of the liquid, ρ, and the solid plate, ρ_s. The plate edge depth, h, is the distance from the undisturbed interface to the plate's outer edge and must be less than or equal to two capillary lengths; otherwise, the meniscus will collapse. The capillary length is defined as $\ell_c^2 = \sigma/\rho g$ where σ is surface tension and g is gravity. The hinge angle is α and the contact angle ϕ is related to the plate edge depth by $h = \ell_c\sqrt{2 - 2\cos\phi}$. There is some freedom in ϕ due to the possibility of pinning at the plate edge but we henceforth assume that $\phi \geq \pi/2$. To increase the load on the plate uniformly, its density ρ_s is increased. As the load increases, the plate will sink and, depending on the magnitude of K_s, bend. Beyond some maximum load (to be determined), the plate will sink. Our approach extends the work of Vella *et al.* [158] through consideration of the torsion spring, which imposes an energetic penalty to flexure.

B.2.1 Energetics

We seek to identify the configuration parameters (α, h) that minimize the total system energy. The potential energy associated with the work done on the system by external forces is V. We express V as the combination of work done by: hydrostatic pressure on the interface, $GPE_{\text{H,interface}}$, hydrostatic pressure on the plate, $GPE_{\text{H,plate}}$, gravity on the plate, GPE_{plate}, and surface tension on the plate, $E_{\text{s.t.}}$.

$$V = \quad GPE_{\text{H,interface}} + GPE_{\text{H,plate}} + GPE_{\text{plate}} + E_{\text{s.t.}} \tag{B.1}$$

We define U to be the combination of surface or "free" energy, SE, and the potential energy stored in the torsion spring, E_{spring}.

$$U = \quad SE + E_{\text{spring}} \tag{B.2}$$

A body will deform to the configuration that minimizes the system's total potential energy, $\Pi = U - V$. We thus identify the configuration parameters that result in zero variation in total potential energy, $\delta\Pi = \delta U - \delta V = 0$, or that correspond to a stationary point in the energy landscape [123]. The variation in the energy terms is:

$$\begin{aligned}\delta V = \quad & \rho g \int \eta(x) dx \delta\epsilon + \rho g \left(\left(2bh\cos\alpha + b^2\cos\alpha\sin\alpha\right)\delta h + \left(\frac{b^3}{3}\sin\alpha + b^2 h\right)\delta\alpha \right) \ldots \\ & -\rho_s g t \left(2b\delta h + b^2\cos\alpha\delta\alpha\right) + 2\sigma\left(\sin\phi\delta h + b\left(\sin\phi\cos\alpha - \cos\phi\sin\alpha\right)\delta\alpha\right) \end{aligned} \tag{B.3}$$

$$\delta U = \quad \sigma\delta\ell + 2K_s\alpha\delta\alpha = \sigma\int \nabla\cdot\vec{n}\, dx\delta\epsilon + K_s\alpha\delta\alpha, \tag{B.4}$$

where $z = \eta(x)$ is the known equation of the interface and $\delta\epsilon$ is the incremental displacement of the interface. The outward vector normal to the interface is $\vec{n}$ and $\delta\ell$ is the incremental change in arc length along the meniscus. We describe the plate configuration by parameters α and h and set the variation in energy with each

Table B.1: Relevant dimensionless groups for a flexible floating plate

Plate Half-Length	b	$\beta = \frac{b}{\ell_c}$	Spring constant	$k_s = \frac{K_s}{\rho g \ell_c^3}$
Plate Thickness	t	$\tau = \frac{t}{\ell_c}$	Load	$\mathcal{D} = D\tau = \frac{\rho_s - \rho}{\rho}\tau$
Plate Edge Depth	h	$H = \frac{h}{\ell_c}$	Bond number	$Bo = \frac{b^2 \rho g}{\sigma} = \frac{b^2}{\ell_c^2} = \beta^2$
Density	$\rho_s - \rho$	$D = \frac{\rho_s - \rho}{\rho}$		

parameter to zero. Two equations must be satisfied for static equilibrium:

$$\frac{\delta \Pi}{\delta h} = -\rho g \left(2bh\cos\alpha + b^2 \cos\alpha \sin\alpha\right) + 2b\rho_s g t - \sigma h\sqrt{4-h^2} = 0 \quad \text{(B.5)}$$

$$\frac{\delta \Pi}{\delta \alpha} = 2K_s\alpha - \rho g\left(\frac{b^3}{3}\sin\alpha + b^2 h\right) + \rho_s g t b^2 \cos\alpha + \ldots \quad \text{(B.6)}$$

$$\sigma b\left(-h\sqrt{4-h^2}\cos\alpha + \left(2-h^2\right)\sin\alpha\right) = 0$$

These equations express, respectively, the force balance on the plate and the balance of torques about the torsion spring. The surface energy and the gravitational potential energy associated with the interface cancel precisely, as follows from application of the Young-Laplace equation at the interface, $\rho g \eta(x) = \sigma \nabla \cdot \vec{n}$: along the meniscus, the curvature and hydrostatic pressures are in balance.

Buckingham's theorem indicates five dimensionless groups, defined in table B.1. The Bond number, $Bo = (b/\ell_c)^2 = \beta^2$, is of particular interest. We focus on the two extremes of plate size; henceforth, "small" and "large" plates correspond to the limits of $\beta \ll 1$ and $\beta \gg 1$, respectively. Non-dimensionalizing (B.5) yields:

$$2\beta\mathcal{D} = 2\beta H\cos\alpha + \beta^2\cos\alpha\sin\alpha + H\sqrt{4-H^2} \quad \text{(B.7)}$$

$$2k_s\alpha + \mathcal{D}\beta^2\cos\alpha = \frac{\beta^3}{3}\sin\alpha + \beta^2 H + \beta\cos\alpha H\sqrt{4-H^2}\ldots \quad \text{(B.8)}$$
$$+\beta\sin\alpha\left(H^2-2\right)$$

(B.7) expresses the dimensionless force balance, from which the generalization of Archimedes' Principle emerges [76]: the weight of the plate is equal to that of the fluid displaced above both the meniscus and the plate (Fig. B-1b). (B.8) expresses

the dimensionless torque balance: the torques resulting from hydrostatic pressure and surface tension are resisted by the spring torque and that resulting from the weight of the plate.

We proceed by determining the k_s that can support the maximum load $\mathcal{D}$ for a fixed β. The problem is expressed as an optimization problem,

$$\max_{\alpha,H,k_s} \quad \mathcal{D}(\beta,\alpha,H,k_s) \quad \text{s.t.} \quad \Sigma F(\beta,\alpha,H,\mathcal{D})=0, \quad \Sigma\tau(\beta,\alpha,H,\mathcal{D},k_s)=0 \tag{B.9}$$

where the configuration (α, H) and optimal stiffness (k_s^*) completely describe the solution. From the objective function and first constraint, the configuration parameters and optimal load are determined analytically as a function of plate size:

$$\mathcal{D}_{\max}=\frac{\beta}{4}+\sqrt{2}+\frac{1}{\beta}, \quad \alpha_{\max\mathcal{D}}=\arccos\left(\sqrt{\frac{1}{2}+\frac{8+\beta^2\left(-2+\sqrt{2}\beta\right)}{16+\beta^4}}\right) \tag{B.10}$$

$$H_{\max\mathcal{D}}=\frac{2\left(\sqrt{2}+\beta\right)}{\sqrt{4+2\sqrt{2}\beta+\beta^2}}.$$

Figs. B-2a and b illustrate the dependence of the optimal configuration parameters and density on the plate size. (B.9) is reduced to a torque balance: $\Sigma\tau(\beta,k_s^*)=0$. It is straightforward to solve this torque balance for the optimal stiffness, k_s^*, as a function of plate size. The relationship between plate size and optimal stiffness is shown in Fig. B-3.

The behavior in the limits of large and small plates is deduced by considering the dominant terms in (B.7) and (B.8). For small plates, the force and torque balances become, respectively: $2\beta\mathcal{D}\approx H\sqrt{4-H^2}$ and $2k_s\alpha+\mathcal{D}\beta^2\cos\alpha\approx\beta\cos\alpha H\sqrt{4-H^2}+\beta\sin\alpha\left(H^2-2\right)$. The force and torque balances are prescribed by contributions from the spring, the weight of the plate, and the surface tension. It is clear that $H=\sqrt{2}$ maximizes the vertical component of surface tension acting on the plate, in accord with Fig. B-2a. This depth also maximizes the liquid displaced, consistent with the generalization of Archimedes' Principle [76]. We see from Fig. B-4a that for small plates ($\beta\ll 1$), bending only serves to reduce the column of fluid displaced above the

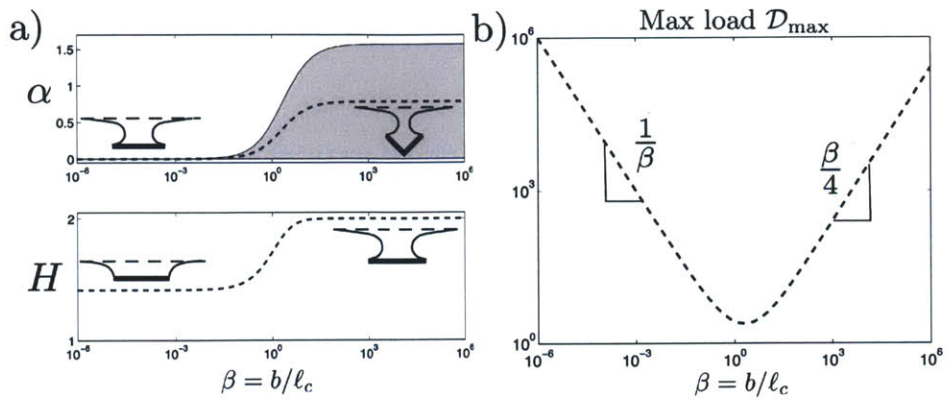

Figure B-2: a) Plate hinge angle α and plate edge depth H that maximize load as a function of plate size $\beta = b/\ell_c$. Small plates maximize the surface tension force by sinking to a depth H=$\sqrt{2}$ while large plates maximize fluid displaced by assuming a plate tilt angle $\alpha = \pi/4$. The shaded area represents the region where bending allows the plate to support a greater load than a flat plate of the same size. b) Maximum load as a function of dimensionless plate size, $\beta = b/\ell_c$.

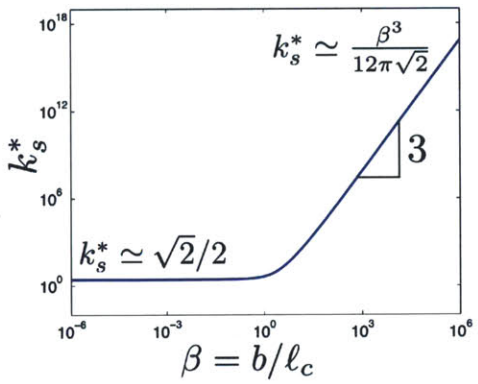

Figure B-3: Optimal stiffness k_s^* (specifically, that which bears the most weight) as a function of plate size. The optimal stiffness for large plates depends on size because the dominant terms in the force and torque balances are due to hydrostatic pressure and increase with plate size. The weight of small plates is supported primarily by surface tension, thus the independence of k_s^* on plate size for $\beta \ll 1$.

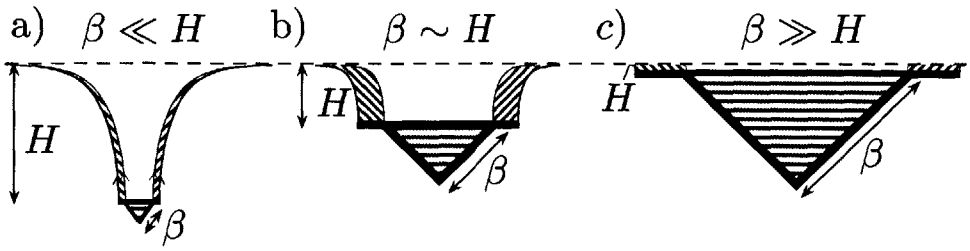

Figure B-4: The dependence on plate size. Horizontal striped regions represent fluid displaced by the bent plate only. Diagonal striped regions indicate where only the flat plate displaces fluid. a) For plates much smaller than a capillary length, the plate edge depth H determines the amount of fluid displaced (accurate to $\mathcal{O}(\beta/H)$), and therefore the maximum plate load. Bending such small plates decreases the total fluid displaced by narrowing the column of fluid displaced above the plate thereby diminishing its weight-bearing characteristics. b) Bending is advantageous for plates on the order of the capillary length if more fluid is displaced by bending than is lost by narrowing the fluid column above the plate. c) Large plates displace significantly more fluid by bending: flexibility thus enables them to bear greater loads.

plate, decreasing the load the plate can bear. In the limit of $\beta \to 0$, the optimal hinge angle is zero and $k_s^* = \sqrt{2}$, as may be deduced by considering higher order terms. For these conditions, the maximum load is $\mathcal{D}_{\max} \sim 1/\beta$. Plates with $k_s < k_s^*$ are bent and support slightly smaller loads, while stiffer plates remain flat.

For plates much larger than the capillary length, $\beta \gg 1$, the force and torque balances become, respectively: $2\beta\mathcal{D} \approx \beta^2 \cos\alpha \sin\alpha$, and $2k_s\alpha + \mathcal{D}\beta^2 \cos\alpha \approx \frac{\beta^3}{3} \sin\alpha$. The force and torque balances are now prescribed by the spring, the weight of the plate and hydrostatic pressure. The configuration parameter H does not appear in the leading order terms for the force and torque balances of large plates, indicating that large plates are insensitive to surface tension. We return to Archimedes' Principle: the plate load is maximized when the most fluid is displaced, or $\alpha = \pi/4$, as in Fig. B-2a. From the torque balance, the optimal stiffness associated with this configuration is $k_s^* = \beta^3/(6\sqrt{2}\pi)$ (Fig. B-3), for which the load is $\mathcal{D}_{\max} \sim \beta/4$ (Fig. B-2b). When the plate is much larger than the plate edge depth H, the bulk of the fluid displaced is associated with the plate deformation rather than the meniscus, as shown in Fig. B-4b.

For any plate size, bending is advantageous if the plate size and tilt angle lies in the shaded region in Fig. B-2a, allowing the plate to bear a greater load than a flat plate. For plates on the order of a capillary length, $\beta \approx \mathcal{O}(1)$, both the hydrostatic pressure and surface tension are important in the force and torque balances. For these plates, the optimal bending angle is determined by the tradeoff between fluid displaced by bending the plate and the narrowing of the fluid column displaced above the plate. Thus, as shown in Fig. B-2a, the optimal plate tilt angle lies between 0 and $\pi/4$, the optimal angles in the limiting cases of small and large plates, respectively.

B.3 Continuously deformable plates

We proceed by extending our results from a hinged to a continuously deformable plate. For small plates, we expect flat plates, at a depth of $\sqrt{2}\ell_c$, to support the greatest load since they displace the most fluid (as in Fig. B-4a). We anticipate flexure to assist with bending for plates above a critical size. In the larger plate limit, the optimal weight-bearing large plate shape to be that which displaces the most fluid, specifically, a semicircle.

For a continuously deformable plate of a given size, we search for the plate shape that minimizes the total energy while maximizing the plate load: max $\mathcal{D}$ s.t. $\delta\Pi = 0$. Components of potential energy for continuously deformable plates are a generalization of those developed in §B.2 and can be written in integral form. We discretize the continuous plate into $2N$ segments of equal length and allow each segment's orientation $\vec{\theta} = (\theta_1, \theta_2, ...\theta_N)$ to vary (Fig. B-5a). Boundary conditions are specified in Fig. B-5a. The principle of minimum potential energy results in a vertical force balance and a torque balance about each hinge, reducing the optimization problem to:

$$\begin{aligned} \max_{H,\vec{\theta}} \quad & \mathcal{D}(\beta, \vec{\theta}, H, k_s) \\ \text{s.t.} \quad & \Sigma F(\beta, \vec{\theta}, H, k_s, \mathcal{D}) = 0,\ \Sigma\tau_i(\beta, \vec{\theta}, H, k_s, \mathcal{D}) = 0,\ i = 1, 2, ...N \end{aligned} \tag{B.11}$$

The problem is solved numerically using the MATLAB optimization toolbox. For

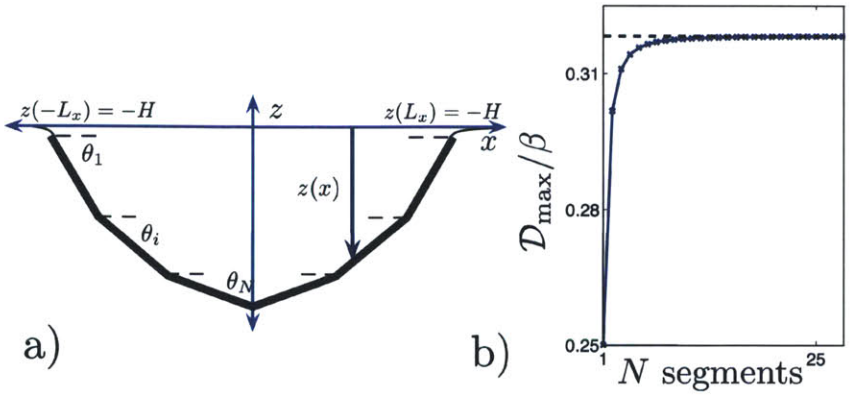

Figure B-5: a) Schematic of the continuous plate configuration discretized into $2N$ segments, where L_x is the horizontal projection of the plate. b) Maximum load, $\mathcal{D}_{\max}/\beta$, determined by numerical optimization of a plate comprised of $2N$ segments. The theoretically predicted maximum load (corresponding to the optimal shape of a semicircle) and the numerical solution are within 0.03% by $N = 25$.

small plates, the equilibrium plate shape that minimizes energy and maximizes density is a flat plate, and arises with any non-zero bending stiffness. As in §B.2, the surface tension forces dominate and the flat plate supports the maximum load, $\mathcal{D}_{\max} \sim 1/\beta$, in this small plate limit.

The large plate shape that displaces the most fluid above the plate and supports the maximum density is necessarily a semicircle, an intuitively satisfying result confirmed by the numerical optimization. Fig. B-5b shows that for $N > 25$ the maximum load for large plates determined numerically by the discrete shape is within 0.03% of the theoretical value for the continuous optimal shape.

Increasing k_s is equivalent to increasing the energetic cost of bending. As a result, as k_s is increased progressively, the optimal plate shape is gradually less bent and displaces less liquid, as shown in Fig. B-6a in the case of large plates, $Bo \gg 1$. For each of these shapes, the torque is balanced at every point along the plate. We note that the most flexible plate is that which bears the greatest load and that this load decreases with increasing k_s, as illustrated in Fig. B-6b. In the absence of any energetic penalty to bending ($k_s = 0$), the plate assumes a semicircular form. The torque resulting from hydrostatic pressure balances the torque from the weight of the

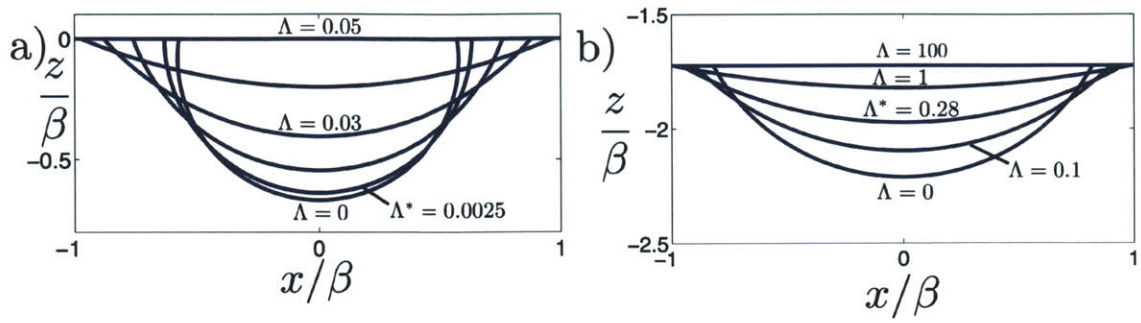

Figure B-6: a) Plate shapes that maximize load for various stiffnesses at large Bo. b) The maximum load decreases monotonically with increasing spring stiffness, k_s, for the continuous plate. The most flexible plate displaces the most fluid, and so supports the greatest load. Thus, the optimal stiffness is zero, $k_s^* = 0$ in this large plate limit.

plate at each point along the semicircle. The plate shapes in Fig. B-6a resemble those presented by [124] for an elastic plate loaded at its midpoint.

B.4 Discussion

We have demonstrated that flexibility can assist in interfacial flotation for bodies on the order of the capillary length and larger. Consideration of the minimum total potential energy yielded force and torque balances whose form depended on body size. For plates much smaller than the capillary length, flat, rigid plates bear the most weight. Such small plates are supported predominately by capillary forces, thus plate bending results in a diminution of fluid displaced above the plate, as illustrated in Fig. B-4a, and so diminishes buoyancy.

A large plate supports a maximum load by deforming to $\alpha = \pi/4$ in the hinged case and to a semicircle in the continuous case, thereby displacing the maximum fluid volume, and minimizing the potential energy of the plate. Increasing plate stiffness increases the energetic cost of bending, forcing the plate to flatten (Fig. B-6a), thus decreasing its load-bearing capacity (Fig. B-6b). We can readily infer the optimal shape for a large three-dimensional "plate" with no stiffness: for a fixed surface area,

a hemisphere maximizes the fluid displaced.

Many water-walking insects are flexible and have length scales on the order of a capillary length [20]. At this scale, we have seen that bending allows an object to bear a greater load than if flat. To model raft-like structures and plants found in nature, we must generalize our theory to three dimensions. Nevertheless, our study does provide some insight for three-dimensional objects such as capillary rafts. [157] noted that capillary rafts comprised of many particles exhibit elastic behavior, and inferred effective values of the Young's modulus and Poisson ratio for rafts comprised of various materials, Similarly, [103] inferred the effective constitutive properties of the ant raft. Our study indicates the manner in which flexibility assists the flotation of these rafts. Floating flexible biological organisms may deform in a variety of manners. Plants such as lily pads may buckle or experience out-of-plane folding. Films or membrane-like materials can stretch to withstand large loads, while flowers may avoid buckling during submergence by having petals that overlap [124].

Modeling more complex rheology and geometry, *e.g.*, variable stiffness distribution along the plate, would be relatively straightforward using our approach. Comparison with data on the distribution of material stiffnesses and typical load cycles in various organisms would provide quantitative confirmation that water plants and floating colonies of interfacial creatures use flexibility to improve flotation.

Appendix C

Biomimicry and the culinary arts

Biomimicry has become a central theme in the engineering sciences, and can count the glider, Velcro and Scotch tape among its successes [8]. Most recently, man has looked to nature to inspire means of reducing drag and corrosion on rigid surfaces by decorating the surface with microstructure, now possible owing to recent advances in microfabrication and materials science [39]. Biocapillarity, the relatively new subject at the border of interfacial science and biology, involves the elucidation of natural mechanisms reliant on interfacial tension. We present here two devices developed for use in the culinary arts, motivated by recent studies in biocapillarity.

Surface tension σ is a tensile force per unit length that acts along fluid-fluid or fluid-gas interfaces [32]. At the fluid-gas interface, the effects of surface tension dominate those of gravity for fluid systems small relative to the capillary length $\ell_c = \sqrt{\sigma/\rho g}$, where ρ represents the fluid density and g gravity. For air-water systems, the capillary length corresponds roughly to the size of a raindrop. Surface tension is thus an important player in the lives of small creatures such as insects, for their propulsion [20], fluid uptake [79], and many other critical functions [21]. Py *et al.* [121] demonstrated that interfacial forces may fold flexible solid sheets, and so presented the first examples of capillary origami. In their experiments, drops were placed on flexible sheets which folded into 3D shapes in response to interfacial forces, provided the sheet's size, L, exceeded the elastocapillary length, $L_{ec} = \sqrt{B/\sigma}$, where B is the sheet's bending stiffness.

Just as scientists draw inspiration from nature, chefs may draw inspiration from science to create novel processes and edible materials [154]. Our collaboration at the interface of the culinary arts has led to the development of two dynamic edible devices inspired by natural mechanisms reliant on, respectively, chemically induced surface tension gradients and capillary origami.

C.1 The cocktail boat

Marangoni flows are those forced by surface tension gradients, as may result from gradients in temperature or chemistry along an interface [131]. The most commonly observed Marangoni flow is that responsible for the tears of wine [147]. Owing to the dependence of surface tension on alcohol concentration, evaporation of alcohol from the thin film on the side of a wine glass increases the local surface tension relative to that of the bulk, and the resulting surface tension gradient pumps fluid up the thin film. Fluid thus accumulates in a horizontal band at the top of the film that grows until becoming gravitationally unstable and releasing the tears of wine. The tears, whose form serves as an indicator of the sugar and alcohol content of the wine, fall until there is insufficient alcohol to drive the system.

Surfactants, such as common soaps, are molecules that find it energetically favorable to reside at the free surface, and act to decrease the local surface tension. The simplest demonstration of a Marangoni flow is the soap boat, a close cousin of the cocktail boat. If a small floating object such as a toothpick of width w is placed on a water surface after one end has been dipped in soap, the surface tension at the clean end is greater than at the soapy end by an amount $\Delta\sigma$; consequently, it is propelled away from the soap by a Marangoni force of characteristic magnitude $F_M = w\Delta\sigma$ (e.g., [109]). The boat thus accelerates until the hydrodynamic drag balances the propulsive Marangoni force. Most soaps decrease the surface tension at an air-water surface, $\sigma = 70$ dynes/cm, by a factor of two, resulting in the soap boat achieving speeds of approximately 10 cm/s. Note that the soap boat's journey is relatively short ($\sim$10 sec) in a closed geometry as the interface soon becomes satu-

rated in surfactant, which suppresses the propulsive surface tension gradient. Nakata *et al.* [109] demonstrated that this limitation may be avoided by using volatile surfactants such as camphor, which evaporates rapidly from the surface, thus enabling sustained Marangoni propulsion.

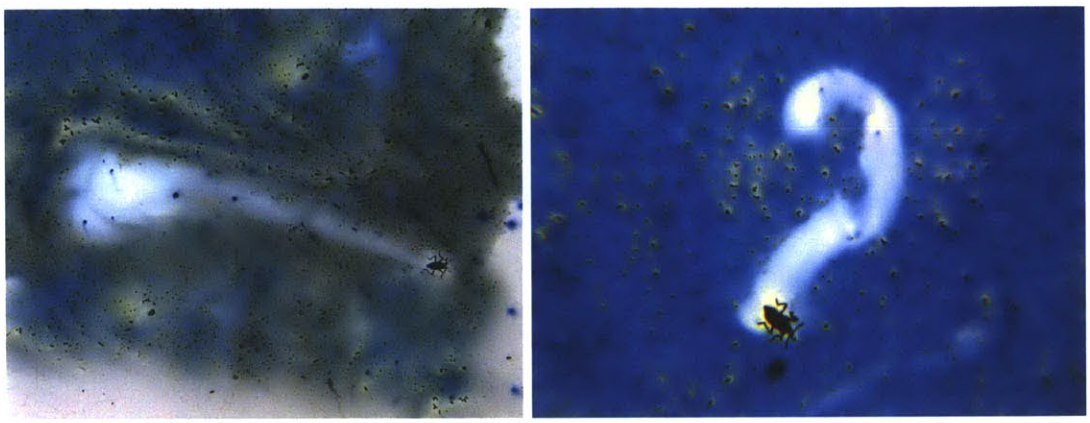

Figure C-1: The semi-aquatic insect Microvelia releases a surface-active lipid in its wake, resulting in a surface tension gradient that propels it forward via Marangoni propulsion. The Microvelia is approximately 2 mm in length [20].

Marangoni propulsion as a means of biolocomotion was first reported by Billard and Bruylant[11] who observed its use by a terrestrial insect when it accidentally fell onto the water surface. By releasing a surfactant, specifically a surface-active lipid, it was able to propel itself toward and up the meniscus bordering land and so return to its preferred terrestrial environment. Marangoni propulsion by the rove beetle has been reported by Betz [10], and by semi-aquatic insects, for example Microvelia (Fig. C-1) and Velia, by Linsenmair and Jander [92] and Andersen [3]. Schlidknecht [129] found that the surfactant released by the rove beetle reduced the surface tension from 72 to 49 dynes/cm. Peak speeds during Marangoni propulsion for Microvelia are approximately 17 cm/s, or twice their peak walking speed [4]. In Fig. C-1, it is apparent that the surfactant ejected by Microvelia not only gives rise to a propulsive force, but clears the initially dyed surface layer in its wake. Marangoni propulsion by such insects is precisely analogous to that of the soap boat: the chemically-induced gradient in the surface tension generates a propulsive force [66].

The cocktail boat relies on precisely the same propulsive mechanism as the soap

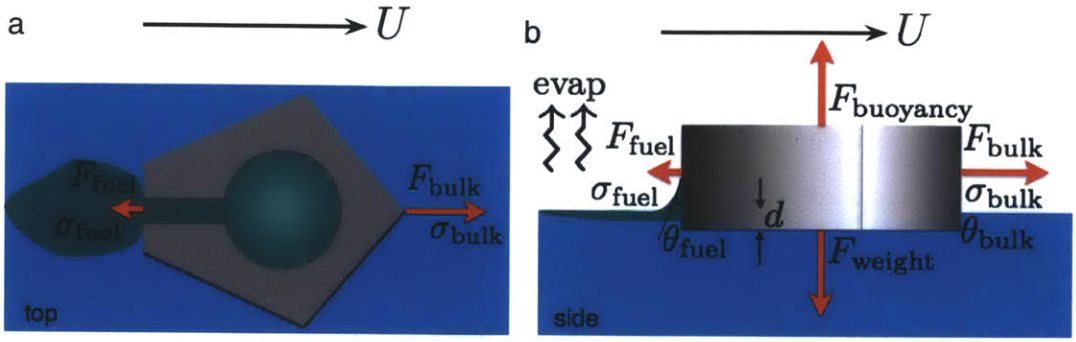

Figure C-2: a) Top and b) side view of the cocktail boat elucidates design considerations and the propulsion mechanism. A lighter boat is desirable, so that the boat's intrusion depth d, and induced drag, are minimized.

boat and the Marangoni swimmers. The floating cocktail boat (Fig. C-2) is filled with its fuel, alcohol, which spills into its wake by way of a small outlet on its aftward side. Alcohol acts to reduce both the surface tension and the contact angle on the aftward side, thus decreasing the horizontal force relative to that on the front (see Fig. C-2b). Alcohol reduces the surface tension at an air-water interface from approximately $\sigma_{bulk} = 70$ to $\sigma_{fuel} = 35$ dynes/cm. In our system, the contact angle between water and plastic is $\theta_{bulk} \simeq 80^o$ and between an alcohol-water mixture and plastic is $\theta_{fuel} \simeq 30^o$. Consequently, a cocktail boat of width $w = 1$ cm is subjected to a propulsive force

$$F_{prop} = (\sigma_{bulk} \sin\theta_{bulk} - \sigma_{fuel} \sin\theta_{fuel})\ w \simeq 51 \text{ dynes}, \tag{C.1}$$

owing to the fore-aft difference in surface tension and contact angles. The resulting steady speed U may be computed from the horizontal force balance, according to which F_{prop} is balanced by the drag force $F_{drag} = \rho U^2 wd$, where d is the intrusion depth of the boat, so wd its submerged exposed area (see Fig. C-2). We thus obtain

$$U = \sqrt{\frac{(\sigma_{bulk} \sin\theta_{bulk} - \sigma_{fuel} \sin\theta_{fuel})}{\rho d}}\ . \tag{C.2}$$

Observed peak speeds of the cocktail boat are approximately 10 cm/s. Like the camphor used by [109], alcohol is volatile and evaporates from the interface on a time scale faster than the motion of the boat. Consequently, the cocktail boat exhibits

sustained motion until it runs out of fuel.

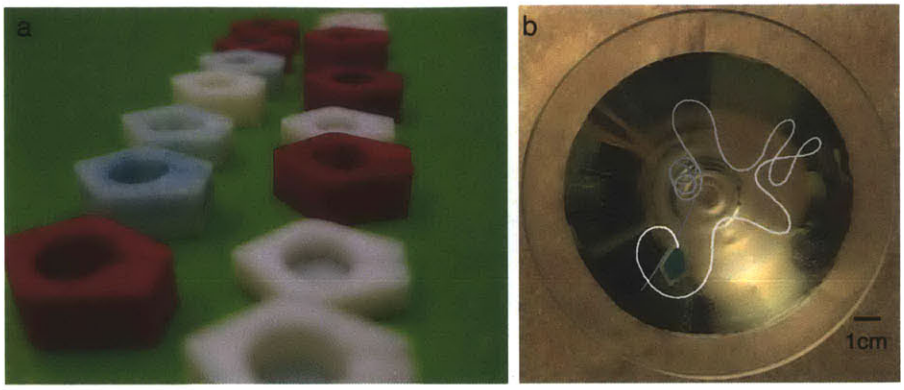

Figure C-3: a) A fleet of cocktail boats with varying shape and slit size were tested, fueled by different liquors. We found that the alcohol content of the fuel was the most important design factor for performance, with higher proof alcohol leading to faster and more vigorous boat motion. b) A cocktail boat propels itself, fueled by Bacardi 151 (75% alcohol). Boat lengths are approximately 1.5 cm.

Initial prototypes of the boats were first made of Acrylonitrile butadiene styrene (ABS plastic) generated on a Stratasys Dimension 3D printer. Boat designs with various slit sizes and shapes were tested, resulting in a range of speeds, stability, and travel duration. The boat performance was most sensitive to the slit size and alcohol concentration in the fuel rather than the shape of the boat's footprint. The longest runs achieved were two minutes. Subsequently, we cast edible cocktail boats from silicone molds. The molds were created using a 3D-printed mold negative. A number of different edible and semi-edible materials were used including gelatin, agar, melted wax and various candies. Once we had verified the feasibility of creating edible boats and optimized the mold design, ThinkFoodGroup refined the composition of the edible boats, making them more pleasing to both the eye and the palate.

C.2 The floral pipette

A family of flowers, including the water lily, float at the surface of ponds or lakes while remaining anchored to the underlying ground. When the water level rises, the petals or leaves wrap up, capturing an air pocket in order to keep the flower's genetic

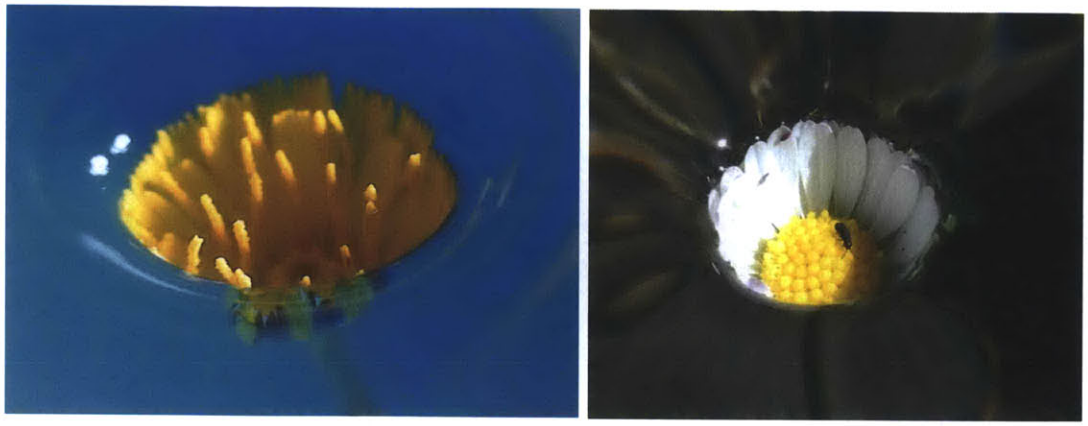

Figure C-4: Flowers that float at the air-water interface are supported by hydrostatic, elastic and capillary forces. The flower's petals close in the presence of high water levels to protect their genetic material ([71], www.wikipedia.org).

material dry (Fig. C-4). Since most such flowers are on a scale much larger than the capillary length, hydrostatic forces play the dominant role in prompting closure; however, capillary forces are critical in preventing water from intruding between the petals (Fig. C-5). Inspired by this class of floating flowers, [124] developed a technique for grabbing water that they termed the elastocapillary pipette, in which the role of gravity is reversed.

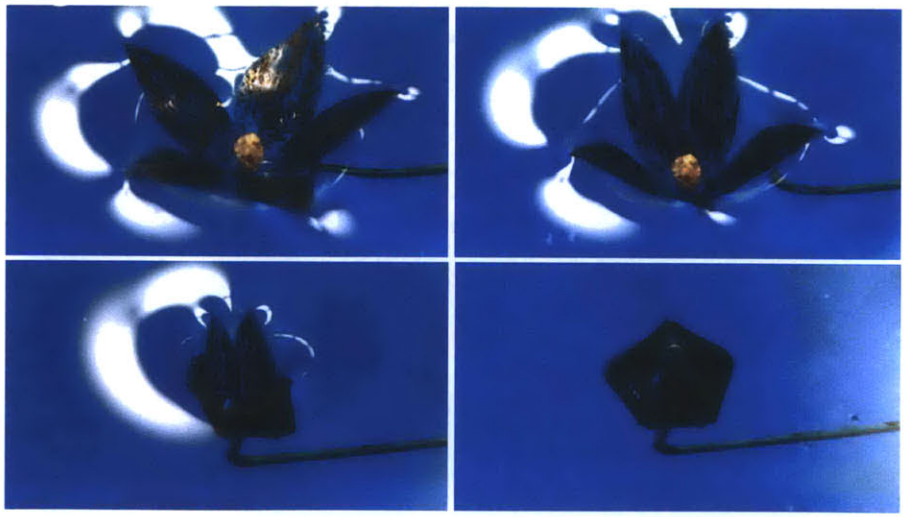

Figure C-5: When submerged, artificial flowers made of polymer elastic sheets mimic the petal closure observed in nature by floating flowers. The undeformed flower diameter is approximately 1.8 cm [71].

Instead of forcing the flower to sink relative to the interface (Figs. C-4 and C-5), an elastic sheet cut into the shape of a flower is drawn upwards, and grabs a volume of fluid from the free surface (Fig. C-6). As the flower is withdrawn from the surface it zips shut, giving rise to a fluid drop enclosed by an elastic shell. The hydrostatic suction associated with the vertical fluid displacement prompts the closure of the flower, while the leakage of fluid from the closing flower is prevented by surface tension. While the elastocapillary designs of [121] were constrained to scales less than the capillary length, for the pipette, hydrostatic pressure is causing rather than resisting the folding. Consequently, fluid capture is possible on a significantly larger scale, that of the the elastogravity length, $L_{eg} = \sqrt{B/\rho g}$ [124]. The synthetic flowers were composed of vinylpolysiloxane of thickness 0.25 mm and Young's modulus $E = 0.5$ MPa, resulting in a bending stiffness of $B \simeq 10^{-6}\text{Nm}^2$. [124] computed the petal shape that optimizes the fluid volume trapped in this manner, and so were able to successfully grab water with elastocapillary pipettes of diameter 5 cm.

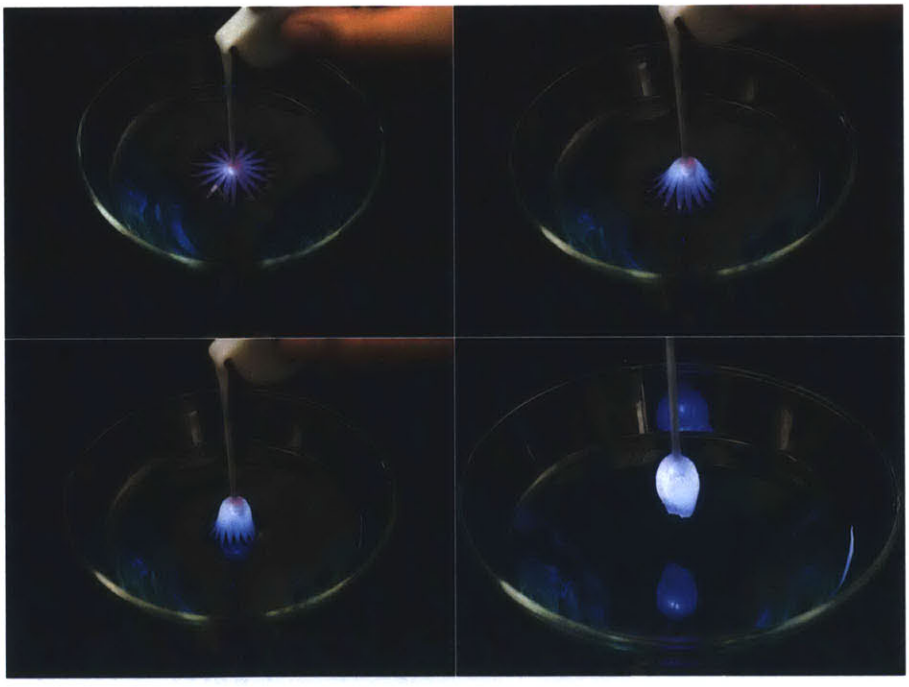

Figure C-6: The floral pipette is drawn up from the interface, enclosing a small volume of fluid. An LED at the pipette's center adds visual appeal.

The culinary application of the elastocapillary pipette is a device resembling a

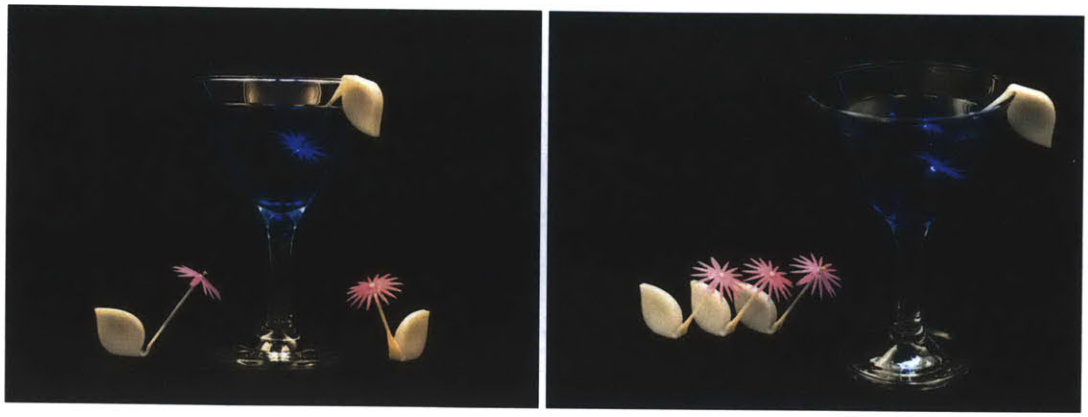

Figure C-7: The floral pipette features two resting positions: on a glass's edge and on a flat surface. Undeformed flowers are approximately 3.5 cm in diameter.

flower, constructed of edible gels and used as a means by which to imbibe fluid drop by drop, after which the flower itself is to be consumed. It represents an intriguing means by which to serve small fluid volumes, and is intended to be used in cleansing the palate between courses in multicourse meals. Flower geometries were optimized for the particular flower material according to the specifications detailed in [124], and molds for casting them were printed on a high-resolution 3D printer. Members of ThinkFoodGroup tested several edible gelling agents, such as gelatin and agar, in order to match the elastic properties of the synthetic materials used at MIT. They were thus able to ensure their robustness, and avoid damage to the petals during use. ThinkFoodGroup then explored flavors for the edible design with a view to integrating it into a dish.

Lastly, aesthetics motivated our incorporation of an LED into the center of the flower (Figs. C-6 and C-7). The petal and stem configuration were 3D printed and the LED was powered by a battery stored in the base, where a small switch controls the light. The shape of the base allows two resting configurations: on the side of a cocktail glass or on a flat surface, as illustrated in Fig. C-7.

C.3 Discussion

We have described the inspiration, mechanics, design and development of two instances of biomimicry in the culinary arts. Both involve striking examples of biocapillarity, in which nature exploits mechanisms that depend explicitly on interfacial effects. The cocktail boat, inspired by a class of insects that use Marangoni propulsion, is propelled in a cocktail glass by alcohol-induced surface tension gradients. The floral pipette is an example of capillary origami, an inversion of floating flowers that enables the imbibition of droplets drawn from a fluid interface. While both mechanisms may be of interest to the scientific and engineering communities, the development into a device of interest to the culinary arts required an additional step: the mimicry not only of nature's function, but of her elegance.

Bibliography

[1] T Ahmed, T S Shimizu, and R Stocker. Bacterial Chemotaxis in Linear and Nonlinear Steady Microfluidic Gradients. *Nano Letters*, 10(9):3379–3385, September 2010.

[2] L Alvarez, L Dai, B M Friedrich, N D Kashikar, I Gregor, R Pascal, and U B Kaupp. The rate of change in Ca2+ concentration controls sperm chemotaxis. *The Journal of Cell Biology*, 196(5):653–663, March 2012.

[3] N M Andersen. A comparative study of locomotion on the water surface in semi-aquatic bugs (Insects, Hemiptera, Gerromorpha) . *Vidensk. Meddr. Dan. Naturhist. Foren.*, 139:337–396, December 1976.

[4] N M Andersen. *The semiaquatic bugs (Hemiptera, Gerromorpha).* Phylogeny, adaptations, biogeography and classification. Brill Academic Pub, 1982.

[5] Archimedes. *The work of Archimedes.* Cambridge Univeristy Press, Cambridge, 1897.

[6] J Avron and O Raz. A geometric theory of swimming: Purcell's swimmer and its symmetrized cousin. *New Journal of Physics*, 10:063016, 2008.

[7] L Becker, S A Koehler, and H A Stone. On self-propulsion of micro-machines at low Reynolds number: Purcell's three-link swimmer. *Journal of Fluid Mechanics*, 490:15–35, 2003.

[8] J M Benyus. *Biomimicry.* Innovation Inspired by Nature. William Morrow Paperbacks, September 2002.

[9] S Berri, J Boyle, M Tassieri, I Hope, and N Cohen. Forward locomotion of the nematode C. elegans is achieved through modulation of a single gait. *HFSP Journal*, 2009.

[10] O Betz. Performance and adaptive value of tarsal morphology in rove beetles of the genus Stenus (Coleoptera, Staphylinidae). *J. Exp. Bio.*, 205(8):1097–1113, 2002.

[11] G Billard and C Bruylant. Sur un mode particulier de locomotion de certains stenus. *C. R. Soc. Biol.*, 59:102, January 1905.

[12] H Bjornsson and S A Venegas. A Manual for EOF and SVD analyses of Climatic Data. Technical Report 97-1, McGill University, Montreal, April 1997.

[13] A M Bloch, P Crouch, J Baillieul, and J Marsden. *Nonholonomic Mechanics and Control.* Springer, New York, 2003.

[14] J J Blum and J Lubliner. Biophysics of flagellar motility. *Annual Review of Biophysics and Bioengineering*, 2(1):181–219, 1973.

[15] M Bozkurttas, R Mittal, H Dong, G V Lauder, and P Madden. Low-dimensional models and performance scaling of a highly deformable fish pectoral fin. *Journal of Fluid Mechanics*, 631:311–342, 2009.

[16] C M Breder. Fish schools as operational structures. *Fish Bulletin*, 74:471–502, 1976.

[17] C Brennen and H Winet. Fluid mechanics of propulsion by cilia and flagella. *Annual Review of Fluid Mechanics*, 9:339–398, 1977.

[18] L J Burton and J W M Bush. Can flexibility help you float? *Physics of Fluids*, 24(10):101701, 2012.

[19] L J Burton, R L Hatton, H Choset, and A E Hosoi. Two-link swimming using buoyant orientation. *Physics of Fluids*, 22:091703, 2010.

[20] J W M Bush and D Hu. Walking on water: biolocomotion at the interface. *Annual Review of Fluid Mechanics*, 38:339–369, 2006.

[21] J W M Bush, D L Hu, and M Prakash. The integument of water-walking arthropods: form and function. *Advances in Insect Physiology*, 34:117–192, 2007.

[22] M Chalfie, J E Sulston, J G White, E Southgate, J N Thomson, and S Brenner. The neural circuit for touch sensitivity in Caenorhabditis elegans. *The Journal of Neuroscience*, 5(4):956–964, 1985.

[23] B Chan, S Ji, C Koveal, and A E Hosoi. Mechanical devices for snail-like locomotion. *Journal of Intelligent Material Systems and Structures*, 18(2):111–116, May 2006.

[24] S Childress. *Mechanics of Swimming and Flying.* Cambridge University Press, July 1981.

[25] H Choset, J Luntz, E Shammas, and T Rached. Design and motion planning for serpentine robots. In *Smart Structures and Materials 2000: Smart Electronics and MEMS, Proceedings of SPIE*, 2000.

[26] N Cohen and J H Boyle. Swimming at low Reynolds number: A beginner's guide to undulatory locomotion. *Contemporary Physics*, 51(2):103–123, 2010.

[27] S P Colin, J H Costello, J O Dabiri, A Villanueva, J B Blottman, B J Gemmell, and S Priya. Biomimetic and Live Medusae Reveal the Mechanistic Advantages of a Flexible Bell Margin. *PLoS ONE*, 7(11):e48909, November 2012.

[28] S P Cook, C J Brokaw, C H Muller, and D F Babcock. Sperm chemotaxis: egg peptides control cytosolic calcium to regulate flagellar responses. *Developmental Biology*, 165(1):10–19, 1994.

[29] M P Cosson, D Carre, and J Cosson. Sperm chemotaxis in siphonophores. II. Calcium-dependent asymmetrical movement of spermatozoa induced by the attractant. *Journal of Cell Science*, 68(1):163–181, 1984.

[30] R Cox. The motion of long slender bodies in a viscous fluid. Part 1. General theory. *Journal of Fluid Mechanics*, 44:791–810, 1970.

[31] O M Curet, N A Patankar, G V Lauder, and M A MacIver. Mechanical properties of a bio-inspired robotic knifefish with an undulatory propulsor. *Bioinspiration & Biomimetics*, 6(2):026004, April 2011.

[32] P de Gennes, F Brochard-Wyart, and D Quere. *Capillarity and Wetting Phenomena.* Drops, Bubbles, Pearls, Waves. Springer Verlag, 2003.

[33] P Dehal, Y Satou, R K Campbell, J Chapman, B Degnan, A De Tomaso, B Davidson, A Di Gregorio, M Gelpke, D M Goodstein, N Harafuji, K Hastings, I Ho, K Hotta, W Huang, T Kawashima, P Lemaire, D Martinez, I A Meinertzhagen, S Necula, M Nonaka, N Putnam, S Rash, H Saiga, M Satake, A Terry, L Yamada, H Wang, S Awazu, K Azumi, J Boore, M Branno, S Chinbow, R DeSantis, S Doyle, P Francino, D N Keys, S Haga, H Hayashi, K Hino, K S Imai, K Inaba, S Kano, K Kobayashi, M Kobayashi, B Lee, K W Makabe, C Manohar, G Matassi, M Medina, Y Mochizuki, S Mount, T Morishita, S Miura, A Nakayama, S Nishizaka, H Nomoto, F Ohta, K Oishi, I Rigoutsos, M Sano, A Sasaki, Y Sasakura, E Shoguchi, T Shin-i, A Spagnuolo, D Stainier, M M Suzuki, O Tassy, N Takatori, M Tokuoka, K Yagi, F Yoshizaki, S Wada, C Zhang, P D Hyatt, F Larimer, C Detter, N Doggett, T Glavina, T Hawkins, P Richardson, S Lucas, Y Kohara, M Levine, N Satoh, and D S Rokhsar. The Draft Genome of Ciona intestinalis: Insights into Chordate and Vertebrate Origins. *Science*, 298(5601):2157–2167, December 2002.

[34] Y Ding, N Gravash, C Li, R D Maladen, S S Sharpe, P B Umbanhowar, D I Goldman, and N Mazouchova. Comparative studies reveal principles of movement on and within granular media. In *The IMA Volumes in Mathematics and its Applications*, 2012.

[35] Y Ding, R D Maladen, P B Umbanhowar, A Kamor, and D I Goldman. Biophysically inspired development of a sand swimming robot. In *Proceedings of Robotics: Science and Systems*, 2010.

[36] R Dreyfus, J Baudry, M Roper, and M Fermigier. Microscopic artificial swimmers. *Nature*, 437:862, 2005.

[37] B P Epps, P Valdivia y Alvarado, K Youcef-Toumi, and Alexandra H Techet. Swimming performance of a biomimetic compliant fish-like robot. *Experiments in Fluids*, 47(6):927–939, June 2009.

[38] L J Fauci and Amy McDonald. Sperm motility in the presence of boundaries. *Bulletin of Mathematical Biology*, 57(5):679–699, September 1995.

[39] E A Favre and N O Fuentes. *Functional Properties of Bio-Inspired Surfaces.* Characterization and Technological Applications. World Scientific Publishing Company, December 2009.

[40] F E Fish. Energetics of swimming and flying in formation. *Comments on Theoretical Biology*, 5:283–304, 1999.

[41] B M Friedrich, I H Riedel Kruse, J Howard, and F Jülicher. High-precision tracking of sperm swimming fine structure provides strong test of resistive force theory. *Journal of Experimental Biology*, 213:1226–1234, 2010.

[42] H Fu, T Powers, and C Wolgemuth. Theory of swimming filaments in viscoelastic media. *Physical Review Letters*, 99:258101, 2007.

[43] R J Full and D E Koditschek. Templates and anchors: neuromechanical hypotheses of legged locomotion on land. *Journal of Experimental Biology*, 202(23):3325–3332, 1999.

[44] E A Gaffney, H Gadelha, D J Smith, J R Blake, and J C Kirkman-Brown. Mammalian Sperm Motility: Observation and Theory. *Annual Review of Fluid Mechanics*, 43(1):501–528, January 2011.

[45] C Gong, M J Travers, X Fu, and H Choset. Extended Gait Equation for Sidewinding. In *Proceedings of the IEEE International Conference on Robotics and Automation (ICRA)*, pages 1–6, Karlsruhe, Germany, February 2013.

[46] D Gonzalez-Rodriguez and E Lauga. Reciprocal locomotion of dense swimmers in Stokes flow. *Journal of Physics: Condensed Matter*, 21:204103, 2009.

[47] J Gray and G J Hancock. The propulsion of sea-urchin spermatozoa. *Journal of Experimental Biology*, 32:802–814, 1955.

[48] J S Guasto. Digitizing sea urchin sperm with MATLAB, October 2011.

[49] J S Guasto, R Rusconi, and R Stocker. Fluid mechanics of planktonic microorganisms. *Annual Review of Fluid Mechanics*, (44):373–400, 2012.

[50] J S Guasto, R K Zimmer, and R Stocker. Chemotaxis and sensing of marine invertebrate sperm. *In preparation*, 2013.

[51] A Guerrero, T Nishigaki, J Carneiro, Y Tatsu, C D Wood, and A Darszon. Tuning sperm chemotaxis by calcium burst timing. *Developmental Biology*, 344(1):52–65, 2010.

[52] Z V Guo, A C Hart, and S Ramanathan. Optical interrogation of neural circuits in Caenorhabditis elegans. *Nature Methods*, 6(12):891–896, November 2009.

[53] R L Hatton. *Geometric Mechanics of Locomotion and Optimal Coordinate Choice*. PhD thesis, Carnegie Mellon University, Pittsburgh, April 2011.

[54] R L Hatton, L J Burton, A E Hosoi, and H Choset. Geometric maneuverability with applications to low Reynolds number swimming. In *IEEE/RSJ International Conference on Intelligent Robots and Systems*, pages 3893–3898, 2011.

[55] R L Hatton and H Choset. Connection vector fields for underactuated systems. In *2nd Biennial IEEE/RAS-EMBS International Conference on Biomedical Robotics and Biomechatronics*, pages 451–456. IEEE, 2008.

[56] R L Hatton and H Choset. Connection vector fields and optimized coordinates for swimming systems at low and high Reynolds numbers. In *Proceedings of the ASME Dynamic Systems and Controls Conference (DSCC)*, pages 817–824, 2010.

[57] R L Hatton and H Choset. Optimizing coordinate choice for locomoting systems. In *2010 IEEE International Conference on Robotics and Automation (ICRA)*, pages 4493–4498, Anchorage, AK, 2010.

[58] R L Hatton and H Choset. Geometric motion planning: The local connection, Stokes's theorem, and the importance of coordinate choice. *The International Journal of Robotics Research*, 30(8):988–1014, 2011.

[59] R L Hatton and H Choset. Kinematic cartography for locomotion at low Reynolds numbers. In *Proceedings of Robotics: Science and Systems*, December 2011.

[60] R L Hatton and H Choset. Nonconservativity and noncommutativity in locomotion. *Society for Industrial and Applied Mathematics*, pages 1–31, July 2012.

[61] R L Hatton and H Choset. Nonconservativity and Noncommutativity in Locomotion. *SIAM Journal on Applied Dynamical Systems*, (Submitted), 2013.

[62] R L Hatton, R A Knepper, H Choset, D Rollinson, C Gong, and E Galceran. Snakes on a plan: toward combining planning and control. In *Proceedings of the IEEE International Conference on Robotics and Automation (ICRA)*, Karlsruhe, Germany, May 2013.

[63] J E Himes, J A Riffell, C A Zimmer, and R K Zimmer. Sperm chemotaxis as revealed with live and synthetic eggs. *The Biological Bulletin*, 220:1–5, 2011.

[64] S G Hinch and P S Rand. Optimal swimming speeds and forward-assisted propulsion: energy-conserving behaviours of upriver-migrating adult salmon. *Canadian Journal of Fisheries and Aquatic Sciences*, 57:2470–2478, April 2000.

[65] S Hirose. *Biologically inspired robots.* Snake-like locomotors and manipulators. Oxford University Press, USA, 1993.

[66] D Hu and J W M Bush. Meniscus-climbing insects. *Nature*, 437:733–736, 2005.

[67] D Hu, B Chan, and J W M Bush. The hydrodynamics of water strider locomotion. *Nature*, 424:663–666, 2003.

[68] I T Jolliffe. *Principal Component Analysis.* Springer Verlag, October 2002.

[69] S Jung. Caenorhabditis elegans swimming in a saturated particulate system. *Physics of Fluids*, 22:031903, 2010.

[70] S Jung, S Lee, and A Samuel. Swimming C. elegans in a wet granular medium. *Chaos: An Interdisciplinary Journal of Nonlinear Science*, 18(4):041106–041106–1, 2008.

[71] S Jung, P Reis, J James, C Clanet, and J W M Bush. Capillary origami in nature. *Physics of Fluids*, 21:091110, September 2009.

[72] S Jung, A G Winter V, and A E Hosoi. Dynamics of digging in wet soil. *International Journal of Non-Linear Mechanics*, 46(4):602–606, May 2011.

[73] E Kanso, J Marsden, C Rowley, and J Melli. Locomotion of articulated bodies in a perfect fluid. *Journal of Nonlinear Science*, 15:225–289, 2005.

[74] J Karbowski, C J Cronin, A Seah, J E Mendel, D Cleary, and P W Sternberg. Conservation rules, their breakdown, and optimality in Caenorhabditis sinusoidal locomotion. *Journal of Theoretical Biology*, 242(3):652–669, June 2006.

[75] U B Kaupp, N D Kashikar, and I Weyand. Mechanisms of sperm chemotaxis. *Annual Review of Physiology*, 70:93–117, 2008.

[76] J Keller. Surface tension force on a partly submerged body. *Physics of Fluids*, 10(11):3009–3010, 1998.

[77] S D Kelly and R M Murray. Geometric Phases and Robotic Locomotion. *Journal of Robotic Systems*, 12:417–431, 1995.

[78] S Kim, M Spenko, S Trujillo, B Heyneman, and V Mattoli. Whole body adhesion: hierarchical, directional and distributed control of adhesive forces for a climbing robot. In *2007 IEEE International Conference on Robotics and Automation*, pages 1268–1273, January 2007.

[79] W Kim and J W M Bush. Natural drinking strategies. *Journal of Fluid Mechanics*, 705:7–25, 2012.

[80] Askin Kocabas, Ching-Han Shen, Zengcai V Guo, and Sharad Ramanathan. Controlling interneuron activity in Caenorhabditis elegans to evoke chemotactic behaviour. *Nature*, 490(7419):273–277, September 2012.

[81] J Koiller, K Ehlers, and R Montgomery. Problems and progress in microswimming. *Journal of Nonlinear Science*, 6:507–541, 1996.

[82] J Korta, D A Clark, C V Gabel, L Mahadevan, and A D T Samuel. Mechanosensation and mechanical load modulate the locomotory gait of swimming C. elegans. *Journal of Experimental Biology*, 210:2383–2389, 2007.

[83] P Krajacic, X Shen, P K Purohit, P Arratia, and T Lamitina. Biomechanical Profiling of Caenorhabditis elegans motility. *Genetics*, 191(3):1015–1021, July 2012.

[84] J N Kutz. *Data-Driven Modeling and Scientific Computing.* Oxford University Press, April 2013.

[85] E Lauga and T Powers. The hydrodynamics of swimming microorganisms. *Reports on Progress in Physics*, 72:096601, 2009.

[86] A M Leifer, C Fang-Yen, M Gershow, M J Alkema, and A D T Samuel. Optogenetic manipulation of neural activity in freely moving Caenorhabditis elegans. *Nature Methods*, 8(2):147–152, January 2011.

[87] J C Liao. Neuromuscular control of trout swimming in a vortex street: implications for energy economy during the Kármán gait. *Journal of Experimental Biology*, 207:3495–3506, 2004.

[88] J C Liao. The role of the lateral line and vision on body kinematics and hydrodynamic preference of rainbow trout in turbulent flow. *Journal of Experimental Biology*, 209:4077–4090, 2006.

[89] J C Liao. A review of fish swimming mechanics and behaviour in altered flows. *Philosophical Transactions of the Royal Society B: Biological Sciences*, 362(1487):1973–1993, November 2007.

[90] J C Liao, D N Beal, G V Lauder, and M S Triantafyllou. The Kármán gait: novel body kinematics of rainbow trout swimming in a vortex street. *Journal of Experimental Biology*, 206:1059–1073, 2003.

[91] M J Lighthill. On the squirming motion of nearly spherical deformable bodies through liquids at very small Reynolds numbers. *Communications on Pure and Applied Mathematics*, 5:109–118, 1952.

[92] K Linsenmair and R Jander. Das 'entspannungsschwimmen' von Velia and Stenus. *Naturwissenschaften*, 50:231, December 1976.

[93] J Liu, X Feng, and G Wang. Buoyant force and sinking conditions of a hydrophobic thin rod floating on water. *Physical Review E*, 76, 2007.

[94] J Liu and H Hu. Mimicry of Sharp Turning Behaviours in a Robotic Fish. *Proceedings of the 2005 IEEE International Conference on Robotics and Automation*, pages 3318–3323, 2005.

[95] J Liu and H Hu. Biological Inspiration: From Carangiform Fish to Multi-Joint Robotic Fish. *Journal of Bionic Engineering*, 7(1):35–48, March 2010.

[96] T Majmudar, E E Keaveny, J Zhang, and M J Shelley. Experiments and theory of undulatory locomotion in a simple structured medium. *Journal of The Royal Society Interface*, 9(73):1809–1823, 2012.

[97] R D Maladen, Y Ding, P B Umbanhowar, and D I Goldman. Undulatory swimming in sand: experimental and simulation studies of a robotic sandfish. *The International Journal of Robotics Research*, 30(7):793–805, 2011.

[98] K McIsaac and J P Ostrowski. Motion planning for anguilliform locomotion. *IEEE Transactions on Robotics*, 19:637, 2003.

[99] T A McMahon and J T Bonner. *On size and life.* Scientific American Library, New York, 1983.

[100] J Melli and C Rowley. Models and Control of Fish-Like Locomotion. *Experimental Mechanics*, 50, 2010.

[101] J Melli, C Rowley, and D Rufat. Motion planning for an articulated body in a perfect planar fluid. *SIAM Journal on Applied Dynamical Systems*, 5:650–669, 2006.

[102] R L Miller and C J Brokaw. Chemotactic turning behaviour of Tubularia spermatozoa. *Journal of Experimental Biology*, 52(3):699, 1970.

[103] NJ Mlot, CA Tovey, and David Hu. Fire ants self-assemble into waterproof rafts to survive floods. *PNAS*, 2011.

[104] K A Morgansen, B I Triplett, and D Klein. Geometric methods for modeling and control of free-swimming fin-actuated underwater vehicles. *IEEE Transactions on Robotics*, 23, 2007.

[105] R Mukherjee and D P Anderson. Nonholonomic motion planning using Stokes's theorem. In *1993 IEEE International Conference on Robotics and Automation Proceedings*, pages 802–809, 1993.

[106] R Murray, Z Li, and S Sastry. *A mathematical introduction to robotic manipulation.* CRC, Boca Raton, FL, 1994.

[107] R Murray and S Sastry. Nonholonomic motion planning: Steering using sinusoids. *IEEE Transactions on Automatic Control*, 38(5):700–716, May 1993.

[108] A Najafi and R Golestanian. Propulsion at low Reynolds number. *Journal of Physics: Condensed Matter*, 17:S1203, 2005.

[109] S Nakata, Y Doi, and H Kitahata. Synchronized Sailing of Two Camphor Boats in Polygonal Chambers. *J. Phys. Chem. B*, 109(5):1798–1802, February 2005.

[110] J C Nawroth, H Lee, A W Feinberg, C M Ripplinger, M L McCain, A Grosberg, J O Dabiri, and K K Parker. A tissue-engineered jellyfish with biomimetic propulsion. *Nature Biotechnology*, 30(8):792–797, July 2012.

[111] E Niebur and P Erdös. Theory of the locomotion of nematodes: Dynamics of undulatory progression on a surface. *Biophysical Journal*, 60(5):1132–1146, November 1991.

[112] E Niebur and P Erdös. Theory of the locomotion of nematodes: Control of the somatic motor neurons by interneurons. *Mathematical Biosciences*, 118:51–82, 1993.

[113] J P Ostrowski and J W Burdick. The geometric mechanics of undulatory robotic locomotion. *The International Journal of Robotics Research*, 17(7):683–701, 1998.

[114] J P Ostrowski, J W Burdick, A Lewis, and R Murray. The mechanics of undulatory locomotion: the mixed kinematic and dynamic case. In *Proceedings of the 1995 IEEE International Conference on Robotics and Automation*, 1995.

[115] J P Ostrowski, JP Desai, and V Kumar. Optimal Gait Selection for Nonholonomic Locomotion Systems. *The International Journal of Robotics Research*, 19(3):225–237, March 2000.

[116] V Padmanabhan, Z S Khan, D E Solomon, A Armstrong, K P Rumbaugh, S A Vanapalli, and J Blawzdziewicz. Locomotion of C. elegans: A Piecewise-Harmonic Curvature Representation of Nematode Behavior. *PLoS ONE*, 7(7):e40121, July 2012.

[117] D S Pavlov and M A Skorobogatov. Effect of the flow turbulence on the movement pattern of the caudal fin in fish. *Doklady Biological Sciences*, 428(1):464–466, October 2009.

[118] T Pedley and J Kessler. Hydrodynamic phenomena in suspensions of swimming microorganisms. *Annual Review of Fluid Mechanics*, 24:313, 1992.

[119] J T Pierce-Shimomura, B L Chen, J J Mun, R Ho, R Sarkis, and S L McIntire. Genetic analysis of crawling and swimming locomotory patterns in C. elegans. *Proceedings of the National Academy of Sciences*, 105(52):20982–20987, December 2008.

[120] E M Purcell. Life at low Reynolds number. *American Journal of Physics*, 45:3, 1977.

[121] C Py, P Reverdy, L Doppler, J Bico, B Roman, and C N Baroud. Capillary Origami: Spontaneous Wrapping of a Droplet with an Elastic Sheet. *Physicl Review Letters*, 98:156103, April 2007.

[122] J E Radford and J W Burdick. Local Motion Planning for Nonholonomic Control Systems Evolving on Principal Bundles. In *Proceedings of Mathematical Theory of Networks and Systems*, 1998.

[123] J N Reddy. *Energy Principles and Variational Methods in Applied Mechanics.* Wiley-Interscience, Hoboken, October 2002.

[124] P Reis, J Hure, S Jung, J W M Bush, and C Clanet. Grabbing water. *Soft Matter*, 6:5705–5708, 2010.

[125] I H Riedel Kruse, A Hilfinger, J Howard, and F Jülicher. How molecular motors shape the flagellar beat. *HFSP Journal*, 1(3):192–208, 2007.

[126] C W Rowley, I Mezic, S Bagheri, P Schlatter, and D S Henningson. Spectral analysis of nonlinear flows. *Journal of Fluid Mechanics*, 641:115–127, 2009.

[127] M S Sakar, D Neal, T Boudou, M A Borochin, Y Li, R Weiss, R D Kamm, C S Chen, and H H Asada. Formation and optogenetic control of engineered 3D skeletal muscle bioactuators. *Lab on a Chip*, 12(23):4976, 2012.

[128] D Santos, B Heyneman, S Kim, N Esparza, and M R Cutkosky. Gecko-inspired climbing behaviors on vertical and overhanging surfaces. In *2008 IEEE International Conference on Robotics and Automation*, pages 1125–1131, Pasadena, CA, April 2008.

[129] H Schildknecht. Chemical Ecology-A Chapter of Modern Natural Products Chemistry. *Angewandte Chemie International Edition in English*, 15(4):214–222, April 1976.

[130] P J Schmid. Dynamic mode decomposition of experimental data. *8th International Symposium on Particle Image Velocimetry*, 2009.

[131] L E Scriven and C V Sternling. The Marangoni Effects. *Nature*, 187:186–188, 1960.

[132] E Shammas. *Generalized motion planning for underactuated mechanical systems.* PhD thesis, Carnegie Mellon University, 2006.

[133] E Shammas, H Choset, and A Rizzi. Geometric motion planning analysis for two classes of underactuated mechanical systems. *The International Journal of Robotics Research*, 26:1043–1073, 2007.

[134] E Shammas, H Choset, and A Rizzi. Towards a unified approach to motion planning for dynamic underactuated mechanical systems with non-holonomic constraints. *The International Journal of Robotics Research*, 26:1075, 2007.

[135] A Shapere and F Wilczek. Geometry of Self-propulsion at Low Reynolds Number. *Journal of Fluid Mechanics*, 198:557–585, 1989.

[136] X Shen and P Arratia. Undulatory swimming in viscoelastic fluids. *Physical Review Letters*, 106(20):208101, May 2011.

[137] X Shen and P Arratia. C. elegans curvature data, April 2013.

[138] X N Shen, J Sznitman, P Krajacic, T Lamitina, and P E Arratia. Undulatory Locomotion of Caenorhabditis elegans on Wet Surfaces. *Biophysical Journal*, 102(12):2772–2781, June 2012.

[139] G J Stephens, B Johnson-Kerner, W Bialek, and W S Ryu. Dimensionality and Dynamics in the Behavior of C. elegans. *PLOS Computational Biology*, 4(4):e1000028, April 2008.

[140] J Sznitman, P K Purohit, P Krajacic, T Lamitina, and P E Arratia. Material properties of Caenorhabditis elegans swimming at low Reynolds number. *Biophysical Journal*, 98(4):617–626, February 2010.

[141] J Sznitman, X Shen, P K Purohit, and P E Arratia. The Effects of Fluid Viscosity on the Kinematics and Material Properties of C. elegans Swimming at Low Reynolds Number. *Experimental Mechanics*, 50(9):1303–1311, March 2010.

[142] J Sznitman, X Shen, P K Purohit, R Snitzman, and P E Arratia. Swimming behavior of the nematode caenorhabditis elegans bridging small scale locomotion with biomechanics. In C T Lim and J C H Goh, editors, *IFMBE Proceedings*, pages 29–32, 2010.

[143] D Tam. *Motion at low Reynolds number.* PhD thesis, Massachusetts Institute of Technology, 2008.

[144] D Tam and A E Hosoi. Optimal stroke patterns for Purcell's three-link swimmer. *Physics Review Letters*, 98:068105, 2007.

[145] D Tam and A E Hosoi. Optimal kinematics and morphologies for spermatozoa. *Physical Review E*, 83(4):045303, April 2011.

[146] X Tan, D Kim, N Usher, D Laboy, and J Jackson. An Autonomous Robotic Fish for Mobile Sensing. In *Procedings of the 2006 IEEE/RSJ International Conference on Intelligent Robots and Systems*, pages 5424–5429, Beijing, China, April 2006.

[147] J Thomson. On certain curious motions observable at the surfaces of wine and other alcoholic liquors . *Phil. Mag.*, 10:330–333, 1855.

[148] M S Triantafyllou and G S Triantafyllou. An Efficient Swimming Machine. *Scientific American*, 272(3):64–70, March 1995.

[149] E D Tytell. Kinematics and hydrodynamics of linear acceleration in eels, Anguilla rostrata. *Proceedings of the Royal Society Biological Sciences*, 271:2535–2540, 2004.

[150] E D Tytell. The hydrodynamics of eel swimming. II. Effect of swimming speed. *Journal of Experimental Biology*, 207:3265–3279, 2004.

[151] E D Tytell and G V Lauder. The hydrodynamics of eel swimming: I. Wake structure. *Journal of Experimental Biology*, 207:1825–1841, 2004.

[152] Y Umentani and S Hirose. Biomechanical study of serpentine locomotion. In *Proceedings of the 1st RoManSy Symposium*, Udine, Italy, 1974. Proc. 1st RoManSy Symp.

[153] P Valdivia y Alvarado and K Youcef-Toumi. Performance of Machines with Flexible Bodies Designed for Biomimetic Locomotion in Liquid Environments. In *Proceedings of the 2005 IEEE International Conference on Robotics and Automation*, pages 3324–3329, Barcelona, Spain, 2005.

[154] C Vega, J Ubbink, and E van der Linden, editors. *The Kitchen as Laboratory: Reflections on the Science of Food and Cooking.* Columbia University Press, 2012.

[155] D Vella. *The Fluid Mechanics of Floating and Sinking.* PhD thesis, PhD Thesis, Trinity College, University of Cambridge, August 2007.

[156] D Vella. Floating Objects with Finite Resistance to Bending. *Langmuir*, 24(16):8701–8706, 2008.

[157] D Vella, P Aussillous, and L Mahadevan. Elasticity of an interfacial particle raft. *EPL (Europhysics Letters)*, 68(2):212–218, 2004.

[158] D Vella, P Metcalfe, and R Whittaker. Equilibrium conditions for the floating of multiple interfacial objects. *Journal of Fluid Mechanics*, 549:215–224, 2006.

[159] S Vogel. *Life in Moving Fluids.* The Physical Biology of Flow. Princeton University Press, 1994.

[160] J Voise, M Schindler, J Casas, and E Raphael. Capillary-based static self-assembly in higher organisms. *Journal of The Royal Society Interface*, 8:1357–1366, 2011.

[161] G C Walsh and S Sastry. On reorienting linked rigid bodies using internal motions. *IEEE Transactions on Robotics and Automation*, 11(1):139–146, 1995.

[162] G Ward, C J Brokaw, D L Garbers, and V D Vacquier. Chemotaxis of Arbacia punctulata spermatozoa to resact, a peptide from the egg jelly layer. *The Journal of Cell Biology*, 101(6):2324, December 1985.

[163] P Webb. Entrainment by river chub Nocomis micropogon and smallmouth bass Micropterus dolomieu on cylinders. *Journal of Experimental Biology*, 201(16):2403–2412, 1998.

[164] D Weihs. Hydromechanics of Fish Schooling. *Nature*, 241(5387):290–291, January 1973.

[165] J G White, E Southgate, J N Thomson, and S Brenner. The Structure of the Nervous System of the Nematode Caenorhabditis elegans. *Philosophical Transactions of the Royal Society B: Biological Sciences*, 314(1165):1–340, November 1986.

[166] C Wiggins and R Goldstein. Flexive and propulsive dynamics of elastica at low Reynolds number. *Physics Review Letters*, 80:3879, 1998.

[167] A G Winter V, R L H Deits, D S Dorsch, A E Hosoi, and A H Slocum. Teaching RoboClam to Dig: The design, testing, and genetic algorithm optimization of a biomimetic robot. In *2010 IEEE/RSJ International Conference on Intelligent Robots and Systems (IROS)*, pages 4231–4235, 2010.

[168] A G Winter V and A E Hosoi. The design and testing of roboclam: a machine used to investigate and optimize razor clam inspired burrowing mechanisms for engineering applications. In *Proceedings of the ASME 2009 International Design Engineering Technical Conference & Computers and Information in Engineering Conference*, pages 1–6, June 2009.

[169] M Yoshida, K Inaba, K Ishida, and M Morisawa. Calcium and cyclic AMP mediate sperm activation, but Ca2+ alone contributes sperm chemotaxis in the ascidian, Ciona savignyi. *Development, Growth & Differentiation*, 36(6):589–595, 2008.

[170] T Yu, E Lauga, and A E Hosoi. Experimental investigations of elastic tail propulsion at low Reynolds number. *Physics of Fluids*, 18:091701, 2006.

[171] R K Zimmer and J A Riffell. Sperm chemotaxis, fluid shear, and the evolution of sexual reproduction. *Proceedings of the National Academy of Sciences*, 108(32):13200–13205, 2011.